Title
Binary Dynamics in Galactic Nuclei: Gravitational Waves and Electromagnetic Signatures

Author
Hoang, Bao Minh

Publication Date
2022

Peer reviewed|Thesis/dissertation

UNIVERSITY OF CALIFORNIA

Los Angeles

Binary Dynamics in Galactic Nuclei: Gravitational Waves and Electromagnetic Signatures

A dissertation submitted in partial satisfaction

of the requirements for the degree

Doctor of Philosophy in Astronomy and Astrophysics

by

Bao Minh Thi Hoang

2022

ABSTRACT OF THE DISSERTATION

Binary Dynamics in Galactic Nuclei:
Gravitational Waves and Electromagnetic Signatures

by

Bao Minh Thi Hoang
Doctor of Philosophy in Astronomy and Astrophysics
University of California, Los Angeles, 2022
Professor Smadar Naoz, Chair

Binaries play an important role in the overall dynamic and evolution of nuclear star clusters. In this dissertation, I explore, using semi-analytic methods, the dynamical evolution of binaries in galactic nuclei after the end of their luminous lives — starting from supernovae and continuing to the compact object phase — and their interactions with other cluster objects, in particular the supermassive black hole (SMBH). This stage of evolution can result in many observable phenomena, the abundance and properties of which are highly dependent on the properties of the underlying stellar binary population. Thus, an understanding of the dynamics of stellar remnants is crucial to understanding of the underlying stellar population.

I have shown that natal kicks in stellar binaries during supernovae can trigger a very wide variety of observable phenomena. These include but are not limited to: X-ray binaries, extreme mass ratio inspirals (EMRIs), and hypervelocity objects (including hypervelocity X-ray binaries). The population of X-ray binaries created by supernova kicks is a diagnostic for the black hole (BH) natal kick distribution, which remains highly debated. In particular, we found that no X-ray binaries with a BH primary is created if we assume no BH natal kicks. Subsequent to the natal kicks, most single and binary compact objects (COs) created remain bound to the SMBH. These COs can form gravitational wave (GW) mergers

detectable the by Laser Interferometer Gravitational-Wave Observatory (LIGO)/Virgo, the Laser Interferometer Space Antenna (LISA), and other future GW observatories.

In galactic nuclei, gravitational perturbations by the SMBH can induce eccentricity oscillations in binary COs, resulting in an elevated GW merger rate. I have shown that these eccentricity oscillations can be detected with LISA, out to a few Mpcs. This will allow us distinguish a variety of binary GW sources in galactic nuclei, from sources in other astrophysical environments. As for the single COs, although by themselves they do not emit GWs, in a dense stellar environment like nuclear clusters, they undergo frequent close encounters and emit energy in the form of GWs. If enough energy is emitted, they will form very close very eccentric binaries and merge. I have studied this mechanism as a formation channel for NSBH mergers and found that it is not likely to a major contributor to the overall NSBH rate detectable by LIGO. However, since the rate of merger from this mechanism is highly contingent on the characteristics of the single CO population, especially the density profile, we can use the future observations of NSBH mergers to confirm or revise our current understanding of the nuclear cluster environment.

The dissertation of Bao Minh Thi Hoang is approved.

Andrea M. Ghez

Bradley M. Hansen

Tommaso L. Treu

Smadar Naoz, Committee Chair

University of California, Los Angeles

2022

TABLE OF CONTENTS

ACKNOWLEDGMENTS

This dissertation has been supported by NASA LISA Preparatory Science grant No. 80NSSC19K0321, NASA ATP grant No. 80NSSC20K0505, the UCLA Graduate Dean's Scholarship, the Eugene V. Cota-Robles Fellowship, and the University of California Office of the President Dissertation Year Fellowship. Many thanks to Howard and Astrid Preston for their generous support, and to the Mani L. Bhaumik Institute for Theoretical Physics.

Chapter 3.3 is a reprint of "Detecting Kozai-Lidov Imprints on the Gravitational Waves of Intermediate-mass Black Holes in Galactic Nuclei", by Barnabás Deme, Bao-Minh Hoang, Smadar Naoz, and Bence Kocsis, published in The Astrophysical Journal, Volume 901, Issue 2, id. 125 (2020). This work was led by Barnabás Deme.

To my advisor Smadar Naoz: thank you for your tireless support and mentorship, without which I could not have done this, and for all the chocolate.

To my thesis committee members, Andrea Ghez, Brad Hansen, and Tommaso Treu: thank you for your guidance, support, and encouragement.

To my past and present research group members, including but not limited to Shelley Cheng, Yeou Chiou, Paul Denham, Isabella Goetting, Igor Marques Van Der Put, Cicero Lu, Chris O'Connor, Sanaea Rose, Jesus Salas, and Alexander Stephan, and Cheryl Wang: thank you for your fellowship and friendship.

To all my collaborators, including but not limited to Barnabás Deme, Will Farr, Kyle Kremer, Jess McIver, Fred Rasio, and especially Bence Kocsis: thank you for your advice, collaboration, and all that I have learnt from you.

To my parents and brother: thank you for your unending love and support.

To all my friends at UCLA, especially Zhuo Chen, Yeou Chiou, Veronica Dike, Helen Kim, Ronald Lopez, Kelly Kosmo O'Neill, and Sanaea Rose: thank you for your unflagging friendship, support, and all the laughs.

To Jack Stropko and Ethan Rosenberg: thank you for being my partners in adventure.

To Billy, my hummingbird friend: thank you for endless hours of joy.

Last but not least, to Jack: thank you for putting up with me.

VITA

2012–2016	B.S. in Astrophysics, University of California, Los Angeles
2016–2018	M.S. in Astronomy & Astrophysics, University of California, Los Angeles
2016–present	Ph.D. student in Astronomy & Astrophysics, University of California, Los Angeles

PUBLICATIONS

[1] **Bao-Minh Hoang**, Smadar Naoz, and Melodie Sloneker, "Binary Natal Kicks in the Galactic Center: X-ray Binaries, Hypervelocity Stars, and Gravitational Waves", ApJ, **934**, 54 (2022).

[2] **Bao-Minh Hoang**, Smadar Naoz, and Kyle Kremer, "Neutron Star-Black Hole Mergers from Gravitational-wave Captures", ApJ, **903**, 8 (2020).

[3] Barnabás Deme, **Bao-Minh Hoang**, Smadar Naoz, and Bence Kocsis, "Detecting Kozai-Lidov Imprints on the Gravitational Waves of Intermediate-mass Black Holes in Galactic Nuclei", ApJ, **901**, 125 (2020).

[4] **Bao-Minh Hoang**, Smadar Naoz, Bence Kocsis, Will Farr, and Jess McIver,"Detecting Supermassive Black Hole-Induced Binary Eccentricity Oscillations with LISA", ApJL, **875**, L31 (2019)

[5] **Bao-Minh Hoang**, Smadar Naoz, Bence Kocsis, Fred Rasio, and Fani Dosopoulou,"Black

Hole Mergers in Galactic Nuclei Induced by the Eccentric Kozai-Lidov Effect", ApJ, **856**, 140 (2018)

CHAPTER 1

Introduction

1.1 Why Study Binary Dynamics in Galactic Nuclei?

The past few decades have seen accelerating interest, progress, and many triumphs for the study of SMBHs and the nuclear star clusters that surround them; notably the observational confirmation of our galaxy's own Sagitarius A*, the 2020 Nobel Prize in Physics, the first image of an SMBH by the Event Horizon Telescope. The next few decades promise revolutionary new instruments to observe and study phenomena involving SMBHs, such as the Laser Interferometer Space Antenna (LISA), which is expected to observe gravitational wave (GW) mergers involving massive black holes, and the Thirty Meter Telescope (TMT), which is expected to drastically improve our ability to detect and map stars in our own Galactic Center.

The inescapable gravitational influence of the SMBH is responsible for shaping the fantastically dense and complex environment of the nuclear star cluster. In our own Galactic Center, some $10^7 M_\odot$ in the form of stars and stellar remnants lie within the central parsec (Genzel et al., 2003; Schödel et al., 2003). These include a young stellar population from a star formation episode approximately 4-6 Myr ago (e.g. Lu et al., 2009; Do et al., 2013a,b). The existence of such a young stellar population in the GC suggests perhaps a rich star formation and dynamical history consisting of multiple star formation episodes.

Binaries are expect to be part of these star formation episodes, and understanding their part is crucial to fully understanding the history and the overall evolution of galactic nuclei (e.g. Chu et al., 2018; Gautam et al., 2019). We have some observational and numerous theoretical pieces of evidence for the existence and importance of binaries in nuclear clusters. On the observational side: a large population of X-ray binaries have been observed in the central 1 pc (Muno et al., 2005; Hailey et al., 2018), and three stellar binaries have been confirmed in the inner ~ 0.2 pc (e.g., Ott et al., 1999; Martins et al., 2006; Rafelski et al., 2007; Pfuhl et al., 2014). Furthermore, most massive stars in the galactic field are in binaries or higher multiples (Raghavan et al., 2010; Moe & Di Stefano, 2017). Thus we might reasonably expect galactic nuclei to contain a similar binary fraction to the field, if not even higher, since the initial mass function in our Galactic Center apppears to be top heavy (Bartko et al., 2009; Lu et al., 2013). On the theoretical side, binaries have been invoked to explain a wide range of observed phenomena. For example, hypervelocity stars (HVS) can be explained by the tidal break up of binaries by the SMBH via the hills process (e.g. Hills, 1988; Yu & Tremaine, 2003), G2-like objects have been posited to be the remnants of binary mergers driven by the SMBH (Phifer et al., 2013; Witzel et al., 2014, 2017; Prodan et al., 2015; Stephan et al., 2016), and a high binary fraction in the Galactic Center have been recently invoked to explain the apparent low disk membership of stars between 0.04 and 0.5 pc (Naoz et al., 2018).

My dissertation focuses on the dynamics of binaries in galactic nuclei starting at the end of their luminous lives, from supernovae explosions, to their life after death as compact object binaries. The death of stellar binaries can provide valuable insight into their life. Understanding the process and rate via which CO binaries in nuclear clusters become GW sources allow us to constrain the the population of COs in galactic nuclei. We can then use these constraints, along with an understanding of the process via which massive stellar binaries become CO binaries, to better understand stellar population, star formation, and the dynamical evolution of galactic nuclei.

1.2 Outline of the Dissertation

Chapter 2 discusses results from my study Hoang et al. (2022), which explores the effect two successive natal kicks have on a massive stellar binary orbiting the SMBH, and the observable astrophysical phenomena generated. These phenomena, such as X-ray binaries, EMRIs, and hypervelocity stars and binaries, can be valuable diagnostics for the characteristics of the nuclear cluster binary population, and the properties of natal kicks. A fraction of these massive binaries stay together through the two natal kicks and become stellar-mass compact object binaries, which are among the most abundant sources gravitational waves (GW) detectable by LIGO/Virgo, and future GW observatories.

Compact object binaries in galactic nuclei face many competing forces, but most important to this thesis: the gravitational tug of the SMBH. Chapter 3 presents my findings on this topic in three publications. The first is Hoang et al. (2018), which studies the merger of black hole binaries induced by the gravitational influence of the SMBH, resulting in GWs detectable by LIGO/Virgo. The second publication, Hoang et al. (2019), presents a new method to detect the imprints the SMBH leaves on the GW signals of black hole binaries, using the Laser Interferometer Space Antenna (LISA). This method can be applied to signals from a wide variety of CO binaries. The final paper in this Chapter, Deme et al. (2020), applies this method to the GW signals of binaries in galactic nuclei consisting of an intermediate mass black hole and a stellar-mass object. This method is a unique way to distinguish GW signals of binaries in galactic nuclei from that of binaries in other astrophysical environments.

In Chapter 4 I discuss my publication Hoang et al. (2020), which explores whether the GW captures of single compact objects in dense clusters is a viable method to create NS-BH mergers. This study found that GW captures is unlikely to be the most dominant channel in creating NS-BH mergers. However, this result is based on several assumptions about the cusp densities of NSs and BHs in galactic nuclei, which are not definitively known. Moreover, most mergers from this channel have high eccentricities in the LIGO band. Thus, once LIGO has detected a statistical population of NS-BH mergers, we can use the observed rate of GW capture mergers to make inferences about the cusp densities of compact objects in galactic nuclei.

Finally, in Chapter 5 I summarize the dissertation's findings, and discuss its relevance and implications for future research.

CHAPTER 2

The Effect of Natal Kicks on Stellar Binaries in the Galactic Center

In this Chapter, I present my publication, Hoang et al. (2022), which investigates the fate of massive stellar binaries in the Galactic Center following two successive natal kicks. Observations have shown that NSs experience high natal kicks of several hundreds of km/s (e.g. Hansen & Phinney, 1997; Lorimer et al., 1997; Cordes & Chernoff, 1998; Fryer et al., 1999; Hobbs et al., 2004), while it is still debated whether black holes receive natal kicks or not (e.g., Gualandris et al., 2005; Willems et al., 2005; Fragos et al., 2009; Repetto et al., 2012). Some past studies have investigated the consequence of a single star orbiting a SMBH receiving a natal kick (Bortolas & Mapelli, 2019), and a binary receiving a single kick (Zubovas et al., 2013; Bortolas et al., 2017). Recently, Lu & Naoz (2019) explored the effect one to two natal kicks would have on various types of binaries orbiting an SMBH, with a proof-of-concept appproach.

In Hoang et al. (2022) we follow a population of massive stellar binaries in the Galactic Center from birth to the natal kick of the primary, and onto the natal kick of the secondary. Since the magnitude of natal kicks for BH progenitors is unknown, we explored different kick distributions for BHs, ranging from kicks with similar magnitudes to NS natal kicks, to no BH kicks at all. We found that two successive natal kicks in a stellar binary can lead to many different dynamical outcomes and observables, including but not limited to X-ray binaries, hypervelocity stars and binaries, and extreme mass ratio inspirals (EMRIs). Notably, we found that no X-ray binaries with a BH primary is created if we assume no BH natal kicks. Thus, the population of X-ray binaries in the Galactic Center may be a diagnostic for the BH natal kick distribution. We found that a majority of binaries are disrupted at the end of two natal kicks, but that a majority of the COs from these broken binaries are retained in the Galactic Center. Thus, successive star formation episodes should build up a dense cusp of COs. However, about 30% of the NSs in our simulations are ejected from the Galactic Center, which may be a contributor to the apparent "missing pular problem" (e.g. Pfahl & Loeb, 2004; Macquart et al., 2010; Dexter & O'Leary, 2014). A small fraction of the original binaries survive both natal kicks and become CO binaries, which are potential GW sources. We discuss this topic in the next Chapter.

The Astrophysical Journal, 934:54 (14pp), 2022 July 20 https://doi.org/10.3847/1538-4357/ac7787

Binary Natal Kicks in the Galactic Center: X-Ray Binaries, Hypervelocity Stars, and Gravitational Waves

Bao-Minh Hoang[1,2], Smadar Naoz[1,2], and Melodie Sloneker[1,2]
[1] Department of Physics and Astronomy, University of California, Los Angeles, CA 90095, USA; bmhoang@astro.ucla.edu
[2] Mani L. Bhaumik Institute for Theoretical Physics, Department of Physics and Astronomy, University of California, Los Angeles, CA 90095, USA
Received 2022 April 7; revised 2022 June 4; accepted 2022 June 9; published 2022 July 25

Abstract

Theoretical and observational studies suggest that stellar binaries exist in large numbers in galactic nuclei like our own Galactic Center. Neutron stars (NSs), and debatedly, black holes and white dwarfs, receive natal kicks at birth. In this work, we study the effect of two successive natal kicks on a population of stellar binaries orbiting the massive black hole (MBH) in our Galactic Center. These natal kicks can significantly alter the binary orbit in a variety of ways, and also the orbit of the binary around the MBH. We found a variety of dynamical outcomes resulting from these kicks, including a steeper cusp of single NSs relative to the initial binary distribution. Furthermore, hypervelocity star and binary candidates, including hypervelocity X-ray binaries, are a common outcome of natal kicks. In addition, we show that the population of X-ray binaries in the Galactic Center can be used as a diagnostic for the BH natal kick distribution. Finally, we estimate the rate of gravitational wave events triggered by natal kicks, including binary mergers and EMRIs.

Unified Astronomy Thesaurus concepts: Galactic center (565); Stellar dynamics (1596); Supernova dynamics (1664); X-ray binary stars (1811); Hypervelocity stars (776); Gravitational waves (678)

1. Introduction

Most galaxies, including our own, host a massive black hole (MBH) at their centers (e.g., Kormendy & Richstone 1995; Ghez et al. 2000, 2008; Kormendy & Ho 2013). Around these MBHs are the incredibly dense structures composed of stars and stellar remnants, called nuclear star clusters (NSCs).

Both theoretical and observational evidence suggests that binaries are common in NSCs. On the theoretical side, Stephan et al. (2016) showed that as many as 70% of the binaries formed in an initial star formation episode survive after a few megayears. Furthermore, Rose et al. (2020) showed that these surviving young (a few megayears) binaries can have a wide range of orbital configurations and separations. Naoz et al. (2018) showed that a high binary fraction can explain many puzzling aspects of the young stellar disk in our own Galactic Center (e.g., Yelda et al. 2014).

On the observational side, recent works have suggested that binaries are prevalent in our galaxy for massive stars (about 70% for ABO spectral type stars) (e.g., Raghavan et al. 2010; Moe & Di Stefano 2017). Thus, we can reasonably infer a comparably large binary fraction for massive stars in NSCs. Furthermore, the large number of observed X-ray sources in the central 1 pc suggests relatively large numbers of binaries containing BHs and NSs in the Galactic Center (Muno et al. 2005; Hailey et al. 2018). Moreover, there are three confirmed binaries in the inner ∼0.2 pc (e.g., Ott et al. 1999; Martins et al. 2006; Rafelski et al. 2007; Pfuhl et al. 2014), with possibly more candidates (e.g., Gautam et al. 2019; Jia et al. 2019).

For massive binaries, a potentially important effect is the *natal* kick that neutron star (NS) progenitors (and debatedly, black hole (BH) progenitors), receive from supernova (SN) explosions. Observations of pulsar proper motions have shown that neutron stars (NSs) receive large kicks of hundreds of kilometers per second (e.g., Hansen & Phinney 1997; Lorimer et al. 1997; Cordes & Chernoff 1998; Fryer et al. 1999; Hobbs et al. 2004). Natal kicks have been shown to explain the spin–orbit misalignment of pulsar binaries (Lai et al. 1995; Kalogera 1996; Kaspi et al. 1996; Kalogera et al. 1998; Kalogera 2000). Furthermore, it has been suggested that hypervelocity stars (HVSs; Zubovas et al. 2013; Bortolas et al. 2017; Fragione et al. 2017; Lu & Naoz 2019), and extreme mass ratio inspirals (EMRIs; e.g., Bortolas & Mapelli 2019; Lu & Naoz 2019), can result from natal kicks.

Recently, Lu & Naoz (2019) explored natal kicks in hierarchical triple systems, including stellar-mass binaries near an MBH (see also Hamers et al. 2018). They found that the natal kicks in these systems can lead to the inner binary shrinking as well as expanding, leading to many possible observable phenomena. In this work, we explore the dynamical and observable consequences of two successive natal kicks on a population of stellar binaries in the Galactic Center. Below we give a brief summary of the steps we take in our study and the structure of this paper:

1. We generate a population of massive stellar binaries. This is described in Section 2.1.
2. We evolve the stellar binaries up to the m_1's natal kick and eliminate any binaries that undergo Roche lobe overflow before m_1's natal kick. This process is described in Section 2.2.
3. We apply the natal kick to m_1 and recalculate the orbits. We check the new orbits for any natal kick-induced observable phenomena (e.g., X-ray binary, HVSs). We then apply the natal kick to m_2 and repeat the process of checking for outcomes. We describe how we apply the natal kicks in more detail in Section 2.3. We describe the criteria we used to classify the outcomes and describe the

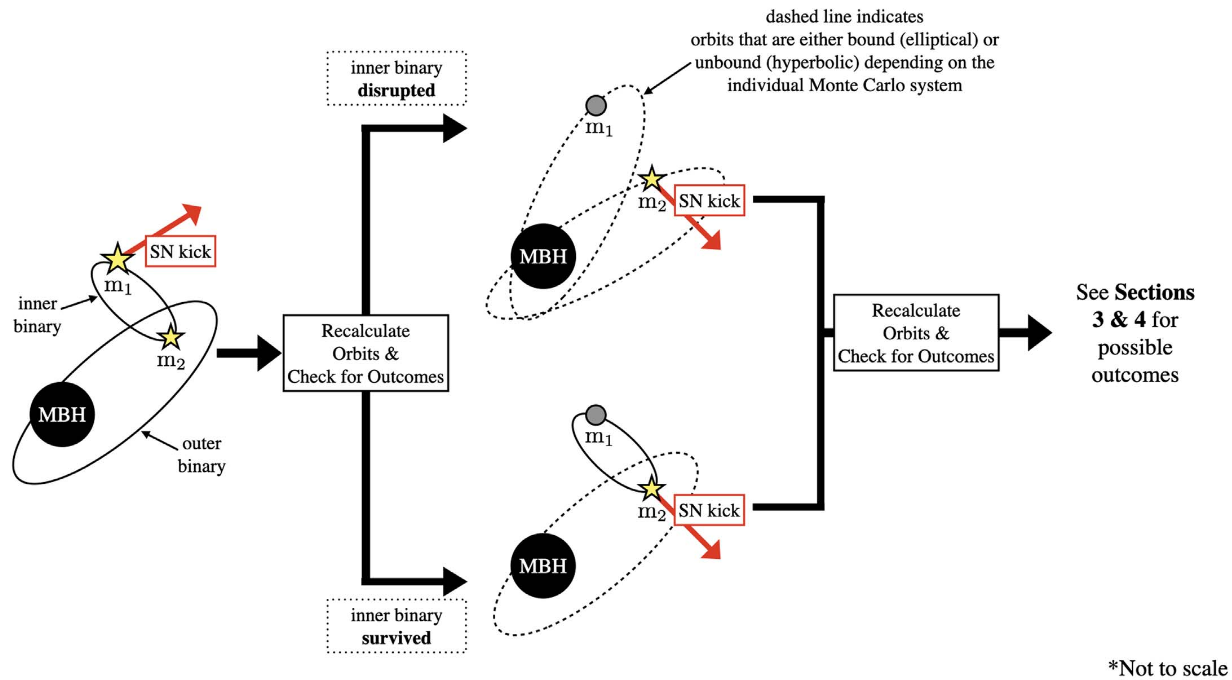

Figure 1. A simplified schematic of our analysis process. Note that this schematic does not illustrate every single possible outcome of natal kicks on a binary.

results of our Monte Carlo simulations in Sections 3 and 4.

A simplified schematic of our steps is given in Figure 1, and a summary of the outcomes of our simulations is given in bar chart form in Figure 4.

2. Methodology

We employ simple Monte Carlo simulations to explore the outcomes of two natal kicks on massive stellar binaries orbiting an MBH within 0.1 pc. Inward to this limit, $\sim 1.5 \times 10^5$ stars are expected to reside, estimated from the M-σ relation (e.g., Tremaine et al. 2002). Thus, this limit is used to estimate the effects of natal kicks on the system close to the MBH.

2.1. Monte Carlo Birth Distributions

We run a total of 300,000 Monte Carlo simulations of a binary star (the *inner binary*) orbiting an MBH (the *outer binary*) in a hierarchical triple configuration system. The inner binary comprises of main-sequence stars with birth masses m_1 and m_2, and the MBH has a mass of $m_{\rm MBH} = 4 \times 10^6\, M_\odot$. The inner (outer) orbit is characterized by the following orbital parameters: the semimajor axis $a_1(a_2)$, the eccentricity $e_1(e_2)$, the argument of periapsis ω_1 (ω_2), the longitude of the ascending node Ω_1 (Ω_2), and the true anomaly $f_1(f_2)$. The inner and outer orbits have a mutual inclination of $i_{\rm tot}$.

For our Monte Carlo simulations, we set m_1 as the more massive star and therefore is always the one that undergoes the first SN in the system. The birth value of m_1 is chosen from a Kroupa mass distribution ranging from 8–100 $M_\odot$ (Kroupa 2001), and $m_2/m_1 = q$, where the mass ratio q is chosen from a uniform distribution ranging from 0.1–1. Note that because of this mass distribution, some m_2's will be white dwarf (WD) progenitors, and a small percentage will not undergo SN at all. Among the systems that are not eliminated in the pre-SN evolution (see Section 2.2), 53.2% of stars become NSs, 19.5% become BHs, WD 26.2% become WDs, and 1.2% never become a compact object (CO).

The inner (outer) orbital eccentricities are chosen from a uniform (thermal) distribution ranging from 0–1. We distribute the mutual inclination $i_{\rm tot}$ isotropically. Further, the arguments of periapsis, true anomalies, and the inner binary longitude of the ascending node Ω_1 are chosen from a uniform distribution between 0 and 2π. Since we are working in the invariable plane reference plane, $\Omega_2 = \Omega_1 - \pi$.

The outer semimajor axis a_2 is chosen from a number density distribution that goes as $n \propto r^{-2}$ with a minimum value of 1000 au, which is roughly the semimajor axis of the well-studied star S0-2 in the S-cluster in the Galactic Center, and a maximum value of 0.1 pc (see above). Note that current observations of late-type giant stars in the Galactic Center show a shallow core-like profile, rather than a cusp (e.g., Do et al. 2013). It remains debated whether this flat density distribution is representative of the rest of the stellar population (e.g., Genzel et al. 2003; Do et al. 2009; Bartko et al. 2010; Schödel et al. 2020). Theoretical models have found steeper cusps ranging from 1.5–2.75, depending on the mass component (e.g., Bahcall & Wolf 1977; Alexander & Hopman 2009). We expect the density distribution of binaries around the MBH to have an effect on some parts of our results. For example, we expect more EMRIs for a steeper cusp since supernovae closer to the MBH are more likely to result in an EMRI (Bortolas & Mapelli 2019). On the other hand, we do not expect that our results for X-ray binaries will be greatly affected, since their formation depends more on the properties of the inner binary.

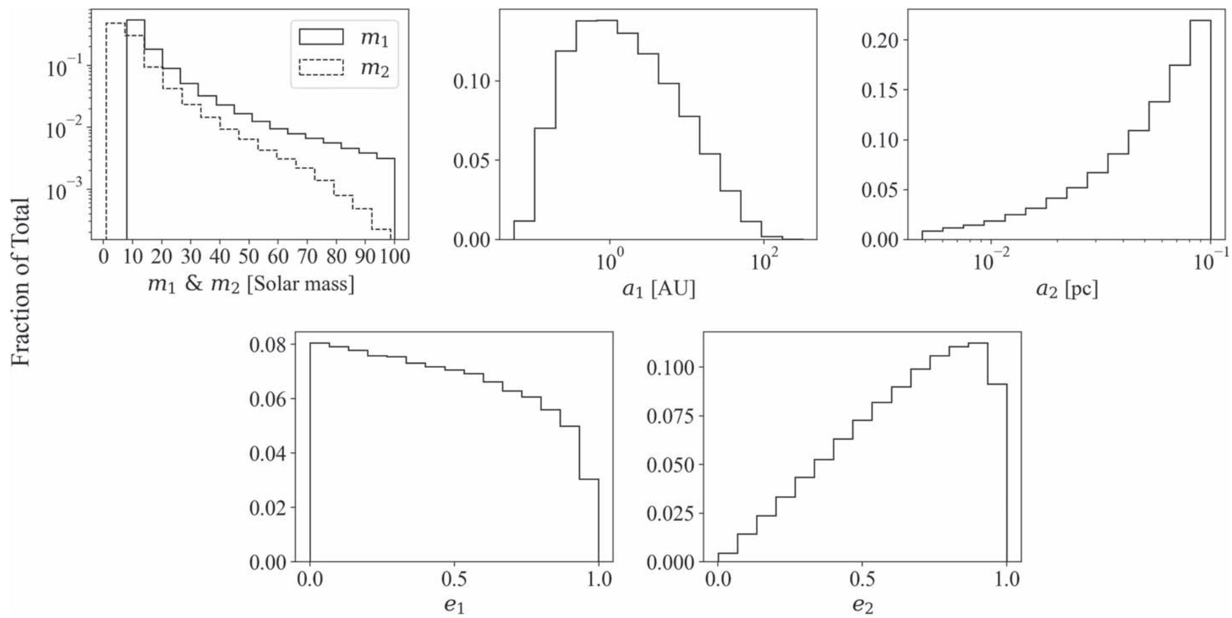

Figure 2. Distributions of the initial triple parameters.

We leave a comprehensive exploration of the effect of varying the density distribution to a future work.

We choose the inner binary semimajor axis a_1 from the period distribution $dn/dP \propto \log(P)^{-0.45}$ (Sana et al. 2013), with the minimum and maximum values of a_1 chosen for each system according to the following criteria. First, we require the inner orbit pericenter to be greater than 2 times the Roche limit of the system:

$$a_1(1 - e_1) > 2\, a_{\rm Roche}. \tag{1}$$

The Roche limit $a_{{\rm Roche},ij}$ for either star in the inner binary[3] is defined as

$$a_{{\rm Roche},ij} = \frac{R_j}{\mu_{{\rm Roche},ji}}, \tag{2}$$

where R_j is the radius of the star of mass m_j, found by the ZAMS mass–radius relation:

$$R(m) = 1.01\, m^{0.57}\, R_\odot \tag{3}$$

(Demircan & Kahraman 1991), and $\mu_{{\rm Roche},ji}$ is defined by

$$\mu_{{\rm Roche},ji} = \frac{0.49(m_j/m_i)^{2/3}}{0.6(m_j/m_i)^{2/3} + \ln(1 + (m_j/m_i)^{1/3})} \tag{4}$$

(Eggleton 1983). To find the upper limit of a_1, we require that each triple system is dynamically stable (Naoz 2016):

$$\frac{a_1}{a_2}\frac{e_2}{1 - e_2^2} < 0.1. \tag{5}$$

Finally, we require that the inner binary does not cross the Roche limit of the central MBH, and thus eliminate systems that do not fulfill the criterion below:

$$a_2(1 - e_2) > a_1(1 + e_1)\left(\frac{3\, m_{\rm MBH}}{m_1 + m_2}\right)^{1/3} \tag{6}$$

(e.g., Naoz & Silk 2014). We show the initial distributions of m_1, m_2, a_1, a_2, e_1, and e_2 in Figure 2.

2.2. Pre-SN Evolution

For each star in the inner binary, we find the time at which it becomes a CO and its mass before and after this transition with SSE (Hurley et al. 2000). The stars experience mass loss due to main-sequence evolution between birth and the first SN, and between the first SN and the second SN. Between birth and the first SN the inner binary will expand due to mass loss (the outer binary will also expand, but by a negligible amount due to the large mass of the MBH). We find the inner binary semimajor axis immediately before the first SN, $a_{1,{\rm pre-SN}}$ by adopting adiabatic expansion, which conserved specific angular momentum:

$$a_{1,{\rm pre-SN}} = \frac{m_1 + m_2}{m_{1,{\rm pre-SN}} + m_{2,{\rm pre-SN}}} a_1. \tag{7}$$

We note that we do not perform a numerical integration of the triple system either before the first kick or between the first and second kick. Eccentricity oscillations in the inner binary driven by the eccentric Kozai–Lidov effect (EKL; Naoz 2016), coupled with stellar evolution, can cause the inner stellar binary to become tidally locked, collide, or overflow its Roche lobe, long before either of the stars undergo an SN (e.g., Stephan et al. 2016, 2019). We cannot account for all of these systems without a numerical simulation. However, we use analytical criteria to identify systems where EKL causes the stellar binary to overflow its Roche lobe. The EKL timescale on which the inner binary experiences eccentricity oscillations is approximately

[3] For Equation (1), we take $a_{\rm Roche} = \max[a_{{\rm Roche},12}, a_{{\rm Roche},21}]$.

(e.g., Antognini 2015)

$$t_{\rm EKL} \sim \frac{16}{15}\frac{a_2^3(1-e_2^2)^{3/2}\sqrt{m_1+m_2}}{a_1^{3/2}m_{\rm MBH}k}. \tag{8}$$

This timescale needs to be shorter than the inner binary general relativity (GR) precession timescale $t_{\rm GR}$ in order for EKL to excite the inner binary eccentricity.[4] The GR precession timescale of the inner binary is defined as

$$t_{\rm GR,\ inner} \sim 2\pi\frac{a_1^{5/2}c^2(1-e_1^2)}{3G^{3/2}(m_1+m_2)^{3/2}}, \tag{9}$$

where c is the speed of light.

For systems with $t_{\rm ELK} < t_{\rm GR,\ inner}$ and mutual inclination between 40° and 140° the maximal eccentricity $e_{1,\max}$ achieved by the inner binary during one Kozai–Lidov cycle can be approximated analytically (e.g., Miller & Hamilton 2002; Wen 2003; Fabrycky & Tremaine 2007; Liu et al. 2015). We approximate $e_{1,\max}$ using the method outlined in Wen (2003).

If the minimum pericenter distance achieved during $t_{\rm EKL}$ (we also require that $t_{\rm EKL}$ is less than the timescale to the first SN) is less than the binary Roche limit $a_1(1-e_{1,\max}) < a_{\rm Roche}$, the stellar binary will undergo Roche lobe overflow and mass transfer. We found that roughly 10% of initial stellar binaries fit these criteria. The subsequent binary evolution is out of the scope of our methodology. Thus, we eliminate these systems from our simulations and do not evolve them to the SN stage. We note that the approach here uses the three-body Hamiltonian up to the quadrupole order, and cannot account for extreme eccentricities excited by the octupole term (e.g., Naoz 2016). Moreover, for inner and outer eccentric orbits, the EKL mechanism can excite high eccentricity for a wide range of inclinations (e.g., Lithwick & Naoz 2011; Naoz et al. 2013a; Li et al. 2014a, 2014b). Therefore, our approach here eliminates a conservative fraction of systems. However, we do expect that the binary orbital distribution from this approach will capture the distribution of the binaries post EKL, just before the first SN (as was highlighted in Rose et al. 2019).

We note that even though we eliminate these systems in the pre-SN stage, the statistics that we give later in the paper are with respect to the initial triple population we generated in Section 2.1. This is so that the event formation fractions we give later on in the paper can be simply multiplied by a star formation rate.

2.3. SN Kicks

We then apply the SN kick to m_1. We assume SN kicks are isotropically distributed in the inner binary orbital frame. We also assume instantaneous mass loss at the moment of the SN, using post-SN masses found with SSE (Hurley et al. 2000). For NS progenitors, we assume kicks drawn from a normal distribution with an average of 400 km s^{-1} and a standard deviation of 265 km s^{-1} (e.g., Hansen & Phinney 1997; Arzoumanian et al. 2002; Hobbs et al. 2004). For WDs, which are present in the second set of kicks, we assume a normal distribution with an average of 0.8 km s^{-1} and a standard deviation of 0.5 km s^{-1} (e.g., El-Badry & Rix 2018; Hamers & Thompson 2019). There is much uncertainty about whether BHs receive natal kicks, and if they do, what the distribution of kick velocities would be (e.g., Gualandris et al. 2005a; Willems et al. 2005; Fragos et al. 2009; Repetto et al. 2012). Thus, we adopt three different kick distributions for BH progenitors:

1. *Fast* BH kicks that are drawn from the same distribution as NS kicks.
2. Following Bortolas & Mapelli (2019), *slow* BH kicks that assume BHs receive the same linear momentum as NSs (i.e., we draw a kick velocity from the NS distribution, then multiply this by $(1.4\,M_\odot/m_{\rm BH})$, where $m_{\rm BH}$ is the mass of the BH progenitor, and 1.4 $M_\odot$ is the typical NS mass).
3. No BH kicks.

We run 100,000 simulations for each scenario, for a total of 300,000 simulations. We present statistics from all three scenarios in Sections 3 and 4, and in Figure 4.

To apply the natal kick, we simply add the Cartesian velocity kick vector to the velocity vector of m_1, and change m_1 to the post-SN mass found with SSE. We then use a new velocity vector and mass to recalculate new orbital parameters.

The two main scenarios resulting from this first kick are the *inner binary survived* and the *inner binary disrupted* cases (see Figure 1). In the case where the inner binary survives the first kick, we have two further branching scenarios. The inner binary can either stay bound to the MBH (elliptical orbit), or become unbound from the MBH (hyperbolic orbit). In the case where the inner binary is disrupted by the first kick, the component masses form separate binaries with the MBH (i.e., m_1-MBH and m_2-MBH). These binaries can either be bound or unbound. We then evolve m_2 up to its own natal kick, and recalculate the orbits after m_2's kick. Between m_1's and m_2's kicks we evolve the orbits as follows:

1. We adiabatically expand the orbits, due to m_2's mass loss, using Equation (7).
2. For hyperbolic orbits, we solve the hyperbolic Kepler Equation using the HKE-SDG package (Raposo-Pulido & Peláez 2018) to find the hyperbolic anomaly at the time of m_2's kick, from which we calculate the true anomaly. Using the newly calculated true anomaly with the Keplerian elements of the orbit, we calculate the Cartesian coordinates of the objects in the orbit.
3. For elliptical orbits, how we calculate the true anomaly at the time of m_2's kick depends on the timescales of the system. If the timescale between the first and second natal kick is longer than 10 times the orbital period, we simply choose the eccentric anomaly at the time of m_2's kick randomly from a uniform distribution between 0 and 2π. Otherwise, we solve the elliptical Kepler's equation iteratively using Newton's method to find the eccentric anomaly. From this, we calculate the true anomaly, and then the Cartesian coordinates of the orbit.

After each kick we check whether the natal kick had induced any observable phenomena (e.g., X-ray binary, gravitational wave (GW) merger, etc.). We describe our criteria in Section 3 for the cases where the inner binary is disrupted, and in Section 4 for the cases where the inner binary survived. We also present results and statistics from our simulations for each outcome in the following two sections. We include a simplified schematic of our process in Figure 1.

[4] However, in some cases, when the GR timescale is comparable or longer than the EKL timescale, the GR precession can trigger eccentricity excitation even in regimes that suppress the large eccentricity excitations (e.g., Naoz et al. 2013b; Hansen & Naoz 2020).

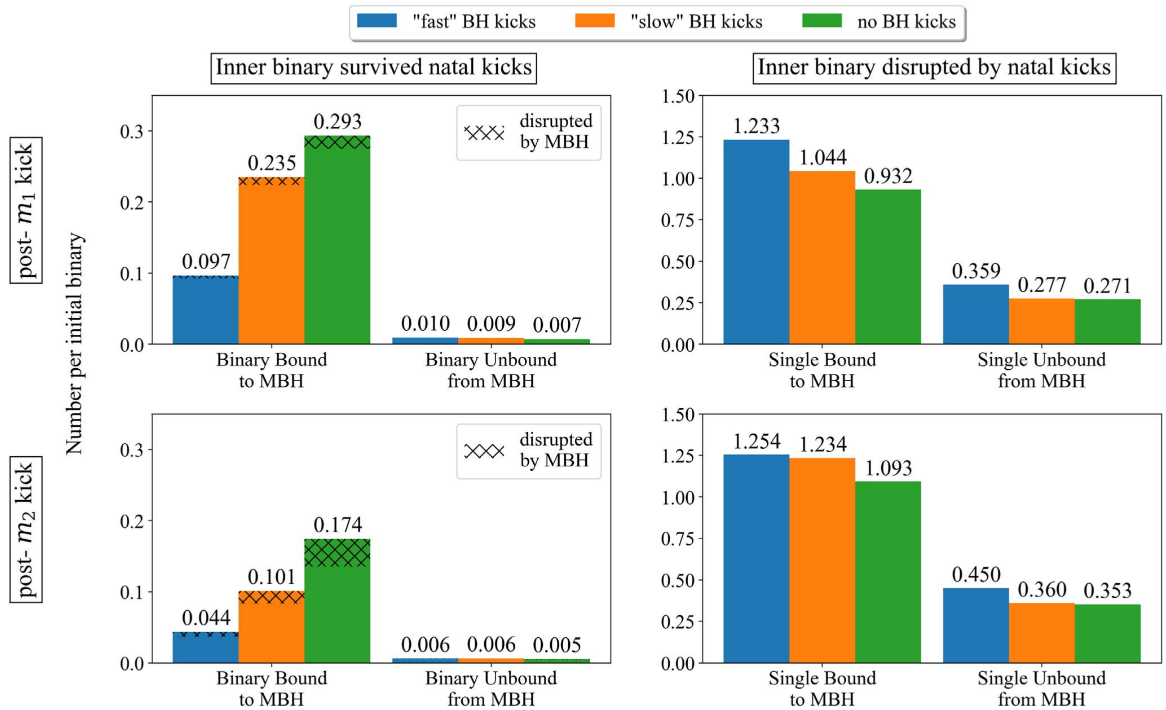

Figure 3. Summary of orbital configuration resulting from each natal kick. In the top (bottom) panels we show the results from after the first (second) natal kick. In the left (right) panels we show the orbital configurations where the inner binary survived (is disrupted by) the natal kicks. In the left panels, we use the crossed pattern to represent the binaries that survived the natal kick, but will be disrupted by crossing the MBH Roche limit upon pericenter passage (Section 4.3). We note that for the *single bound to MBH* cases, we have numbers greater than 1 because this number is taken relative to the number of initial binaries, and each binary contains two singles.

3. Inner Binary Disrupted by Natal Kicks

In the case that the inner binary is disrupted by either m_1's or m_2's natal kick, the result is two separate binaries with each composed of a stellar mass object orbiting the MBH (m_1-MBH and m_2-MBH). These orbits can either be bound (elliptical orbit), or unbound (hyperbolic orbit). However, natal kicks are less likely to result in unbound objects, as we find that the majority of objects remain bound to the MBH. See Table 2, for percentages of bound and unbound orbits as a function of stellar type.

The orbital configurations and observables resulting from these systems are described below. We also give rates of each orbital configuration and observables from our Monte Carlo simulations. These rates are summarized in bar chart form in Figures 3 and 4, which also break down the rates by BH kick distribution.

3.1. Single Objects Bound to MBH

Single objects bound to the MBH are the most common resulting orbital configuration in our simulations. We find 0.9–1.2 single objects per initial binary bound to the MBH after the first natal kick, and 1.1–1.3 after both natal kicks (see Figure 3). The vast majority of these orbits are long-term stable orbits, with a very small number becoming EMRIs (Section 3.1.1), direct plunges (Section 3.1.2), and TDEs (Section 3.1.3).

In Figure 5 we show the distribution of NSs, BHs, and WDs with respect to the MBH after two successive natal kicks. Note that each triple is evolved in its own simulation, and each system undergoes natal kicks at different times, thus Figure 5 does not accurately show the distribution of a contemporaneous population of COs. However, Figure 5 is a good approximation of NS and BH distributions between a few tens of megayears and ~ 1 Gyr after the star formation episode. This is because NS natal kicks occur between $\sim$10 and 45 Myr and BH natal kicks occur between ~ 4 and 10 Myr, and the two-body relaxation timescale in the Galactic Center is $\sim 0.1-1$ Gyr (Rose et al. 2020). WD natal kicks occur between 45 and 1.4×10^4 Myr, so Figure 5 cannot be taken as a representation of a contemporaneous population of WDs at any given time.

Figure 5 shows that after two successive natal kicks, the cusp of single NSs is steeper than the initial stellar binary cusp. This is also true for the BHs if we assume fast BH kicks. WDs and BHs with no kicks more or less follow the initial stellar binary distribution.

In fact, a steeper NS cusp is already present after just one natal kick. In Figure 6 we show the distribution of single NSs, BHs, stars, and binaries bound to the MBH after the first natal kick, for the slow BH kicks scenario. We see a steeper distribution of NSs than for BHs and stars, and a steeper distribution of binaries with an NS primary than for binaries with a BH primary. Thus, for a relatively young stellar population, before mass segregation has taken place, we expect a steeper cusp of NSs relative to the stellar and BH cusp. This is of course excepting the case in which BHs receive fast kicks similar to NSs, in which case the BH cusp

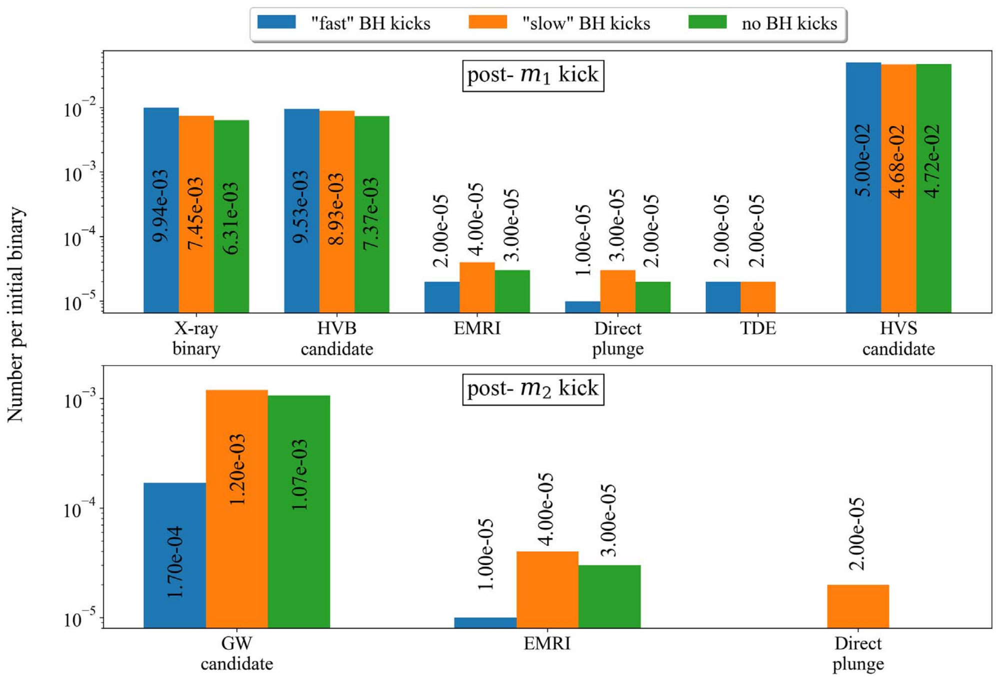

Figure 4. Number of observables per initial stellar binary (see footnote 5), triggered by the first natal kick (top panel), and by the second natal kick (bottom panel). For details about how we classify the different observables, see the following sections: X-ray binaries (Section 4.1.1); HVB candidates (hypervelocity binaries, Section (4.2); GW candidates (Section 4.1.2); HVS candidates (Section 3.2.1); EMRIs (Section 3.1.1); direct plunges (Section 3.1.2); and TDEs (tidal disruption events, Section 3.1.3).

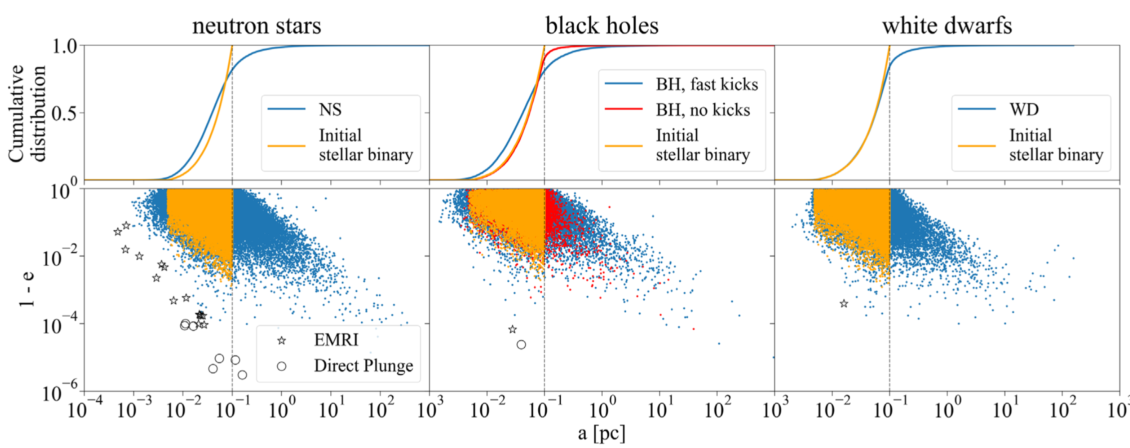

Figure 5. Distribution of bound single CO orbits after two successive natal kicks in the $(a, 1-e)$ plane (a and e are the semimajor axis and eccentricity with respect to the MBH). These objects were components of the stellar binaries that were disrupted by the natal kicks. For the NSs and WDs, we show data only from the *fast* BH kicks simulation set as the NS and WD kick distributions do not change between simulation sets and the results from any one set are fairly representative of the others. For the BHs, we show data from both the fast (in blue) and no BH kicks (in red) simulation sets to demonstrate two extremes. We plot the distribution (with respect to the MBH) of the initial stellar binaries that contained the compact object progenitors in yellow for comparison. In addition, we plot the distribution of EMRI progenitors (empty star symbol) and direct plunge progenitors (empty circles).

will be as steep as the NS cusp after the first natal kick (not shown in the figure).

3.1.1. EMRIs

EMRIs are gradual GW inspirals of stellar-mass COs onto MBHs, and are one of the main targets for the future Laser Interferometer Space Antenna (LISA; Danzmann et al. 2017). The timescale on which a CO inspirals onto an MBH is (Peters 1964)

$$t_{\rm GW,\,EMRI} \sim \frac{5}{64}\frac{c^5 a^4}{G^3 m_{\rm MBH}^2 m}(1-e^2)^{7/2}. \tag{10}$$

In a dense environment, such as the Galactic Center, we also have to take into account the effects of two-body relaxation on the

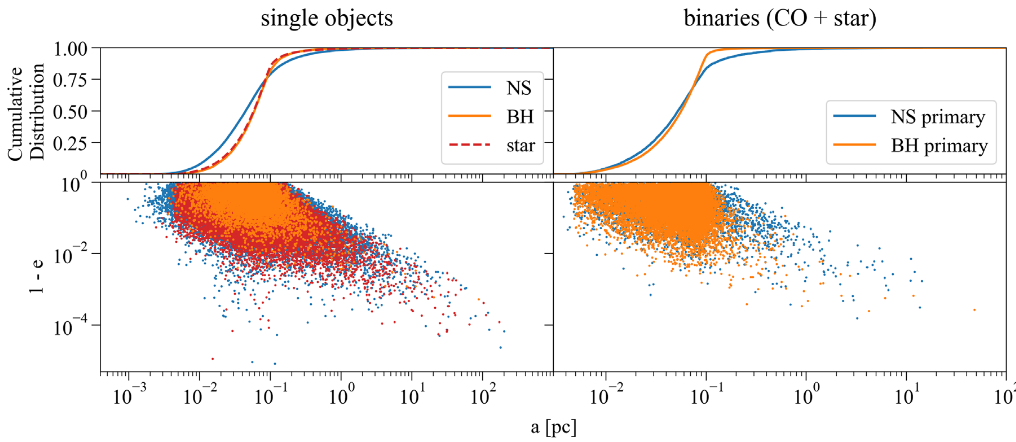

Figure 6. Distribution of single objects and binaries bound to the MBH after the first natal kick in the (a, $1-e$) plane (bottom panels), and the cumulative distribution of a (top panels), for the slow BH kicks scenario. The variables a and e are the semimajor axis and eccentricity with respect to the MBH.

potential EMRI. While two-body relaxation from other stars in the cluster can create EMRIs by pushing COs onto high eccentricity orbits, it can also push COs onto more circular orbits, such that $t_{\rm GW,EMRI}$ increases to longer than a Hubble time. Two-body relaxation changes an orbit's angular momentum by an order of itself on a timescale of $\sim(1-e)t_{\rm relax}$, where $t_{\rm relax}$ is

$$t_{\rm relax} = \frac{0.34}{\ln\Lambda}\frac{\sigma^3(r)}{G^2\rho(r)m}, \tag{11}$$

where $\ln\Lambda = 15$ is the Coulomb algorithm, and $\sigma(r)$ is the velocity dispersion, given by (Kocsis & Tremaine 2011),

$$\sigma(r) = 280\ {\rm km\ s^{-1}}\sqrt{\frac{0.1\ {\rm pc}}{r}}, \tag{12}$$

and $\rho(r)$ is the Galactic Center stellar density (Genzel et al. 2010)

$$\rho(r) = 1.35\times10^6\,M_\odot\ {\rm pc^{-3}}\left(\frac{r}{0.25\ {\rm pc}}\right)^{-1/3}. \tag{13}$$

Thus, we require that $t_{\rm GW,EMRI} < (1-e)t_{\rm relax}$ be classified as an EMRI (e.g., Amaro-Seoane et al. 2007).

EMRI formation is a rare event in our simulations. In particular, we find $(3-8)\times10^{-5}$ EMRIs per initial stellar binary.[5] This is roughly consistent with results from Bortolas & Mapelli (2019), which studied EMRIs triggered by natal kicks on single stars in the Galactic Center and found a rate of 10^{-7}–10^{-4} EMRIs per SN. Assuming a star formation rate of $10^3\,M_\odot\ {\rm Myr^{-1}}$ in the Galactic Center (e.g., Lu et al. 2009), and an average binary mass of $30M_\odot$ (from our Monte Carlo simulations), we obtain an EMRI rate of $(1-2.7)\times10^{-9}\ {\rm yr^{-1}}$. Assuming a galaxy density of $0.02\ {\rm Mpc^{-3}}$ (Conselice et al. 2005), and that half of galaxies contain an MBH at the center, we calculate an EMRI volume rate of $0.01-0.027\ {\rm Gpc^{-3}\ yr^{-1}}$ from our simulations.[6] However, we note that this rate is likely a conservative one because of the minimum value of 1000 au that we have chosen for the binary distribution around the MBH. As shown by Bortolas & Mapelli (2019), stars closer to the MBH are much more likely than stars further away to end up as an EMRI after undergoing an SN. Thus, EMRI rates are very sensitive to the inner edge of the initial binary distribution. Currently, there are several observed stars in the S-cluster with semimajor axes smaller than 1000 au: S0102/S55 with a semimajor axis of ∼900 au (Meyer et al. 2012), S62 with a semimajor axis of ∼700 au (Peißker et al. 2020a), and S4711, with a semimajor axis of ∼600 au (Peißker et al. 2020b). Bortolas & Mapelli (2019) found that a population of single stars located between 0.001 pc (∼200 au) and 0.004 pc, modeled after the S-cluster stars, can generate up to a few 10^{-4} EMRIs per SN. Thus, if S0102/S55, S62, and S4711 are indicative of a larger population of stars and stellar binaries inside of 1000 au, then the EMRI rate we have found here may underestimate the true rate from this mechanism by about an order of magnitude.

Interestingly, the three different BH kick cases give very similar EMRI formation rates. This is because in our simulations most EMRIs involve an NS inspiralling into the MBH (see Figure 5). Out of EMRIs from all three BH kick cases, ∼88% are NS-EMRIs, ∼6% are BH-EMRIs, and ∼6% are WD-EMRIs.

Note that the WDs will not behave like an NS or BH EMRI because while we have a GW signal detectable by LISA while the WD is inspiralling, this signal will stop when the WD is tidally disrupted by the MBH and replaced with an EM counterpart (e.g., Sesana et al. 2008).

3.1.2. Direct Plunges

Natal kicks can results in orbits with such a high eccentricity that they cause the orbiting object to plunge directly into the MBH instead of gradually inspiralling like EMRIs. Plunging orbits satisfy

$$e > 1 - 4\frac{R_s}{a}, \tag{14}$$

where a and e are, respectively, the semimajor axis and eccentricity of the post-kick orbit, and $R_s = 2Gm_{\rm MBH}/c^2$ is the Schwarzchild radius of the MBH (e.g., Amaro-Seoane et al.

[5] Here we remind the reader that we generated 100,000 initial conditions per set of Monte Carlo simulations. To arrive at the *EMRIs (or any other outcome) per initial stellar binary* figure, we simply count the number of EMRIs (or any other outcome) in each set of simulations and divide this by 100,000.

[6] Note that these rates are about one to two orders of magnitude lower than the EMRI rate estimated via two-body relaxation processes (e.g., Hopman & Alexander 2006), and three to four orders of magnitude lower than the estimated rate of MBH binaries (Naoz et al. 2022).

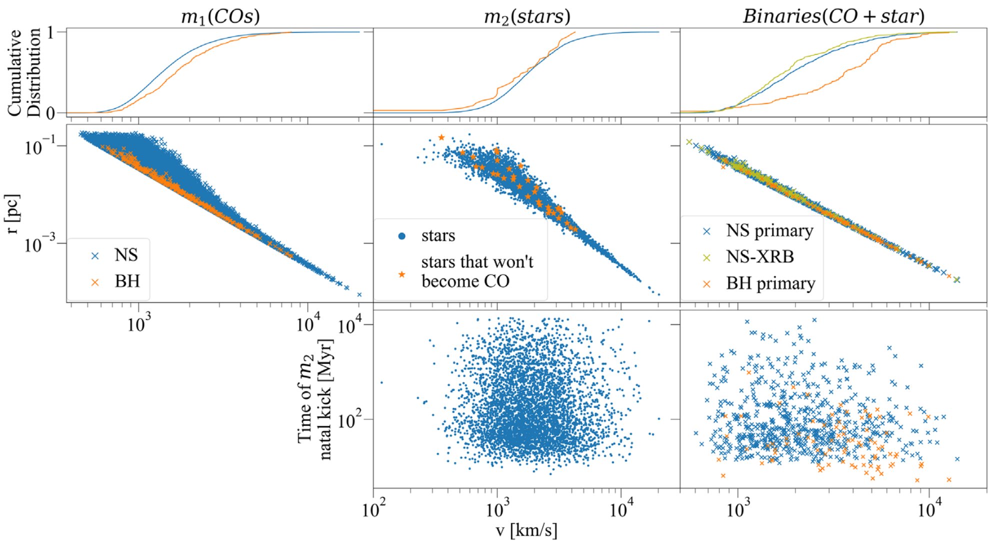

Figure 7. Objects on unbound orbits after m_1's natal kick for the slow BH kicks case. Here we show the immediately post-kick position and velocity of unbound objects (middle row), and the cumulative distribution of the velocities (top row). For the unbound stars and binaries, we also show the time at which m_2 will become a CO (bottom row). Note that this time is measured with respect to the initial stellar formation and not with respect to m_1's SN. We also show the population of unbound NS X-ray binaries in the third column.

2007). Unlike EMRIs, which emit detectable GWs for thousands of orbits, creating a coherent signal, plunges emit a brief burst of GW radiation (e.g., Yunes et al. 2008; Berry & Gair 2013). Therefore direct plunges are not expected to be detected by LISA unless originating from the Milky Way Galactic Center (Hopman & Alexander 2005). We find, in our simulations, $(1-5)\times10^{-5}$ direct plunges per initial stellar binary. The distribution of direct plunge progenitors is shown in Figure 5.

3.1.3. TDEs

TDEs will happen when the pericenter of the m_2–MBH orbit drops below the MBH tidal radius as a result of the natal kick of m_1. We also require that m_2 pass within the tidal radius before it undergoes its own natal kick to qualify as a TDE.

The tidal radius is defined as

$$r_t \sim R_*\left(\frac{m_{\rm MBH}}{m_*}\right)^{1/3}, \qquad (15)$$

where R_* is the radius of the star, given by Equation (3), and m_* is its mass (e.g., Rees 1988). We also require that r_t lie outside of the MBH Schwarzchild radius so that the star is not directly swallowed instead of being tidally disrupted. TDEs are a rare outcome in our simulations. We find 2×10^{-5} TDEs per initial stellar binary for the fast and slow kicks scenarios.

3.2. Single Objects Unbound from the MBH

Natal kicks can result in objects that are unbound from the MBH (i.e.,) on hyperbolic orbits. In our simulations, we find 0.27–0.36 single objects per initial stellar binary are unbound from the MBH after the first kick, and 0.35–0.45 after both kicks, making this the second most common orbital configuration resulting from our simulations (see Figure 3). Most objects are ejected from the inner 0.1 pc with velocities between 1000 and 10,000 km s^{-1} in our simulations, as shown by Figure 7. Despite deceleration by the combined gravitational potential of the MBH, nuclear cluster, and galaxy, objects ejected from the Galactic Center with velocities in excess of 1000 km s^{-1} should reach $r>8$ kpc with ease, and retain their high velocities (e.g., Kenyon et al. 2008).

Unfortunately, hypervelocity NSs and BHs are not observable. However, a large number of m_2's are ejected by m_1's natal kick (see Figure 7). Since $m_2<m_1$ and thus all the m_2's are still stars at the time of m_1's kick, some m_2's may be observed as HVSs. We discuss this possibility further in Section 3.2.1.

3.2.1. HVSs

If either the two members of the binary or one member of the binary becomes unbound to the MBH, it may be observed as an HVS. A large number of stars have been detected with velocities larger than the escape velocity from the galaxy and with trajectories that are consistent with a Galactic Center origin (e.g., Brown et al. 2005; Hirsch et al. 2005; Brown et al. 2007, 2009a, 2009b, 2010; Kollmeier et al. 2010; Brown et al. 2012; Boubert et al. 2018; Brown et al. 2018).

The leading channel to explain these systems has involved a binary star crossing the tidal limit and breaks up, ejecting in the process one of the members (known as the Hills mechanism, Hills 1988). The consequences of this mechanism have been explored in the literature in great detail (e.g., Gualandris et al. 2005b; Bromley et al. 2006; Perets et al. 2007; Kenyon et al. 2008; Antonini et al. 2010; Sari et al. 2010; Kobayashi et al. 2012; Zhang et al. 2013; Rossi et al. 2014). Additionally, it has been suggested that SN kicks could also contribute to the hypervelocity population (e.g., Zubovas et al. 2013; Bortolas & Mapelli 2019; Lu & Naoz 2019). In particular, Zubovas et al. (2013) predicted a characteristic spatial anisotropy for HVSs created by SN kicks. As highlighted in Figure 7, we expect to have a population of HVSs as well as hypervelocity COs after

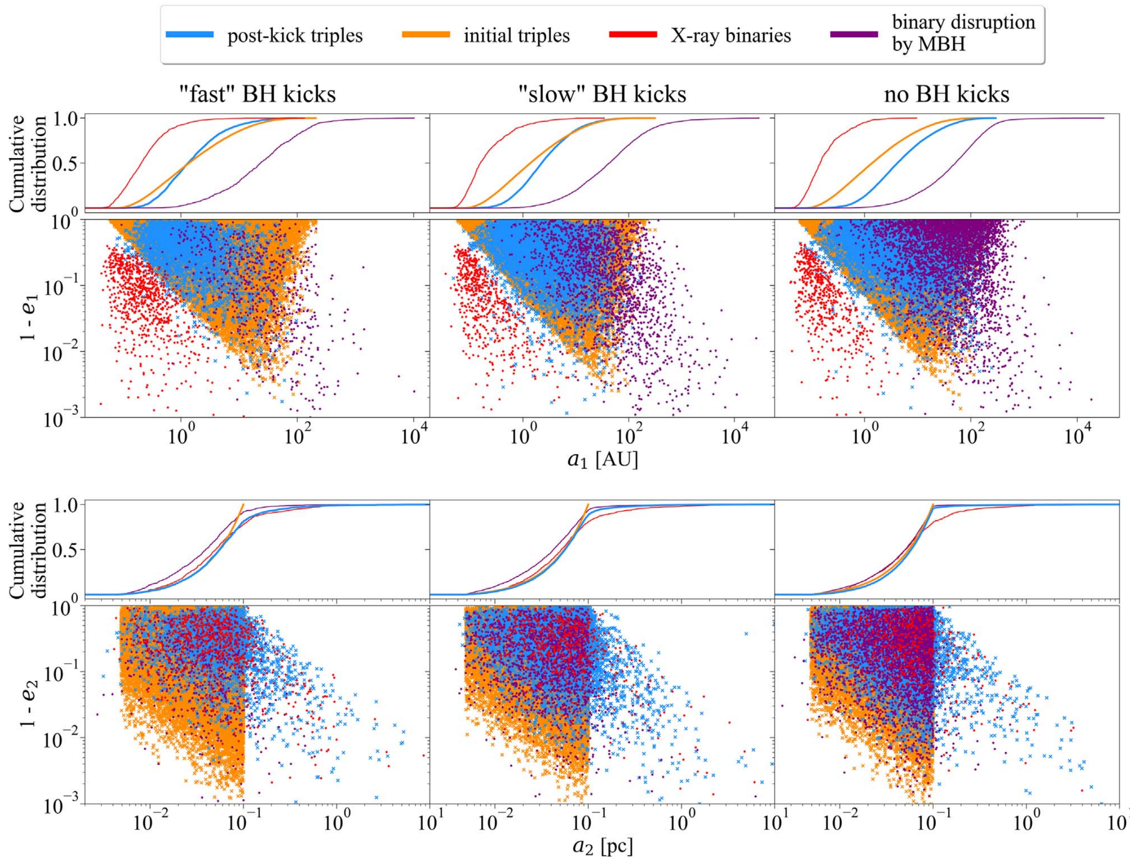

Figure 8. Distribution of triples that remain after natal kicks in the (a_1,1−e_1) plane (top plots, a_1 and e_1 are the inner binary semimajor axis and eccentricity), and the (a_2,1−e_2) plane (bottom plots, a_2 and e_2 are the outer binary semimajor axis and eccentricity). We show X-ray binaries created by m_1's natal kick in red, stable triples in blue, and binary disruptions (these are binaries that survive the natal kicks but will be disrupted by the MBH at the next pericenter passage) in purple. A fraction of the binaries in the stable triples will become GW sources.

the first natal kick. The first natal kick takes place between 4 and 45 Myr after the star formation episode, and as shown in the bottom row of Figure 7, over half of the ejected stars will not become COs until 100 Myr–10 Gyr after star formation. Combined with the fact that the majority of these stars are ejected from the inner 0.1 pc with velocities between 1000 and 10,000 km s^{-1}, a large fraction of them can be observed as HVSs outside of the Galactic Center.

4. Inner Binary Survived Natal Kicks

In the case that the inner binary survives m_1's or m_2's natal kick (or both), we have a stellar-mass binary orbiting the MBH. The orbital configurations and observables resulting from these systems are described below. We also give rates of each orbital configuration and observables from our Monte Carlo simulations. These rates are summarized in bar chart form in Figures 3 and 4, which also break down the rates by BH kick distribution.

4.1. Binaries Bound to an MBH

We find 0.1–0.29 binaries per initial binary remain bound to the MBH after one natal kick, and 0.04–0.17 after both natal kicks. We show the orbital distribution of these binaries, and their orbital distribution with respect to the MBH, in Figure 8. As highlighted in Figure 3, assuming no kicks for the BHs increase the survivable rate of binaries around the MBH. Furthermore, the number of BH-BH binaries after two kicks is inversely correlated with the strength of BH kicks. For the fast BH kick case, BH-BH comprise only 4.2% of the survived binaries. This percentage increases to 39.5% and 58.1% for the slow and no BH kicks cases, respectively. As expected, due to high natal kick magnitudes, NS-NS binaries are relatively rare in our simulations. They comprise ∼1% of all surviving binaries for the fast BH kicks case, and ∼0.2% for the two other BH kick cases.

In Figure 9 we show the distribution of orbital parameters for the surviving CO binaries for the no BH kicks case, compared to the initial binaries. We choose to highlight the no BH kicks because this is the case with the most surviving binaries. In general, we find that the surviving binaries have larger semimajor axes (a_1) than the initial binaries. Surprisingly, despite the large NS kick magnitudes, the a_1 distribution for binaries containing at least one NS (i.e NS-WD, NS-NS, and BH-NS), peaks at a smaller value than for binaries that do not (i.e., BH-WD, BH-BH). This may be because binaries that start with a smaller a_1 have a better chance of surviving high NS natal kicks. Furthermore, the binaries containing at least one NS generally have much large eccentricities (e_1) than binaries

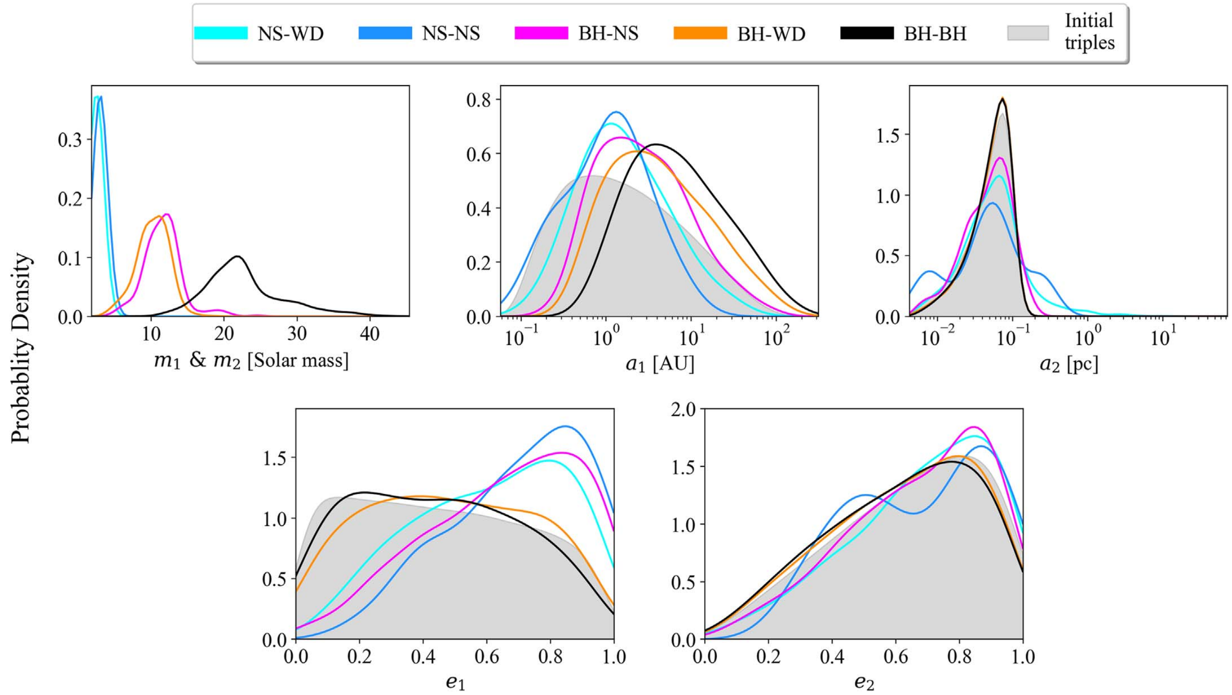

Figure 9. Distributions of CO binaries bound to MBH after both natal kicks for the no BH kicks case. The initial triple probability densities are shaded in gray for comparison. Notably, CO binaries containing at least one NS tend to be more eccentric than binaries with a BH primary due to the large NS kicks.

that do not. We find similar trends with the semimajor axis and eccentricity of the binaries' orbits around the MBH (a_2 and e_2). In general, NS containing binaries have slightly larger a_2 and e_2 than the other types of CO binaries.

These surviving binaries can undergo EKL eccentricity excitations from the MBH, which may result in GW mergers (e.g., Hoang et al. 2018; Stephan et al. 2019). We explore this effect in Section 4.1.2. We also find X-ray binaries among the surviving binaries, which we discuss in Section 4.1.1.

4.1.1. X-Ray Binary

Natal kicks can actually tighten the inner binary, causing its pericenter to drop below the binary Roche limit, creating an X-ray binary. Note that we will only get X-ray binaries after m_1's kick and not after m_2's kick, since one member of the inner binary needs to be still a star. We classify a system as a potential X-ray binary if the inner binary post-kick pericenter is below $a_{\rm Roche}$, given by Equation (2). In our simulations, we find $(6.3-9.9)\times10^{-3}$ X-ray binaries per initial stellar binary, for the no BH kicks and fast BH kicks, respectively.

In Figure 10 we show the distribution of X-ray binaries for the different kick models. Unlike Figure 8 here we divide the notation into BH X-ray binaries and NS X-ray binaries. As highlighted in Figure 10, the no BH kicks case has zero BH X-ray binaries. Thus, at face value, this implies that detecting BH X-ray binaries at the center of the galaxy may imply that the BH may have some kicks.[7]

[7] Note that other formation channels for X-ray binaries, such as EKL, (e.g., Naoz et al. 2016; Stephan et al. 2019), may form BH X-ray binaries even in the absence of BH kicks.

Interestingly, our simulations predict some X-ray binaries ejected from the Galactic Center (see Figure 7). These comprise about 20% of all X-ray binaries, for all BH kick scenarios. See Section 4.2 for further discussion.

4.1.2. GW Candidates

Natal kicks can shrink the inner binary orbit or increase the eccentricity, or nudge the binary into a part of the parameter space where EKL can excite the binary eccentricity, both scenarios leading to a shorter GW merger time. However, before a binary can merge, it can become unbound due to cumulative encounters with other stars in the cluster (Binney & Tremaine 2008). This takes place on an *evaporation* timescale of

$$t_{ev} = \frac{\sqrt{3}\,\sigma(r)}{32\sqrt{\pi}\,G\rho(r)a_1\ln\Lambda}\frac{m_1+m_2}{m_{\mathrm{m}_b}}, \qquad (16)$$

where $\ln\Lambda = 15$ is the Coulomb algorithm, $m_b = 1\,M_\odot$ is the average mass of background stars, and $\sigma(r)$ and $\rho(r)$ are given by Equations (12) and (13), respectively. Note that our orbits are very eccentric; however, as shown by Rose et al. (2020), the eccentricity may only change the evaporation timescale by a factor of a few.

There are two pathways to merger, depending on whether EKL plays a significant part. In the case where $t_{\rm EKL} > t_{\rm GR,inner}$ (given by Equations (8) and (9)), i.e., systems where GR effects dominate over EKL effects and the inner binary does not experience EKL-induced eccentricity excitations, we calculate the inner binary gravitation wave merger timescale following

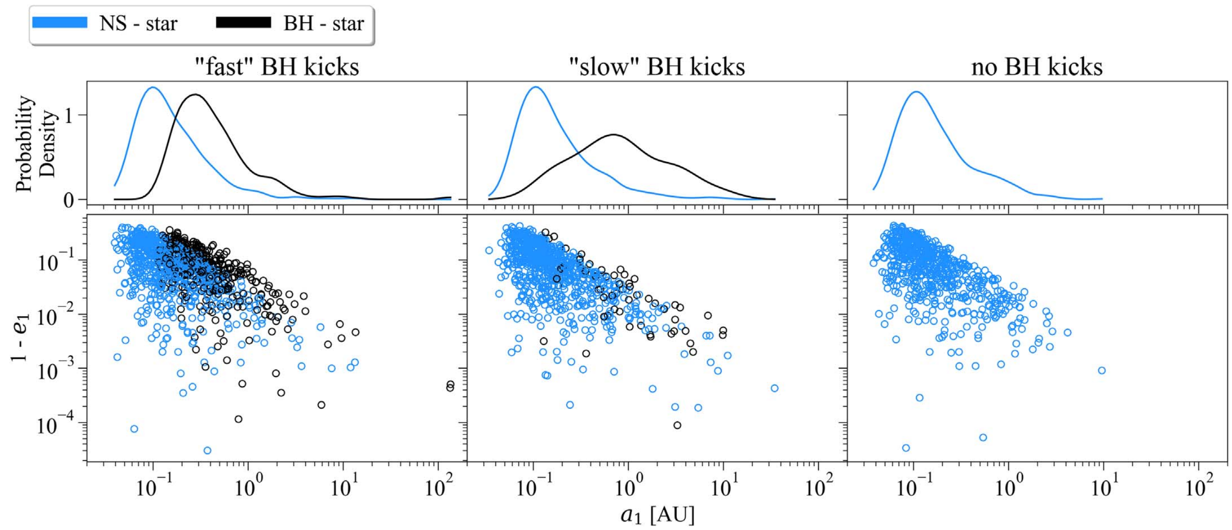

Figure 10. Distribution of X-ray binaries in the (a_1, $1-e_1$) plane (bottom three panels), and the kernel density estimation (KDE) of a_1 (top three panels). X-ray binaries with an NS (BH) primary are shown in blue (black). We show X-ray binaries from all three BH kick distribution cases. We find that the set receiving fast BH kicks resulted in the most BH-star X-ray binaries, with the set receiving no BH kicks resulting in no BH-star X-ray binaries at all. Furthermore, fast and slow BH kicks result in different semimajor axis distributions for BH-star X-ray binaries, as shown by the KDEs in the top panels. Thus, the type and semimajor axis distribution of a statistically significant population of X-ray binaries in the Galactic Center can be a diagnostic for the hitherto uncertain distribution of natal kicks received by BH progenitors.

Peters (1964):

$$t_{\rm GW} \sim \frac{5}{265}\frac{c^5 a_1^4}{G^3(m_1+m_2)m_1 m_2}(1-e^2)^{7/2}. \quad (17)$$

If $t_{\rm GW} < t_{\rm Evap}$, we denote the system as a GW merger candidate.

In the case where $t_{\rm EKL} < t_{\rm GR,inner}$, we analytically estimate the maximal EKL-induced eccentricity, $e_{1,\max}$ using the method detailed in Wen (2003), and estimate the EKL-induced GW merger time as

$$t_{\rm GW,EKL} \sim \frac{5}{265}\frac{c^5 a_1^4}{G^3(m_1+m_2)m_1 m_2}(1-e_{1,\max}^2)^3 \quad (18)$$

(e.g., Liu & Lai 2018; Randall & Xianyu 2018). Using the above method, we find $(0.17\text{–}1.2)\times10^{-3}$ GW merger candidates per initial stellar binary (see Figure 4 for breakdown by BH kick scenario). Note that this is likely an underestimate because the calculation of $e_{1,\max}$ in Wen (2003) uses the three-body Hamilton up to only the quadrupole order, and may miss octupole effects, which increases the merger rate (Hoang et al. 2018). Using the same method we used to calculate the volume rate of EMRIs as in Section 3.1.1, we find a volume rate for GW mergers facilitated by natal kicks and EKL of 0.06–0.4 Gpc^{-3} yr^{-1}.

4.2. Binaries Unbound from an MBH

Natal kicks can leave the inner binary bound while unbinding it from the MBH. In our simulations we find 0.007–0.01 binaries ejected from the MBH per initial stellar binary after one natal kick, and 0.005–0.006 after both natal kicks, making this the least common orbital configuration resulting from our simulations (see Figure 3). After both natal kicks, these unbound CO binaries are not observable. However, similarly to the ejected single objects from Section 3.2, binaries ejected from the Galactic Center after m_1's natal kick (these binaries contain one CO and one star), are observable. In the third column of Figure 7, we show the post-kick positions and velocities of these binaries after the first natal kick for the slow BH kicks case. Most of these binaries are ejected from the Galactic Center with velocities between 1000 and 10,000 km s^{-1}. These binaries are ejected from the Galactic Center between 4 and 45 Myr after the star formation episode, and ∼38% of these binaries contain a star that will not evolve to the CO phase until 100 Myr–10 Gyr after the star formation episode, giving up to a few gigayear window to observe them.

Interestingly, ∼15% (17%) (22%) of the ejected binaries are X-ray binaries, for the no BH kicks (slow BH kicks) (fast BH kicks) scenario. For the fast BH kicks scenario, 86% (14%) of the ejected X-ray binaries have an NS (BH) primary. For both of the other BH kicks scenarios all the ejected X-ray binaries have an NS primary.

Of the ejected binaries that are not X-ray binaries, ∼76% (89%)(96%) have an NS primary, for the no BH kicks (slow BH kicks) (fast BH kicks) scenario. The rest have a BH primary.

We note that some previous theoretical works have predicted the existence of HVBs (e.g., Fragione et al. 2017; Fragione & Gualandris 2018; Wang et al. 2019). Furthermore, an HVB candidate has recently been observed (Németh et al. 2016).

4.3. Binary Disruption by an MBH

In our Monte Carlo runs, we make sure that the inner binary birth distribution does not cross the Roche limit of the MBH (Equation (6)). However, sometimes the natal kick will push the inner binary onto an orbit around the MBH that does violate the condition given in Equation (6). In this case, the inner binary will be disrupted at the next pericenter passage with the

MBH. In our simulations, we find $(0.68–3.9) \times 10^{-2}$ binaries disrupted by the MBH, per initial stellar binary.

Typically, the heavier member of the inner binary is captured by (ejected from) the MBH for a bound (unbound) outer orbit, and vice versa for the lighter member (Hills 1988; Yu & Tremaine 2003; Sari et al. 2010; Kobayashi et al. 2012). Previous works have shown that captured COs and stars from these binary disruption events can result in EMRIs, plunges, or TDEs (e.g., Miller et al. 2005; Sari & Fragione 2019). We check whether this is the case for any of our binary disruptions. The inner binary is tidally disrupted by the MBH when it passes inside the tidal radius

$$r_t = a_1\left(\frac{m_{\rm MBH}}{m_1 + m_2}\right)^{1/3}. \qquad (19)$$

The newly captured object's orbit has a pericenter equal to this tidal radius. Its new semimajor axis is given by

$$a_{\rm capt} \sim a_1\left(\frac{m_{\rm MBH}}{m_1 + m_2}\right)^{2/3}. \qquad (2\ )$$

We show the probability density of the post-kick inner binary semimajor axis, and then the probability density of the captured objects in Figure 11. Because the binaries disrupted by the MBH are wide by definition (their distribution peaks at ∼100 au), the captured objects have relatively large semimajor axes with respect to the MBH (their distribution peaks at ∼1 pc). As a result, we find that none of the captured objects in our simulations result in EMRIs, plunges, and TDEs. However, they might have an effect on the stellar cusp in the inner parts of the Galactic Center (e.g., Fragione & Sari 2018).

The other binary member is typically ejected from the MBH at high velocities (e.g., Hills 1988), and may add to the number of HVSs in our simulations. However, this is beyond the scope of this paper.

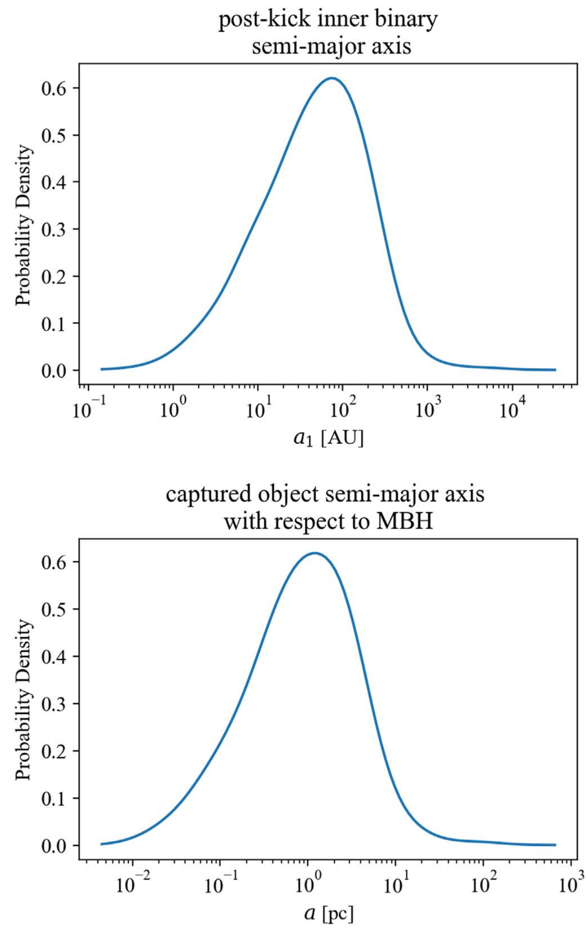

Figure 11. The semimajor axis distribution of binaries disrupted by the MBH post-natal kick (top panel), and the semimajor axis distribution of the binary component captured by the MBH (bottom panel).

5. Discussion

We have conducted an analysis of the consequences of natal kicks in massive binaries at the Galactic Center. When a star undergoes SN to become a BH or an NS it is expected to receive a large natal kick (e.g., Hansen & Phinney 1997; Lorimer et al. 1997; Cordes & Chernoff 1998; Fryer et al. 1999; Hobbs et al. 2004, 2005; Beniamini & Piran 2016).

We run three large sets of Monte Carlo simulations (100,000 for each set), calculating the dynamical outcome after an SN kick. The three sets correspond to three different kick distributions for BH progenitors: fast kicks (for which the kicks are similar to NS kicks), slow kicks (for which the kicks are normalized by the BH mass), and no kicks. The application of the kicks is done by simple vector analysis. The analytical equations are given in Lu & Naoz (2019).

Generally, after each kick there are two main outcomes, where the inner binary becomes unbound or stays bound. The second kick may also unbind a binary in the latter case. After two kicks took place we find that most of the binaries were disrupted, e.g., between 94.5% and 80.1%, for the fast to no kicks models, respectively. See Table 1 for the full details. However, even in the cases of inner binary disruption, the majority of the systems remain bound to the MBH (see Table 2). These consequences yield the following predictions and observational signatures:

Table 1
Percentage of Inner Binaries Disrupted/Survived After m_1's and m_2's Kick

BH Kick Distribution	Inner Binary Disrupted (%)		Inner Binary Survived (%)	
	Post-m_1 kick	Post-m_2 kick	Post-m_1 kick	Post-m_2 kick
Fast	88.2	94.5	11.8	5.5
Slow	73.0	88.1	27.0	11.9
None	66.7	80.1	33.3	19.9

Note. As expected, the percentage of inner binaries that survive both kicks is inversely correlated to the magnitude of BH natal kicks

1. Natal kicks create X-ray binaries at a rate of $(6.3–9.9) \times 10^{-3}$ per initial stellar binary. In general, we find that faster kicks create more X-ray binaries. In particular, we find that no BH X-ray binaries are created if we assume no BH kicks. This suggests that detecting BH X-ray binaries in the Galactic Center implies some degree of BH kicks. However, other formation channels

Table 2
Percentage of Single CO Orbits That Are Bound to/Unbound from the MBH After Both Kicks, for Different Types of COs

BH Kick Distribution	NS (%)		BH (%)		WD (%)	
	Bound	Unbound	Bound	Unbound	Bound	Unbound
Fast	67.1	32.9	67.7	32.3	91.7	8.3
Slow	65.9	34.1	96.3	3.7	91.5	8.5
None	65.7	34.3	98.3	1.7	91.1	8.9

Note. Whereas the majority of single BHs and WDs remain bound to the MBH after the natal kicks (except for the case where BHs receive fast kicks), about a third of single NSs are unbound from the MBH after natal kicks.

can create BH X-ray binaries in the absence of kicks (e.g., Naoz et al. 2016; Stephan et al. 2019).

2. HVSs and COs are a common outcome. We find that after the two kicks have taken place, a fairly significant fraction of the systems became unbound to the MBH (slightly more than 30% of NSs, and between 32.3% and 1.7% of BHs for fast to no kicks, respectively). See Table 2 for details. After the first kick, a number of stars are ejected from the inner 0.1 pc with velocities between 1000 and 10,000 km s^{-1}. Some of these stars may be observed as HVSs outside of the Galactic Center.
3. HVBs are created in addition to the ejected COs and stars, about 20% of which are X-ray binaries. These binaries are ejected from the inner 0.1 pc after the first kick with velocities between 1000 and 10,000 km s^{-1}. In particular, after the first natal kick, we find $\sim(7.4$–$9.5)\times 10^{-3}$ binaries (CO + star) ejected from the inner 0.1 pc. These may be observed as HVBs and hypervelocity X-ray binaries outside of the Galactic Center.
4. Kicks result in a steeper distribution of the bound single NSs and BHs about ~0.04 pc from the MBH compared to the initial distribution. The progenitors began on Bahcall & Wolf (1976) density profile; however, after the two kicks both the NS and the BHs (with fast kicks) result in a steeper distribution inward to 0.04 pc. At this distance from the MBH, the orbital velocity around the MBH is comparable to the average kick velocity of ~200 km s^{-1}. Beyond this radius, we find that the distribution of the NS and BHs (with fast kicks) has a shallower density distribution compared to their birth distribution. BHs with no kicks and WD (without kicks) follow the initial density distribution. This behavior is depicted in Figure 5.
5. Kicks result in a slightly shallower binary density distribution about the MBH. Unlike the steeper segregation of singles toward the MBH, the bound inner binary post kicks result in a somewhat shallower density distribution, with a long tail of systems reaching large densities. Additionally, the inner binary semimajor axis distribution after two natal kicks has a greater spread and peaks at a larger value, relative to the initial distribution.
6. Exotic events from our simulation include binary GW mergers, EMRIs, direct plunges, and TDEs. Of these, the most common are binary mergers, which occur in our simulations at a rate of $\sim(0.17-1.2)\times 10^{-3}$ per initial binary. EMRIs, direct plunges, and TDEs are much rarer events in our simulations. For each of these, we find a few times 10^{-5} events per initial binary. However, we note that our estimate of the EMRI rate is likely a conservative one due to assumptions about the inner edge of binary distribution around the MBH; see Section 3.1.1 for further discussion.

In summary, we showed that natal kicks have a significant effect on the density distribution of COs, and of binaries in the Galactic Center. For example, it produces a steeper cusp of NSs about the MBH. Additionally, natal kicks naturally give rise to HVSs, HVBs, and X-ray binaries. Interestingly, we found that X-ray binaries can serve as a discriminator between BH kick distribution models. Lastly, natal kicks can also result in a non-negligible rate of exotic events such as TDEs, LIGO, and LISA sources.

B.M.H. and S.N. acknowledge the partial support from NASA No. 80NSSC19K0321, ATP-80NSSC20K0505 and partial support from the NSF through grant No. AST-1739160. B.M.H. thanks the University of California Office of the President Dissertation Year Fellowship. S.N. thanks Howard and Astrid Preston for their generous support.

ORCID iDs

Bao-Minh Hoang https://orcid.org/0000-0003-0992-0033
Smadar Naoz https://orcid.org/0000-0002-9802-9279

References

Alexander, T., & Hopman, C. 2009, ApJ, 697, 1861
Amaro-Seoane, P., Gair, J. R., Freitag, M., et al. 2007, CQGra, 24, R113
Antognini, J. M. O. 2015, MNRAS, 452, 3610
Antonini, F., Faber, J., Gualandris, A., & Merritt, D. 2010, ApJ, 713, 90
Arzoumanian, Z., Chernoff, D. F., & Cordes, J. M. 2002, ApJ, 568, 289
Bahcall, J. N., & Wolf, R. A. 1976, ApJ, 209, 214
Bahcall, J. N., & Wolf, R. A. 1977, ApJ, 216, 883
Bartko, H., Martins, F., Trippe, S., et al. 2010, ApJ, 708, 834
Beniamini, P., & Piran, T. 2016, MNRAS, 456, 4089
Berry, C. P. L., & Gair, J. R. 2013, MNRAS, 433, 3572
Binney, J., & Tremaine, S. 2008, Galactic Dynamics (2nd ed.; Princeton, NJ: Princeton Univ. Press)
Bortolas, E., & Mapelli, M. 2019, MNRAS, 485, 2125
Bortolas, E., Mapelli, M., & Spera, M. 2017, MNRAS, 469, 1510
Boubert, D., Guillochon, J., Hawkins, K., et al. 2018, MNRAS, 479, 2789
Bromley, B. C., Kenyon, S. J., Geller, M. J., et al. 2006, ApJ, 653, 1194
Brown, W. R., Anderson, J., Gnedin, O. Y., et al. 2010, ApJL, 719, L23
Brown, W. R., Cohen, J. G., Geller, M. J., & Kenyon, S. J. 2012, ApJL, 754, L2
Brown, W. R., Geller, M. J., & Kenyon, S. J. 2009a, ApJ, 690, 1639
Brown, W. R., Geller, M. J., Kenyon, S. J., & Bromley, B. C. 2009b, ApJL, 690, L69
Brown, W. R., Geller, M. J., Kenyon, S. J., & Kurtz, M. J. 2005, ApJL, 622, L33
Brown, W. R., Geller, M. J., Kenyon, S. J., Kurtz, M. J., & Bromley, B. C. 2007, ApJ, 671, 1708
Brown, W. R., Lattanzi, M. G., Kenyon, S. J., & Geller, M. J. 2018, ApJ, 866, 39
Conselice, C. J., Blackburne, J. A., & Papovich, C. 2005, ApJ, 620, 564
Cordes, J. M., & Chernoff, D. F. 1998, ApJ, 505, 315

Danzmann, K., Amaro-Seoane, P., Audley, H., et al. 2017, LISA Mission L3 Proposal, LISA Consortium, https://www.elisascience.org/articles/lisa-mission/lisa-mission-proposal-l3
Demircan, O., & Kahraman, G. 1991, Ap&SS, 181, 313
Do, T., Ghez, A. M., Morris, M. R., et al. 2009, ApJ, 703, 1323
Do, T., Martinez, G. D., Yelda, S., et al. 2013, ApJL, 779, L6
Eggleton, P. P. 1983, ApJ, 268, 368
El-Badry, K., & Rix, H.-W. 2018, MNRAS, 480, 4884
Fabrycky, D., & Tremaine, S. 2007, ApJ, 669, 1298
Fragione, G., Capuzzo-Dolcetta, R., & Kroupa, P. 2017, MNRAS, 467, 451
Fragione, G., & Gualandris, A. 2018, MNRAS, 475, 4986
Fragione, G., & Sari, R. 2018, ApJ, 852, 51
Fragos, T., Willems, B., Kalogera, V., et al. 2009, ApJ, 697, 1057
Fryer, C. L., Woosley, S. E., & Hartmann, D. H. 1999, ApJ, 526, 152
Gautam, A. K., Do, T., Ghez, A. M., et al. 2019, ApJ, 871, 103
Genzel, R., Eisenhauer, F., & Gillessen, S. 2010, RvMP, 82, 3121
Genzel, R., Schödel, R., Ott, T., et al. 2003, ApJ, 594, 812
Ghez, A. M., Morris, M., Becklin, E. E., Tanner, A., & Kremenek, T. 2000, Natur, 407, 349
Ghez, A. M., Salim, S., Weinberg, N. N., et al. 2008, ApJ, 689, 1044
Gualandris, A., Colpi, M., Portegies Zwart, S., & Possenti, A. 2005a, ApJ, 618, 845
Gualandris, A., Portegies Zwart, S., & Sipior, M. S. 2005b, MNRAS, 363, 223
Hailey, C. J., Mori, K., Bauer, F. E., et al. 2018, Natur, 556, 70
Hamers, A. S., Bar-Or, B., Petrovich, C., & Antonini, F. 2018, ApJ, 865, 2
Hamers, A. S., & Thompson, T. A. 2019, ApJ, 882, 24
Hansen, B. M. S., & Naoz, S. 2020, MNRAS, 499, 1682
Hansen, B. M. S., & Phinney, E. S. 1997, MNRAS, 291, 569
Hills, J. G. 1988, Natur, 331, 687
Hirsch, H. A., Heber, U., O'Toole, S. J., & Bresolin, F. 2005, A&A, 444, L61
Hoang, B.-M., Naoz, S., Kocsis, B., Rasio, F. A., & Dosopoulou, F. 2018, ApJ, 856, 140
Hobbs, G., Lorimer, D. R., Lyne, A. G., & Kramer, M. 2005, MNRAS, 360, 974
Hobbs, G., Lyne, A. G., Kramer, M., Martin, C. E., & Jordan, C. 2004, MNRAS, 353, 1311
Hopman, C., & Alexander, T. 2005, ApJ, 629, 362
Hopman, C., & Alexander, T. 2006, ApJL, 645, L133
Hurley, J. R., Pols, O. R., & Tout, C. A. 2000, MNRAS, 315, 543
Jia, S., Lu, J. R., Sakai, S., et al. 2019, ApJ, 873, 9
Kalogera, V. 1996, ApJ, 471, 352
Kalogera, V. 2000, ApJ, 541, 319
Kalogera, V., Kolb, U., & King, A. R. 1998, ApJ, 504, 967
Kaspi, V. M., Bailes, M., Manchester, R. N., Stappers, B. W., & Bell, J. F. 1996, Natur, 381, 584
Kenyon, S. J., Bromley, B. C., Geller, M. J., & Brown, W. R. 2008, ApJ, 680, 312
Kobayashi, S., Hainick, Y., Sari, R., & Rossi, E. M. 2012, ApJ, 748, 105
Kocsis, B., & Tremaine, S. 2011, MNRAS, 412, 187
Kollmeier, J. A., Gould, A., Rockosi, C., et al. 2010, ApJ, 723, 812
Kormendy, J., & Ho, L. C. 2013, ARA&A, 51, 511
Kormendy, J., & Richstone, D. 1995, ARA&A, 33, 581
Kroupa, P. 2001, MNRAS, 322, 231
Lai, D., Bildsten, L., & Kaspi, V. M. 1995, ApJ, 452, 819
Li, G., Naoz, S., Holman, M., & Loeb, A. 2014a, ApJ, 791, 86
Li, G., Naoz, S., Kocsis, B., & Loeb, A. 2014b, ApJ, 785, 116
Lithwick, Y., & Naoz, S. 2011, ApJ, 742, 94
Liu, B., & Lai, D. 2018, ApJ, 863, 68
Liu, B., Muñoz, D. J., & Lai, D. 2015, MNRAS, 447, 747
Lorimer, D. R., Bailes, M., & Harrison, P. A. 1997, MNRAS, 289, 592
Lu, C. X., & Naoz, S. 2019, MNRAS, 484, 1506
Lu, J. R., Ghez, A. M., Hornstein, S. D., et al. 2009, ApJ, 690, 1463
Martins, F., Trippe, S., Paumard, T., et al. 2006, ApJL, 649, L103
Meyer, L., Ghez, A. M., Schödel, R., et al. 2012, Sci, 338, 84
Miller, M. C., Freitag, M., Hamilton, D. P., & Lauburg, V. M. 2005, ApJL, 631, L117
Miller, M. C., & Hamilton, D. P. 2002, ApJ, 576, 894
Moe, M., & Di Stefano, R. 2017, ApJS, 230, 15
Muno, M. P., Lu, J. R., Baganoff, F. K., et al. 2005, ApJ, 633, 228
Naoz, S. 2016, ARA&A, 54, 441
Naoz, S., Farr, W. M., Lithwick, Y., Rasio, F. A., & Teyssandier, J. 2013a, MNRAS, 431, 2155
Naoz, S., Fragos, T., Geller, A., Stephan, A. P., & Rasio, F. A. 2016, ApJL, 822, L24
Naoz, S., Ghez, A. M., Hees, A., et al. 2018, ApJL, 853, L24
Naoz, S., Kocsis, B., Loeb, A., & Yunes, N. 2013b, ApJ, 773, 187
Naoz, S., Rose, S. C., Michaely, E., et al. 2022, ApJL, 927, L18
Naoz, S., & Silk, J. 2014, ApJ, 795, 102
Németh, P., Ziegerer, E., Irrgang, A., et al. 2016, ApJL, 821, L13
Ott, T., Eckart, A., & Genzel, R. 1999, ApJ, 523, 248
Peißker, F., Eckart, A., & Parsa, M. 2020a, ApJ, 889, 61
Peißker, F., Eckart, A., Zajaček, M., Ali, B., & Parsa, M. 2020b, ApJ, 899, 50
Perets, H. B., Hopman, C., & Alexander, T. 2007, ApJ, 656, 709
Peters, P. C. 1964, PhRv, 136, 1224
Pfuhl, O., Alexander, T., Gillessen, S., et al. 2014, ApJ, 782, 101
Rafelski, M., Ghez, A. M., Hornstein, S. D., Lu, J. R., & Morris, M. 2007, ApJ, 659, 1241
Raghavan, D., McAlister, H. A., Henry, T. J., et al. 2010, ApJS, 190, 1
Randall, L., & Xianyu, Z.-Z. 2018, ApJ, 864, 134
Raposo-Pulido, V., & Peláez, J. 2018, A&A, 619, A129
Rees, M. J. 1988, Natur, 333, 523
Repetto, S., Davies, M. B., & Sigurdsson, S. 2012, MNRAS, 425, 2799
Rose, S. C., Naoz, S., Gautam, A. K., et al. 2020, ApJ, 904, 113
Rose, S. C., Naoz, S., & Geller, A. M. 2019, MNRAS, 488, 2480
Rossi, E. M., Kobayashi, S., & Sari, R. 2014, ApJ, 795, 125
Sana, H., de Koter, A., de Mink, S. E., et al. 2013, A&A, 550, A107
Sari, R., & Fragione, G. 2019, ApJ, 885, 24
Sari, R., Kobayashi, S., & Rossi, E. M. 2010, ApJ, 708, 605
Schödel, R., Nogueras-Lara, F., Gallego-Cano, E., et al. 2020, A&A, 641, A102
Sesana, A., Vecchio, A., Eracleous, M., & Sigurdsson, S. 2008, MNRAS, 391, 718
Stephan, A. P., Naoz, S., Ghez, A. M., et al. 2016, MNRAS, 460, 3494
Stephan, A. P., Naoz, S., Ghez, A. M., et al. 2019, ApJ, 878, 58
Tremaine, S., Gebhardt, K., Bender, R., et al. 2002, ApJ, 574, 740
Wang, Y.-H., Leigh, N., Sesana, A., & Perna, R. 2019, MNRAS, 482, 3206
Wen, L. 2003, ApJ, 598, 419
Willems, B., Henninger, M., Levin, T., et al. 2005, ApJ, 625, 324
Yelda, S., Ghez, A. M., Lu, J. R., et al. 2014, ApJ, 783, 131
Yu, Q., & Tremaine, S. 2003, ApJ, 599, 1129
Yunes, N., Sopuerta, C. F., Rubbo, L. J., & Holley-Bockelmann, K. 2008, ApJ, 675, 604
Zhang, F., Lu, Y., & Yu, Q. 2013, ApJ, 768, 153
Zubovas, K., Wynn, G. A., & Gualandris, A. 2013, ApJ, 771, 118

CHAPTER 3

Binary-SMBH Interactions: Implications for LIGO & LISA

In 2015, the Laser Interferometer Gravitational-Wave Observatory (LIGO) detected for the first time in history gravitational waves, coming from a pair of merging black holes. Other observations have quickly followed, and with them many questions about the origins of these GW mergers. The inferred rate of BBH mergers based on observations in the Second LIGO-Virgo Gravitational-wave Transient Catalog is currently $23.9^{+14.3}_{-8.6}$ $\mathrm{Gpc^{-3}yr^{-1}}$ (Abbott et al., 2021b), far greater than old theoretical estimates based on isolated binary evolution in the galactic field (e.g. Tutukov & Yungelson, 1993; Portegies Zwart & Yungelson, 1998; Bethe & Brown, 1998). As a result, many different scenarios and mechanisms— e.g. mergers in globular clusters (e.g. Miller & Hamilton, 2002; Portegies Zwart & McMillan, 2000; Rodriguez et al., 2016), mergers in AGN disks (e.g. Bartos et al., 2017; Stone et al., 2017), enhanced binary evolution (e.g. Belczynski et al., 2016; de Mink & Mandel, 2016; Mandel & de Mink, 2016), triples (e.g. Wen, 2003; Antonini & Perets, 2012) — have been proposed to explain this discrepancy. A significant part of my dissertation have focused on explaining this elevated rate of merger by exploring binary dynamics in galactic nuclei.

As shown by Hoang et al. (2022) in Chapter 2, a significant percentage of massive binary stars become BH binaries and other types of CO binaries. The gravitational push and pull of the SMBH can excite large amplitude eccentricity oscillations in binaries in galactic nuclei via the Eccentric Kozai-Lidov mechanism (e.g. Naoz, 2016). For CO binaries, these eccentricity oscillations can significantly increase the efficiency of GW emission, resulting in a much faster merger relative to an isolated binary. This mechanism is demonstrated in the first publication included in this Chapter, Hoang et al. (2018). We found that $\sim 10\%$ of

BH binaries in galactic nuclei will merge due to the gravitational influence of the SMBH. Furthermore, we found that the rate of merger for this mechanism is directly dependent on the average number of BH binaries per galactic nuclei. Assuming a steady-state number of binaries gives us a volume rate of mergers detectable by LIGO of $\sim 0.01N$ $\text{Gpc}^{-3}\ \text{yr}^{-1}$, where N is the number of BH binaries per galactic nucleus.

Since the observable rate of EKL-induced mergers is a function of the number of binaries in galactic nuclei, it can be used to constrain the latter quantity. However, this requires that we are able to distinguish GW signals from this formation channel from others. This issue is addressed in the second publication included in this Chapter, Hoang et al. (2019). Previous work have shown that only a very small percentage ($\sim 0.5\%$) of EKL-driven mergers retain their high eccentricity in the LIGO frequency band (Antonini & Perets, 2012). Fortunately, numerous studies have shown that BH binaries are detectable with the future Laser Interferometer Space Antenna (LISA), for long timescales before they merge in the LIGO frequency range (e.g. O'Leary et al., 2006; Breivik et al., 2016; Nishizawa et al., 2016; Chen & Amaro-Seoane, 2017; Nishizawa et al., 2017; Samsing & D'Orazio, 2018; D'Orazio & Samsing, 2018; Kremer et al., 2019; Randall & Xianyu, 2019).

In Hoang et al. (2019), we show a new method to identify GW signals of BH binaries undergoing EKL oscillations, in the LISA data stream. We show that EKL-induced eccentricity oscillations in BH binaries orbiting SMBH can be detected up to a few megaparsecs away. This method will allow us to estimate the rate of mergers in LIGO, and using the relation found in Hoang et al. (2018), constrain the number of binaries in galactic nuclei.

We have demonstrated this effect only for BH binaries in Hoang et al. (2019), but it can be applied to and studied for any kind of CO binaries. The third publication included in this Chapter, Deme et al. (2020) demonstrates this effect for binaries containing an IMBH. We found that EKL oscillations in a binary containing an IMBH and a stellar-mass object, induced by the SMBH, are even more detectable than those in a stellar-mass binary (i.e., have higher signal-to-noise ratios in LISA).

The Astrophysical Journal, 856:140 (10pp), 2018 April 1 https://doi.org/10.3847/1538-4357/aaafce

Black Hole Mergers in Galactic Nuclei Induced by the Eccentric Kozai–Lidov Effect

Bao-Minh Hoang[1], Smadar Naoz[1,2], Bence Kocsis[3], Frederic A. Rasio[4], and Fani Dosopoulou[4]
[1] Department of Physics and Astronomy, University of California, Los Angeles, CA 90095, USA
[2] Mani L. Bhaumik Institute for Theoretical Physics, Department of Physics and Astronomy, UCLA, Los Angeles, CA 90095, USA
[3] Institute of Physics, Eötvös University, Pázmány P. s. 1/A, Budapest, 1117, Hungary
[4] Center for Interdisciplinary Exploration and Research in Astrophysics (CIERA), Northwestern University, Evanston, IL 60201, USA
Received 2017 June 29; revised 2018 February 3; accepted 2018 February 13; published 2018 April 2

Abstract

Nuclear star clusters around a central massive black hole (MBH) are expected to be abundant in stellar black hole (BH) remnants and BH–BH binaries. These binaries form a hierarchical triple system with the central MBH, and gravitational perturbations from the MBH can cause high-eccentricity excitation in the BH–BH binary orbit. During this process, the eccentricity may approach unity, and the pericenter distance may become sufficiently small so that gravitational-wave emission drives the BH–BH binary to merge. In this work, we construct a simple proof-of-concept model for this process, and specifically, we study the eccentric Kozai–Lidov mechanism in unequal-mass, soft BH–BH binaries. Our model is based on a set of Monte Carlo simulations for BH–BH binaries in galactic nuclei, taking into account quadrupole- and octupole-level secular perturbations, general relativistic precession, and gravitational-wave emission. For a typical steady-state number of BH–BH binaries, our model predicts a total merger rate of $\sim$1–3 $\mathrm{Gpc}^{-3}\ \mathrm{yr}^{-1}$, depending on the assumed density profile in the nucleus. Thus, our mechanism could potentially compete with other dynamical formation processes for merging BH–BH binaries, such as the interactions of stellar BHs in globular clusters or in nuclear star clusters without an MBH.

Key words: black hole physics – galaxies: star clusters: general – gravitational waves – stars: kinematics and dynamics

1. Introduction

Recently, the Advanced Laser Interferometer Gravitational-Wave Observatory[5] (LIGO) has directly detected gravitational waves (GWs) from at least five inspiraling black hole–black hole (BH–BH) binaries in the universe (LIGO Scientific Collaboration & Virgo Collaboration 2016a, 2016b, 2017; Abbott et al. 2017a, 2017b). With ongoing further improvements to LIGO and the commissioning of additional instruments to VIRGO[6] and KAGRA,[7] hundreds of BH–BH binary sources may be detected within the decade, opening the era of GW astronomy (Abbott et al. 2016c).

The primary astrophysical origin of BH–BH mergers is still under debate. Merging BH binaries may be produced dynamically in dense star clusters, such as globular clusters or nuclear star clusters (NSCs) at the center of galaxies (Portegies Zwart & McMillan 2000; Wen 2003; O'Leary et al. 2006, 2009, 2016; Kocsis & Levin 2012; Antonini et al. 2014; Rodriguez et al. 2016b; Bartos et al. 2017b; Stone et al. 2017). These merging BH binaries may also be a result of isolated binary evolution in the galactic field due to special modes of stellar evolution and evolution in active galactic nuclei (Belczynski et al. 2016a; de Mink & Mandel 2016; Mandel & de Mink 2016; Marchant et al. 2016). Some studies also suggested that these LIGO detections are sourced in the first stars (Kinugawa et al. 2014, 2016; Dvorkin et al. 2016; Hartwig et al. 2016; Inayoshi et al. 2016), cores of massive stars (Reisswig et al. 2013; Loeb 2016; Woosley 2016), or in dark matter halos comprised of primordial BHs (Bird et al. 2016; Sasaki et al. 2016; Clesse & García-Bellido 2017).

Here we focus on sources produced in galactic nuclei around massive black holes (MBHs). The large escape speed in NSCs creates an ideal environment to accumulate a population of stellar mass BHs. Thus, even stellar-mass BH binaries can survive in this configuration despite supernova kicks (C. Lu & S. Naoz 2018, in preparation). Antonini & Rasio (2016) investigated the evolution of binaries in NSCs without MBHs in their centers and found a rate of 1.5 $\mathrm{Gpc}^{-3}\,\mathrm{yr}^{-1}$. Furthermore, O'Leary et al. (2009) considered binaries that form due to GW emission during close encounters between single BHs (see also Kocsis & Levin 2012; Gondán et al. 2017). In this channel, the merger rate is dominated by massive BHs over 25 $M_\odot$, which are delivered to the center by dynamical friction and relax to form steep density cusps near the MBH.[8]

We investigate the secular evolution of stellar-mass BH binaries in galactic nuclei with MBHs in their centers. These BH–BH binaries undergo large-amplitude eccentricity oscillations due to the Eccentric Kozai–Lidov (EKL; e.g., Naoz 2016) mechanism in the presence of the MBH (e.g., Antonini et al. 2010; Antonini & Perets 2012). If the eccentricity reaches a sufficiently high value, then GW emission drives the binary to merge. Antonini & Perets (2012) studied the merger rate of BH–BH binaries in the presence of MBHs in galactic nuclei and estimated the merger rates to be 1.7–4.8 $\times$ $10^{-4}\,\mathrm{Myr}^{-1}$. VanLandingham et al. (2016) studied the merger rate of BH–BH binaries in the presence of intermediate mass BHs of $\sim 10^{3-4} M_\odot$ and found it to be very high. Here we also focus on BH–BH mergers in the presence of MBHs in galactic nuclei. However, unlike Antonini & Perets (2012), who assume that the heaviest BH mass in the cluster is 10 $M_\odot$, we explore a large range of BH masses because recent LIGO observations have shown that there is a much greater range of BH masses

[5] http://www.ligo.org/
[6] http://www.virgo-gw.eu/
[7] http://gwcenter.icrr.u-tokyo.ac.jp/en/

[8] Mergers of low-mass BHs and neutron stars may be rare in this channel (Tsang 2013).

Table 1
Information About the Density Profile, Number of Monte Carlo Simulations Performed, BH Mass Distribution (the Distribution Is for Each Component of the Binary BH), Evaporation Time (t_{ev}, See Equation (3)), and Newtonian Precession (NT) for Different Simulation Runs Performed

	Profile	Number of Simulations	BH mass ($M_\odot$)	t_{ev}	NT
Nominal	GC	1000	6–100	stars	0
Runs	BW	1500	6–100	stars	0
	BW	500	5–15	stars	0
Additional	BW	1500	6–100	10 $M_\odot$ BHs	0
Runs	BW	1500	6–100	30 $M_\odot$ BHs	0
	GC	63	6–100	stars	1

Note. The first two runs listed are our nominal GC and BW runs. The last four runs listed contain various changes and additions to the two nominal runs. The t_{ev} column denotes whether the evaporation timescale is dominated by the background stars or background BHs. For the NT column, 1 means that Newtonian precession was included, and 0 means that Newtonian precession was not included.

than previously thought. EKL effects are stronger when there is a greater mass difference between the two BHs in the binary. Thus, Antonini & Perets (2012) concluded that EKL was not important and based their rate estimate on the semi-analytical timescale given in Thompson (2011), using only the quadrupole order in a multipole expansion.[9] Here we use the EKL mechanism, which represents the secular approximation up to the octupole level of approximation. Furthermore, we adopt a BH population that is consistent with a BH mass function that extends to higher masses (O'Leary et al. 2009; Kocsis & Levin 2012).

The octupole correction drives chaotic variations in the eccentricity, increases the probability of close encounters, and thus enhances the efficiency of BH–BH mergers. We show that this mechanism results in a merger rate that is higher than the rates found in the cases without MBHs, and it is coincidentally comparable to estimated globular cluster rates.

We describe our simulations in Section 2, and present our results, predictions, and merger rate in Section 3. Finally, we offer our discussions in Section 4.

2. Numerical Setup

We run several large sets of Monte Carlo simulations to investigate the effects of the SMBHs gravitational perturbations on binary BHs, with variations between sets of simulations to account for different effects (see Table 1 for details of all simulations). We study the secular dynamical evolution of binary BHs around the MBH in galactic nuclei, starting from the BH binary phase. We include the secular equations up to the octupole level of approximation (e.g., Naoz 2016), general relativity (GR) precession of the inner and outer orbits (e.g., Naoz et al. 2013), and GW emission (Peters 1964). We consider this as a simple proof-of-concept to investigate the effects of the EKL mechanism6. In general, we neglect the effects of Newtonian precession, which causes the precession of the outer orbit, and thus does not yield a suppression of the EKL mechanism (Li et al. 2015). We have rerun the merged systems via EKL processes for the Galactic Center (GC) case (see Table 1) with Newtonian precession, and demonstrated that it indeed has a negligible effect on the EKL mechanism for the physical picture we considered (see the discussion in Section 3.3).

The number of BHs, their mass distribution, and the number density are poorly known in NSCs. Theoretically, a single-mass distribution of objects forms a power-law density cusp around a massive object with $n(r) \propto r^{-1.75}$ (Bahcall & Wolf 1976), where $n(r)$ is the number density, and r is the distance from the MBH. For multi-mass distributions, lighter and heavier objects develop shallower ($\propto r^{-1.5}$) and steeper cusps (typically $\propto r^{-2}$ to $r^{-2.2}$, and r^{-3} in extreme cases), respectively (Bahcall & Wolf 1977; Freitag et al. 2006; Hopman & Alexander 2006b; Keshet et al. 2009; Aharon & Perets 2016). Recent observations of the stellar distribution in the Milky Way NSC identify a cusp with $n(r) \propto r^{-1.25}$ (Gallego-Cano et al. 2018; Schödel et al. 2018), which is consistent with the profile after a Hubble time (Baumgardt et al. 2018). As BHs are heavier than typical stars, they are expected to relax into the steeper cusps. The relaxation time of BH populations is much shorter: 0.1–1 Gyr (O'Leary et al. 2009), although it can become much longer than that in the case of a shallow stellar density profile (Dosopoulou & Antonini 2017). In this work, we assume that the BH number density follows a cusp with either $n(r) \propto r^{-2}$ or r^{-3} in our two sets of calculations.The BH mass in the two cases is set arbitrarily to 10^7 and $4 \times 10^6\, M_\odot$, respectively, and we refer to the two models as Bahcall–Wolf–like (BW) and GC examples. Note that here GC refers to the assumed MBH mass (Ghez et al. 2008) and the observed stellar distribution (see below). In reality, the cusp distribution varies with the BH mass. Thus, we have also generated initial conditions for the BW case so that β in the number density distribution, $n(r) \propto r^{-(3/2+\beta)}$, is calculated by $\beta(m) = m/4M_0$, where m is the binary mass, and M_0 is the weight average mass (e.g., Alexander & Hopman 2009; Keshet et al. 2009; Aharon & Perets 2016). We found that, due to the stability conditions, the initial condition distribution does not change significantly. For the GC case, the initial conditions' distribution will change more significantly if we allow β to vary with the mass. However, we keep $\beta = 3$ to investigate the effects of a steep number density distribution on the rates. As we will show later in this work, the choice of the number density distribution will have a very limited effect on the merger rate.

Note that $dN = 4\pi\, r^2 n(r)\, dr = 4\pi\, r^3 n(r)\, d(\ln r)$, where N is the number of objects, and thus we choose to have the initial outer binary semimajor axis follow a uniform distribution in a_2 and $\ln a_2$ in the BW and GC model, respectively. We set the minimum a_2 to be one at which the relaxation timescale equals the outer binary GW merger timescale. The maximum a_2 is chosen to be 0.1 pc, which corresponds to the value at which the EKL timescale is equal to the timescale, on which accumulated fly-bys from single stars tend to unbind the binary (see Equations (3) and (5)). However, the BH-binary semimajor axis distribution changes after applying the stability criteria (see below).

Motivated by the recent LIGO detections, in both examples, the mass of each of the BHs is chosen from a distribution uniform in logspace between 6 and 100 $M_\odot$ (i.e., $dN/dm \propto m^{-1}$; Miller 2002; Will 2004). For a comparison, we have also run additional Monte Carlo simulations in the case of the BW distribution, keeping all other parameters the

[9] The range in the rate estimation of Antonini & Perets (2012) represents core to mass-segregated distributions of the binaries and corresponds to $\sim$0.002–0.48 Gpc^{-3} yr^{-1}.

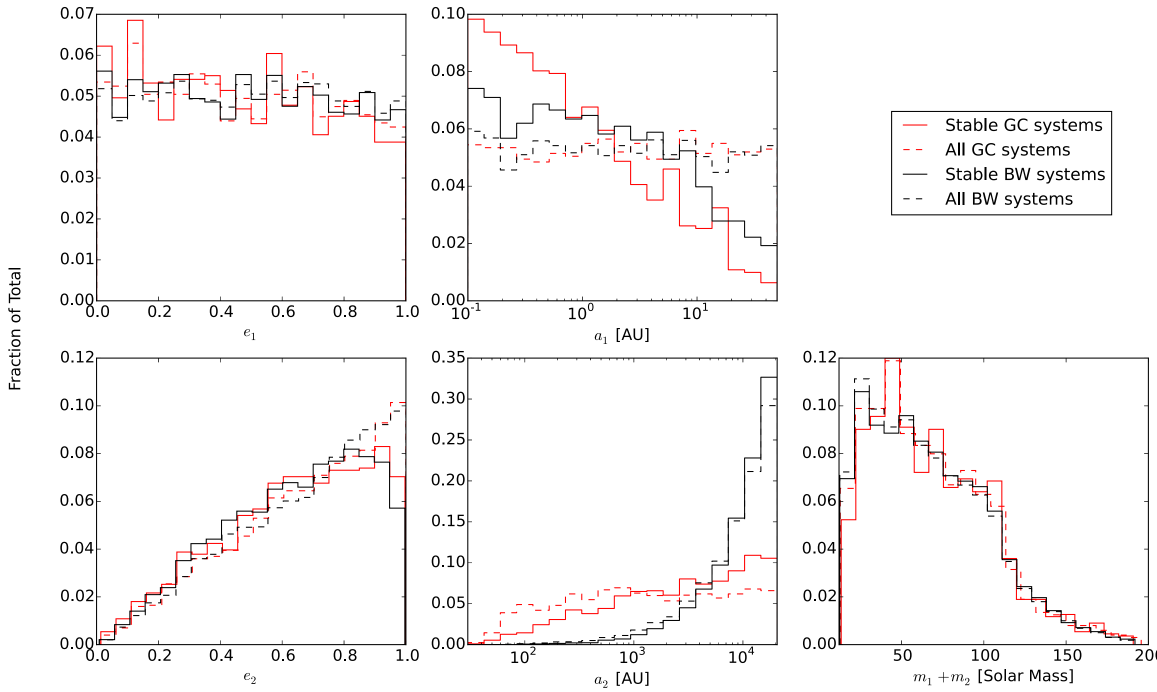

Figure 1. Distributions of the initial conditions before (dashed lines) and after (solid lines) accounting for the stability for our nominal runs. We consider the two density profiles we adopt: GC (red lines) and BW (black lines). The top and bottom rows depict the distribution of the inner and outer binaries, respectively, showing e and a from left to right. The bottom right panel shows the initial distribution of the total inner binary mass, $m_1 + m_2$. The mutual inclination is isotropic (uniform in cos(i)), and the arguments of periapsis ω_1 and ω_2 are uniform from 0 to 2π. These distributions did not change after applying the stability criterion and thus are not depicted here to avoid clutter.

same, but using a mass distribution uniform in logspace between 5 and 15 $M_\odot$ instead of 6–100 $_\odot$ (Belczynski et al. 2004). This had a negligible effect on the EKL-induced mergers (see Table 1). The binary separation a_1 is drawn from a uniform in log distribution between 0.1 and 50 au. This is consistent with Sana et al. (2012)'s distribution, which favors short period binaries, although those BHs have already gone through stellar evolution and thus their exact distribution is unknown. We note that our stability criteria largely modifies the chosen distribution and yields a steeper distribution with a cutoff for systems beyond 50 au, as shown in Figure 1 (see below). The lower limit is such as to avoid a mass transfer before the supernova took place. We note that the vast majority of our binaries are soft, with only 2% (5%) of the GC (BW) binaries being hard binaries (e.g., Quinlan 1996).

The eccentricity of the BH binaries is chosen from a uniform distribution (Raghavan et al. 2010) and takes the outer eccentricity distribution to be thermal (Jeans 1919). Furthermore, the inner and outer argument of periapsis ω_1 and ω_2 are chosen from a uniform distribution between 0 and 2π. In addition, the mutual inclination i is drawn from an isotropic distribution (uniform in cos i).

After drawing these initial conditions, we require the systems to satisfy dynamical stability, such that the hierarchical secular treatment is justified. We use two stability criteria. First we set

$$\epsilon = \frac{a_1}{a_2}\frac{e_2}{1 - e_2^2} < 0.1, \tag{1}$$

which is a measure of the relative strengths of the octupole and quadrupole level of approximations (Naoz 2016). Second, we require that the inner binary does not cross the Roche limit of the central MBH:

$$\frac{a_2}{a_1} > \left(\frac{3m_{\rm MBH}}{m_{\rm binary}}\right)^{1/3} \frac{1 + e_1}{1 - e_2}, \tag{2}$$

(e.g., Naoz & Silk 2014).[10] These stability criteria may significantly alter the distribution of BH binary systems that can survive long timescales around the MBH (similar to Stephan et al. 2016). We show the before and after stability distributions in Figure 1 for both examples. We use these distributions to initialize our runs. We note that the distribution of the angles (ω_1, Ω_2, and i) remained the same after applying the stability criteria.

The main difference between the BW and GC models is the stable outer binary semimajor axis (a_2) distribution. As depicted in Figure 1, after the stability criteria of ~80% of the BW systems remained stable, and their orbital parameter distribution did not significantly change. On the other hand, the choice of the uniform in the ln(a_2) initial distribution for the GC case resulted in a steeper distribution than the nominal Bahcall & Wolf (1976) density profile, with ~57% of the systems remaining stable. Coincidentally, this type of steeper distribution is consistent with the deprojected density profile of the disk of massive stars (Bartko et al. 2009; Lu et al. 2009). Moreover, this distribution represents a strongly mass-segregated cluster (Keshet et al. 2009).

[10] See Antonini & Perets (2012) for the quasi-secular evolution.

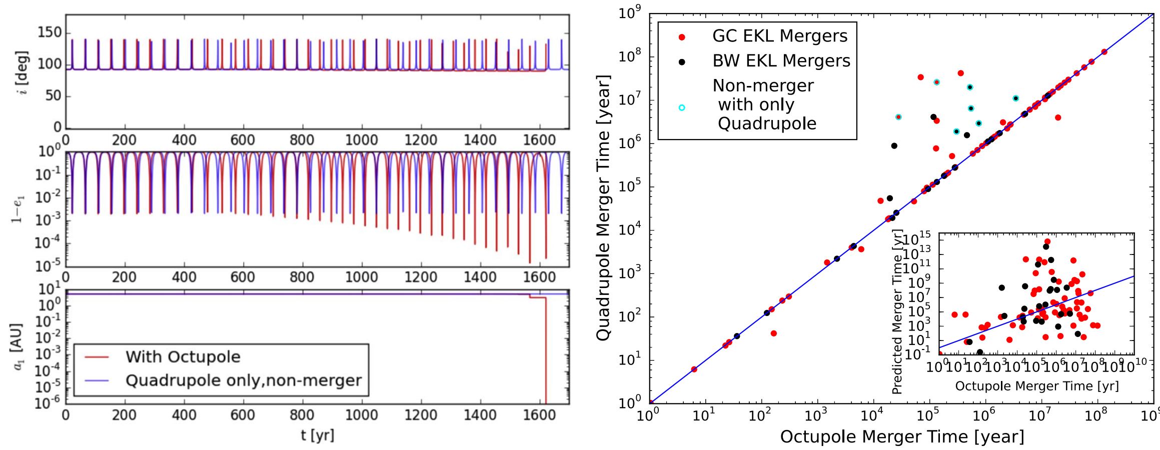

Figure 2. Left panel: time evolution of the inner binary using up to the octupole level of approximation (red) and only up to the quadrupole level of approximation (blue). The initial conditions are $m_1 = 12.8\ M_\odot$, $m_2 = 63.3\ M_\odot$, $m_{\rm MBH} = 1 \times 10^7\ M_\odot$, $a_1 = 5.1$ au, $a_2 = 936$ au, $e_1 = 0.014$, $e_2 = 0.4$, and $i = 92^\circ\!.8$. The octupole-level run results in a merger at 1623 years; whereas, the quadrupole-level run results in a non-merger. Right panel: the merger time at the quadrupole level vs. the merger time at the octupole level for the EKL-induced mergers. For 16% of the GC systems and 40% of the BW systems, the octupole level of approximation is important in predicting the correct merger time. For 2 of the GC systems and 6 of the BW systems, using only the quadrupole level of approximation results in a non-merger. These systems are shown with a cyan outline and the timescale shown on the y-axis is $t_{\rm ev}$, (see Equation (3)). The inset shows the semi-analytical merger timescale from Thompson (2011) plotted against the merger time in the Monte Carlo simulations.

Gravitational perturbations from the MBH can lead to an eccentricity excitation of the binary BH, which may lead to mergers, via the EKL mechanism (see Naoz 2016 for a review). We integrate the EKL equations (e.g., Naoz 2016), including the GR precession and GW emission for 1000 (1500) systems in the GC (BW) case either until they merge or until they become unbound, whichever happens first. The latter takes place on the order of the typical timescale, at which close encounters with other stars in the cluster cause the binary to unbind, (e.g., Binney & Tremaine 1987). This evaporation timescale has the form:

$$t_{\rm ev} = \frac{\sqrt{3}\,\sigma}{32\sqrt{\pi}\,G\rho a_1 \ln\Lambda}\frac{m_1 + m_2}{m_3}, \qquad (3)$$

where in the inner parts ($\lesssim$0.1 pc),

$$\rho = \begin{cases} 1.35 \times 10^6 M_\odot\ {\rm pc}^{-3}(a_2/0.25\ {\rm pc})^{-1.3} & {\rm GC} \\ \dfrac{3-\alpha}{2\pi}\dfrac{M_{\rm MBH}}{r^3}(G\sqrt{M_{\rm MBH}M_0}/(\sigma_0^2 r))^{-3+\alpha} & \alpha = 1.5,\ {\rm BW} \end{cases} \qquad (4)$$

(see Tremaine et al. 2002; Genzel et al. 2010, for the two cases) is the density of the surrounding stars, m_1 and m_2 are the masses of the two stellar mass BHs, m_3 is the average mass of the background stars, G is the universal gravitational constant, $\ln\Lambda$ is the Coulomb logarithm, and σ is the velocity dispersion. We adopted $\ln\ \Lambda = 15$, $\sigma = 280\ {\rm km\ s^{-1}}\sqrt{0.1\ {\rm pc}/a_2}$ and $m_3 = 1\ M_\odot$ (Kocsis & Tremaine 2011). For the BW case, $\sigma_0 = 200\ {\rm km\ s^{-1}}$ and $M_0 = 3 \times 10^8\ M_\odot$ are constants. Note that the density distributions of the background stars are flatter than the density distribution of the BHs.

In the GC case, the average evaporation timescale is about 200 Myr, but there is a very broad distribution from $\sim$1 Myr to $\sim$3 Gyr. In the BW case, the average evaporation timescale is about 120 Myr, but again there is a broad distribution from $\sim$1 Myr to $\sim$2 Gyr. Binaries that do not merge are all evaporated by 10 Gyr, which is consistent with Stephan et al. (2016).

The above evaporation time assumes that the unbinding is taking place through an interaction with the surrounding background stars. However, an interaction with background stellar mass BHs may result in different evaporation timescales. If the stellar mass BHs follow the stellar density profile in Equation (4), then the evaporation timescale is similar to the evaporation timescale due to interactions with stars, up to a numerical factor that comes from the BH mass. However, if the density profile of the stellar BHs is steeper, like the one that might be expected from mass segregation over long timescales (e.g., Keshet et al. 2009), then the evaporation timescale might be shorter. Thus, we have also calculated two representative evaporation timescales that result from steeper profiles for 10 $M_\odot$ and 30 $M_\odot$ BHs, using densities from Aharon & Perets (2016) for these background BHs (see Table 1). These evaporation timescales are much shorter, on average, than the evaporation timescales that result from the background stars, and thus the absolute number of mergers is reduced. However, the merger rate is not reduced, as explained in Section 3.3.

3. Results: EKL-induced Mergers and GW-only Mergers

3.1. Merging Channels

The EKL mechanism has been shown to play an important role in producing short period binaries and merged systems (e.g., Naoz et al. 2011; Thompson 2011; Antonini & Perets 2012; Prodan et al. 2013; Naoz & Fabrycky 2014; Prodan et al. 2015; Antonini & Rasio 2016; Naoz 2016; Naoz et al. 2016; Stephan et al. 2016). The high-eccentricity values achieved during the binary evolution lead to a shorter GW emission timescale, which may cause a merger before the binary become unbound, as shown in Figure 2. If a merger takes place due to high-eccentricity excitation, we denote this merger as an EKL-induced merger.

The eccentricity excitation due to EKL can be inhibited by GR precession if the timescale for the latter is much shorter

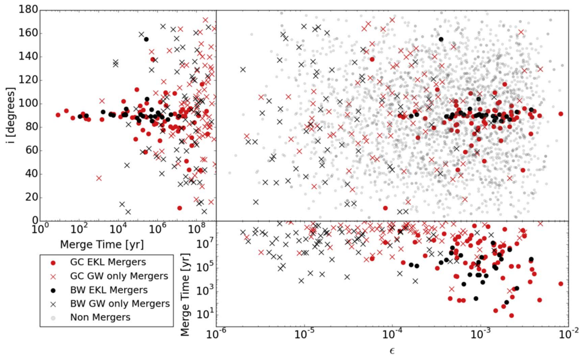

Figure 3. Main panel: the mutual inclination, i-ϵ plane, where ϵ is the hierarchy parameter (Equation (1)). We consider EKL mergers (red points), GW-only mergers (blue points), and non-mergers (gray points). Left panel: distribution of EKL-induced and GW-only mergers for mutual inclination vs. merger time. Bottom panel: distribution of EKL-induced mergers and GW-only mergers for merger time vs. ϵ.

than the former (e.g., Naoz et al. 2013). The EKL timescale at the quadrupole level of approximation is estimated as:

$$t_{\rm quad} \sim \frac{16}{30\pi}\frac{m_1+m_2+m_3}{m_3}\frac{P_2^2}{P_1}(1-e_2^2)^{3/2}, \tag{5}$$

(e.g., Antognini 2015), where P denotes the orbital period, and the GR precession of the inner orbit timescale is:

$$t_{\rm GR,inner} \sim 2\pi\frac{a_1^{5/2}c^2(1-e_1^2)}{3G^{3/2}(m_1+m_2)^{3/2}}, \tag{6}$$

(e.g., Naoz et al. 2013), where c is the speed of light. If $t_{\rm GR,inner} < t_{\rm quad}$, then the EKL effects are negligible, the binary evolves due to close encounters with other stars in the cluster, and the inspiral is caused by only GW emission. The binary may approach merger if the GW timescale, $t_{\rm GW}$, (Peters 1964) is shorter than the timescale it takes the binary to become unbound (see Equation (3)). We identify those as GW-only mergers.

In other words, we identify two channels for mergers. In the GW-only merger, we have $t_{\rm GR} < t_{\rm quad}$ and $t_{\rm ev} > t_{\rm GW}$, and in the EKL-induced merger, $t_{\rm quad} < t_{\rm GR}$, in which the eccentricity can be excited to near unity.

The EKL-induced high-eccentricity excitations usually appear in a distinctive regime in the $\epsilon - i$ parameter space. This can be seen in Figure 3, where the EKL-induced mergers inhabit a specific regime of a higher ϵ (between 10^{-4} and 10^{-2}) and relatively large inclinations.[11] The EKL-induced mergers represent $\sim$7% (1.7%) of all GC (BW) Monte Carlo systems. The systems that merge via the GW-only process (where no significant eccentricity excitations took place) occupy this parameter space uniformly. They represent about 9% (9.1%) of all the GC (BW) systems. The two sub-panels in Figure 3 show that the EKL yields a systematically shorter merger timescale. In other words, out of all systems that merged, 44% are EKL-induced mergers in the GC case, and about 16% are EKL-induced mergers for the BW density profile.

[11] Although we note that some EKL-induced mergers take place beyond the nominal Kozai angles, (i.e., $i < 40°$ and $i > 140°$), which is consistent with the near co-planar behavior (Li et al. 2014).

As implied from Figure 3, these two merger channels can yield different predictions for the statistics of BH binary mergers. The EKL-induced mergers take place preferentially in systems that are closer to the MBH (see the left panel of Figure 4), whereas the GW-only systems have no apparent trend. We note that the cutoff in GW-only mergers for $a_2 < 200$ au takes place because systems below this value either have GR precession timescales much longer than the EKL, or unbind before the binary can merge.

The EKL-induced mergers systematically happen on shorter timescales compared to the GW-only mergers (see the inset on Figure 5). On average, EKL-induced mergers in the GC case take place within about 25 Myr, while GW-only mergers merge, on average, after 296 Myr (see Figure 5 for the merger time histogram of the two channels). On the other hand, the BW case yields a shorter unbinding timescale, and thus we find that the average EKL-induced mergers in the BW is about 1 Myr, while the GW-only merger is about 166 Myr.

As expected, in both of our examples, none of the EKL-induced mergers were initially hard. On the other hand, out of all of the GW-only mergers, 14% in the GC example and 43% of the BW example, were, in fact, initially hard binaries. Hardening channels (e.g., Quinlan 1996) may result in a shorter merger time for those binaries.

3.2. The Rate Estimate

We also estimate the merger rate of BH–BH systems. The total merger rate is dominated by the merger rate of the soft binaries because the hard binaries represent a very small percentage of the total number of systems in our simulation (2% for the GC case and 5% for the BW case). Thus, we only perform the following calculations for the soft binaries.The merger rate per unit volume is defined as:

$$\Gamma_{\rm total} \;=\; n_g \Gamma f_{\rm MBH}, \tag{7}$$

where n_g is the density of galaxies, Γ is the merger rate per galaxy, and $f_{\rm MBH}$ is the fraction of galaxies containing an MBH. We adopt $n_g = 0.02\ {\rm Mpc}^{-3}$ (Conselice et al. 2005) and $f_{\rm MBH} = 0.5$ following Antonini et al. (2015a, 2015b). Note that this is a rather conservative number, and we expect this fraction to be higher.

The merger time for our systems span a very broad range of timescales with a slight systematic trend for shorter merger time closer to the MBH (i.e., a smaller a_2), as can be seen in Figure 6. However, these short-lived systems represent a small fraction of the total number of merged systems, and the apparent trend may be a result of statistical bias. To ascertain whether the merger rate has a dependency on a_2, we perform a bootstrap resampling of the merger time versus the a_2 distribution. We find that a bootstrapped analysis (both binned and not binned in a_2) yields a dependency in a_2 (see Figure 6). However, the percentage of systems close to the SMBH is small. Thus, we proceed by calculating the cumulative fraction of mergers as a function of time to calculate an average merger rate.

Figure 7 shows the cumulative fraction of merged systems as a function of time for various cases. We find that the cumulative number of merged systems fits a power law of the form:

$$N_{\rm merged} = a\ t^b, \tag{8}$$

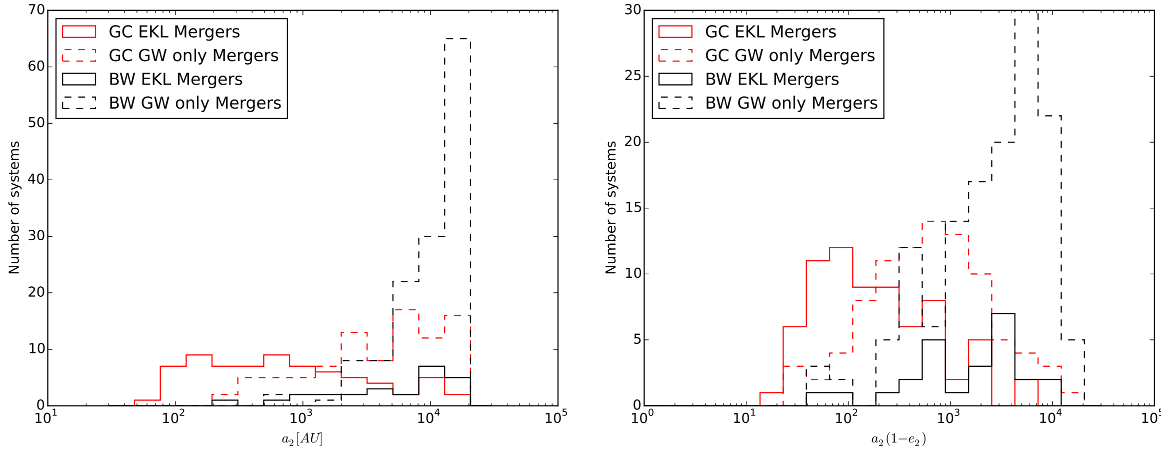

Figure 4. Left panel shows the histogram of a_2. The right panel shows the histogram of the pericenter $a_2(1-e_2)$. We consider EKL-induced (GW-only) mergers in the BW case in solid (dashed) black lines, while the GC mergers are depicted in red lines.

where a and b are constants. We perform a bootstrap resampling on the cumulative number of mergers versus merger time distribution and generated 500 resampled data sets for the GC and BW cases. We fit the above power law to all of these data sets, which gives us a range of possible fits. The average best fit values for a and b are 2.8 and 0.19 for the GC case, and 2.3 and 0.19 for the BW case. We note that we also fit a combination of different exponential functions to the cumulative number of mergers (not shown), which perhaps follows a exponential decay-like process. These fits were systematically less good, but nonetheless yield consistent results with those shown below. We can define a "half-life," $t_{1/2}$, for each sample as the time it takes for half of the systems that will merge to merge. Thus, the merger frequency at $t = t_{1/2}$ is:

$$\gamma = \frac{1}{N}\frac{dN}{dt}\bigg|_{t=t_{1/2}} = \frac{b}{t_{1/2}}. \tag{9}$$

We use this frequency as the characteristic merger frequency for each data set.

Assuming a steady-state number of BH binaries in the galactic nucleus, $N_{\rm steady}$, we can then estimate the merger rate per galaxy Γ as

$$\Gamma = N_{\rm steady} f_{\rm merge}\, \gamma, \qquad (1\ \ )$$

where $f_{\rm merge}$ is the merger fraction from our simulation, which is equal to 0.15 for the GC case and 0.07 for the BW case. $N_{\rm steady}$ is highly uncertain, so we set it to be a free parameter between 1 and 500. The right panel of Figure 7 shows the total merger rate as a function of $N_{\rm steady}$. We use a nominal value of $N_{\rm steady} = 200$ to calculate the merger rates for the GC and BW cases. We find a nominal average merger rate of $\sim$2 $\mathrm{Gpc^{-3}\,yr^{-1}}$ for both the GC and BW cases. The average merger rate values are represented by the red and black solid lines in the right panel of Figure 7; the merger rate range obtained from the bootstrap is depicted by the shaded areas.

Our estimated merger rates for the GC and BW cases are on the same order as the merger rates estimated for globular clusters, 5 $\mathrm{Gpc^{-3}\,yr^{-1}}$ (Rodriguez et al. 2016a), isolated triples in galaxies 0.14–6 $\mathrm{Gpc^{-3}\,yr^{-1}}$ (Silsbee & Tremaine 2017), and mergers following close encounters of initially unbound BHs at 0.04–3 $\mathrm{Gpc^{-3}\,yr^{-1}}$ (O'Leary et al. 2009).[12] The current LIGO/VIRGO detection constrains the total merger rate of circular BH binaries to within 12–240 $\mathrm{Gpc^{-3}\,yr^{-1}}$ (LIGO Scientific Collaboration & Virgo Collaboration 2017).

Note that Antonini & Perets's (2012) rate estimation is based on the quadrupole based a semi-analytical timescale that does not capture the system's full dynamical behavior. The octupole level of approximation used here shortens the merger timescale for 16%–40% of the EKL-induced mergers for the GC and BW distributions, respectively (see Figure 2). Furthermore, Antonini & Perets (2012) used the semi-analytical timescale given in Thompson (2011) to estimate the merger timescale. However, this does not capture the correct merger timescale for each binary BH, as can be deduced from the inset in Figure 2.

3.3. Additional Tests

As stated in Section 2, we have also considered the effects of using a narrower BH mass distribution ranging from 5 to 15 $M_\odot$ instead of 6–100 $M_\odot$ for the BW case, while keeping all other parameters the same; and the effects of using the evaporation timescale resulting from interactions with 10 $M_\odot$ and 30 $M_\odot$ background BHs instead of background stars. For the 5–15 $M_\odot$ BH mass distribution, the average evaporation time is shorter than the nominal GC and BW cases because of the reduced BH binary mass (see Equation (3) and Table 2). We performed 500 Monte Carlo simulations and found that the number of GW-only mergers are greatly reduced, due to the fact that they generally take longer to merge. However, the short-timescale EKL mergers are unaffected, and we find that using a 5–15 $M_\odot$ BH mass distribution results in a merger population that predominantly consists of short-timescale EKL mergers. We also run a set of quadrupole-only simulations for the EKL mergers in this case and found that about $\sim$25% take longer to merge than with the octupole, or do not merge at all (the total percentage of non-mergers with only quadrupole are $\sim$13%).

[12] Here we use the rates per single galaxy from O'Leary et al. (2009) in Table 1 and multiply by $\xi = 10$ and $n_g = 0.02$ $\mathrm{Mpc^{-3}}$. However, that mechanism is weakly sensitive to the NSC and MBH mass. Dwarf galaxies dominate the rates with a much higher n_g.

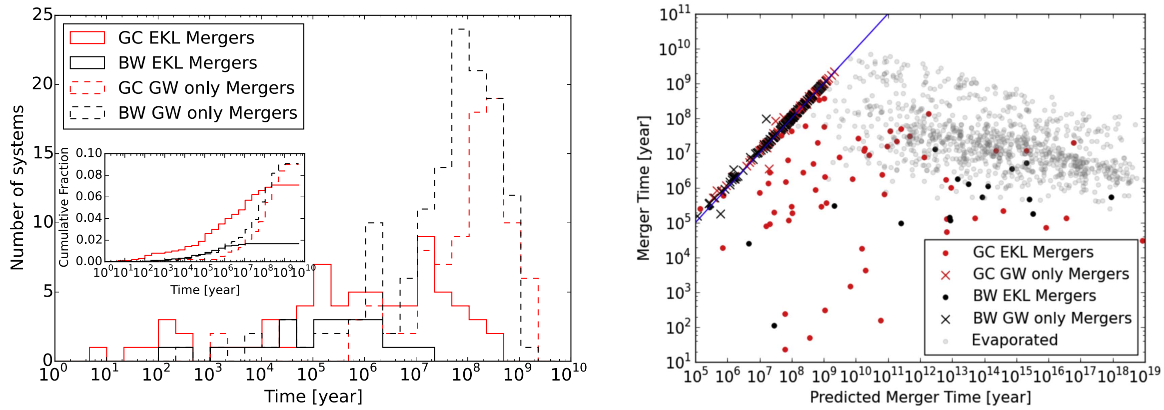

Figure 5. GW timescale comparison between different channels. Left panel: the histogram of merger times for EKL mergers (red lines) and GW-only mergers (blue lines). The inset shows the cumulative distribution function of merger times. Right panel: the actual merger timescale as a function of the GW timescale given the initial condition of the simulation. The GW-only mergers (blue points) follow the expected 1 : 1 line, while most of the EKL-induced merger times are shorter. The gray points never merge, and their y-axis value marks their unbinding timescale.

Fitting Equation (8) to the number of mergers as a function of time results in a shorter merger half-life (this can be seen from the left panel of Figure 7), and therefore a higher merger frequency, as defined in Equation (9). Thus, performing the calculation for $\Gamma_{\rm tot}$ results in a merger rate that is higher than before, as can be seen in the right panel of Figure 7. This makes sense, considering that a majority of the mergers in this case are EKL mergers that take place very quickly. However, a shorter average evaporation timescale and average merger timescale for a fixed steady-state number of binaries also means that we require a quicker BH binary replenishment mechanism (on a timescale roughly equal to the average evaporation and average merger timescale) to maintain steady-state. Otherwise the high rate of merger seen in Figure 7 cannot be maintained. For this particular case, a replenishment timescale of about 10 Myr is required to maintain steady state.

We have a similar consequence resulting from using the evaporation timescales from interactions with background BHs of masses 10 $M_\odot$ and 30 $M_\odot$ rather than background stars. To do this, we first calculate the new evaporation timescales using the number densities for 10 $M_\odot$ and 30 $M_\odot$ found in Aharon & Perets (2016), then we compare the merger time of each of our soft binaries with the new evaporation timescales, and if the merger time is longer, we count it as a non-merger. We then fit the new merger distributions as a function of time to Equation (8) as was done previously, and then calculate $\Gamma_{\rm tot}$ as a function of $N_{\rm steady}$, as shown in the right panel of Figure 7. We find that using the evaporation timescale dominated by the 10 $M_\odot$ BHs results in a merger rate that is very similar to the nominal BW and GC cases, but using the evaporation timescale dominated by the 30 $M_\odot$ BHs results in a much higher merger rate than before (see right panel of Figure 7). In the 30 $M_\odot$ background BHs case, the average evaporation timescale is very short compared to the nominal GC and BW cases (see Table 2). Similar to what happened with the 5–15 $M_\odot$ BH mass distribution, only BH binaries with short merger timescales can merge before they are evaporated, so the average merger timescale is very short, leading to a higher $\Gamma_{\rm tot}$. Furthermore, like in the 5–15 $M_\odot$ BH mass distribution case, this higher $\Gamma_{\rm tot}$ will require a shorter binary replenishment timescale (roughly 1 Myr) to continue in the steady state with a fixed number of BHs. For the 10 $M_\odot$ background BHs case, the average evaporation timescale is very similar to the the average evaporation timescale in the nominal GC and BW cases (see Table 2). Thus, the average merger timescale is very similar to before, leading to a similar $\Gamma_{\rm tot}$. Note that since the evaporation timescale has a weak dependence on perturber mass, the significantly shorter evaporation timescale resulting from the 30 $M_\odot$ is primarily a consequence of their steeper density profile as compared to the 10 $M_\odot$ background BHs.

Finally, we have also rerun our EKL mergers run in the GC case with the Newtonian precession added. First, one should differentiate between the Newtonian precession that occurs due to a spherical mass distribution (which was what we assumed in this work) versus the precession due to deviations from spherical symmetry, as explored in Petrovich & Antonini (2017). Thus, in the following analysis, we constrain ourselves to the spherically symmetric Newtonian precession. The Newtonian precession in our case causes the outer orbit to precess. While it may take place on a timescale similar to the octupole timescale, it will not affect the inner orbit precession, which has a much greater effect on the EKL mechanism. However, to quantify how much Newtonian precession will affect our systems, we rerun the 63 EKL mergers for the GC case with the Newtonian precession included, following Equation (44) of Tremaine (2005). We found that over 90% of these runs remained mergers even with the Newtonian precession included. Furthermore, the merger time distribution remains the same.

4. Discussion

We investigated the secular evolution of stellar mass BH binaries in the neighborhood of the MBH in galactic nuclei using Monte Carlo simulations. Our equations included the hierarchical secular effects up to the octupole level of approximation (the so-called EKL mechanism; Naoz 2016), the general relativity precession of the inner and outer orbits, and GW emission between the two stellar BHs. During their evolution, binary stellar mass BHs may undergo large eccentricity excitations, which can drive them to merge (see, for example, Figure 2). While BHs are expected to segregate toward the center of the galactic nuclei, the power-law index of

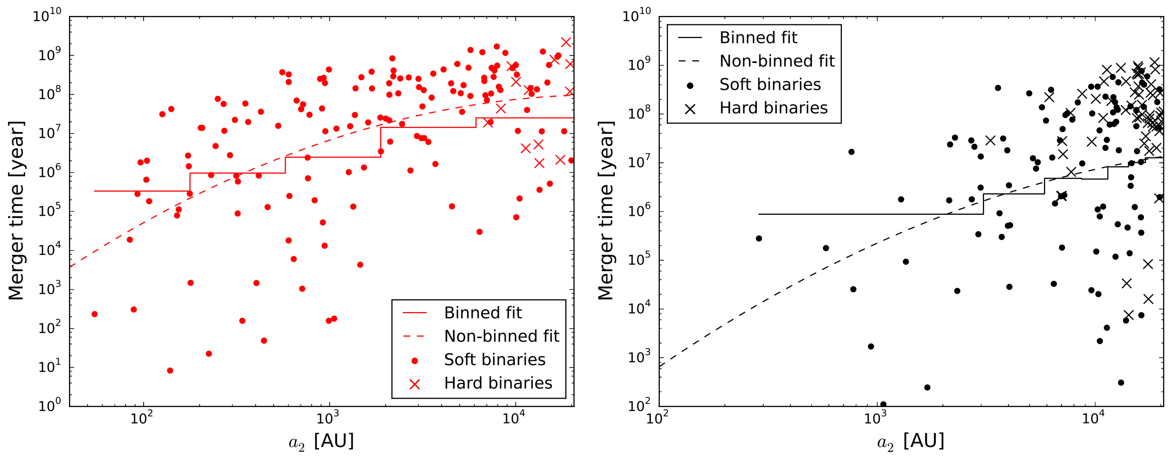

Figure 6. Merger time of soft and hard binaries as a function of outer binary separation a_2 for the GC case (left panel), and the BW case (right panel). We perform both a binned (solid line) and not binned (dashed line) bootstrap fit to the data and find a slight dependence of the merger time on a_2.

the number density of the cusp is still uncertain. As a proof-of-concept, we explored two cases: r^{-2}, denoted as BW; and r^{-3}, denoted as GC. We find a consistent merger rate in both cases.

We identified two channels for BH–BH mergers. In the first type of merger, the general relativity precession timescale is shorter than the quadrupole timescale, suppressing eccentricity excitations. However, the initial GW merger timescale is shorter than the evaporation timescale, leading to a merger. We call these GW-only mergers. These systems will merge in the absence of an MBH in the center of a galaxy. For the second type of merger, the EKL mechanism produces large eccentricity oscillations in the inner binary orbit, driving the binary BHs to merge. We call these EKL-induced mergers.

GW-only and EKL-induced mergers occupy different parts of the parameter space for both number density profiles we examined. Specifically, consider the $\epsilon - i$ parameter space, where ϵ is given by Equation (1). EKL-induced mergers will preferentially occupy a regime of high ϵ and is close to 90° mutual inclination. On the other hand, GW-only mergers are uniformly spread in i and $\ln(\epsilon)$ (see Figure 3). This yields a prediction for the merger distribution as a function of distance from the MBH; the EKL-induced mergers will be systematically closer to the MBH. This is depicted in Figure 4.

Finally, we estimate the total merger rate to be at the order of unity of $\mathrm{Gpc}^{-3}\ \mathrm{yr}^{-1}$ and perhaps even higher. This rate is coincidentally comparable to the estimated merger rate in globular clusters, which suggests that galactic nuclei may host a significant fraction of the BH–BH mergers. Note that Antonini & Rasio (2016) showed that if the natal kick of BH binaries is higher than 50 km s^{-1}, then the efficiency of forming BH binaries in globular clusters is suppressed significantly (Chatterjee et al. 2017),[13] and BH mergers in NSCs dominate over mergers in globular clusters. We note that if natal kicks are smaller, so that BH binaries form efficiently in globular clusters, then BH mergers in NSC with an MBH are still comparable to that of globular clusters.

Our results suggest that the key parameter controlling the merger rate is the steady-state number of BH–BH binaries. We find that, for typical BH–BH binary populations often assumed in the literature, the predicted merger rate is $\sim$1–3 $\mathrm{Gpc}^{-3}\ \mathrm{yr}^{-1}$; but this can become much higher, depending on the exact assumptions made (see Figure 7). Our steady-state assumption requires a binary replenishment mechanism, without which the EKL-induced BH–BH merger rate would rapidly decay (as implied from Figure 5).The BH–BH binary population in real systems may be replenished from the outside: for example, from globular clusters that spiral in, or from nearby star formation (e.g., Hopman & Alexander 2006a, 2006b; Gnedin et al. 2014; Antonini et al. 2015a; Aharon & Perets 2016). A different channel for recent in situ formations of BH–BH binaries may exist near the centers of E + A (or post-starburst) galaxies (e.g., Dressler & Gunn 1983). These galaxies are special because it appears that they underwent a star formation episode that terminated abruptly $\sim$1 Gyr ago. Thus, this population may hold recent BH–BH binaries near their nuclei. While these galaxies are a relatively rare subtype of elliptical galaxies, they may increase the stellar mass of the galaxy by $\sim$10% (e.g., Swinbank et al. 2012). Thus, due to their recent star formation and overdensity in the nuclei, these galaxies were linked to an enhancement of tidal disruption events (e.g., Arcavi et al. 2014; Stone & van Velzen 2016). Therefore, these galaxies may have an overabundance of BH binaries, which can cause enhancement of BH–BH mergers. Recently, Bartos et al. (2017a) showed that with a big enough sample of observed BH–BH mergers, a certain BH–BH merger channel can be statistically correlated with rare galaxy types, including E + A galaxies. This may prove a valuable test for our model in the future.

The BH–BH merger scenario presented here, in our proof-of-concept examples, suggests that MBH gravitational perturbations can enhance the merger rate. Since these mergers take place close to the SMBH, the acceleration of the binary around the SMBH may cause a detectable Doppler shift of the waveform (Inayoshi et al. 2017; Meiron et al. 2017). Furthermore, a GW echo of the binary BH merger caused by the SMBH may be detectable (Kocsis 2013). We have provided the parameter space at which these mergers take place and demonstrated that they occupy a different part of the parameter space. This suggests that this channel may be statistically distinguished with a sufficiently large sample of mergers (B.-M. Hoang et al. 2018, in preparation).

[13] Also above this natal kick, the mergers of isolated binaries are significantly suppressed (Belczynski et al. 2016b).

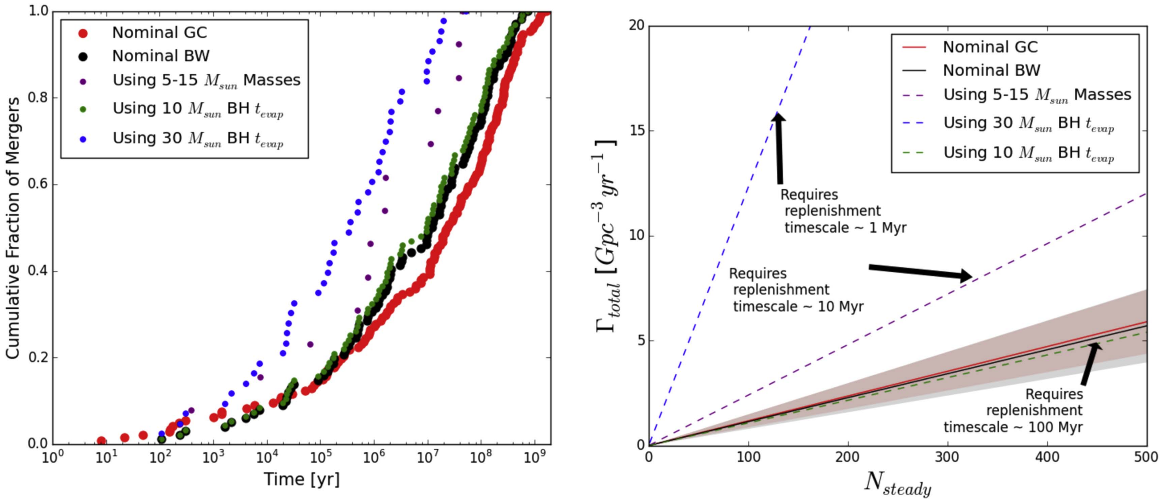

Figure 7. Left panel: scatter points show the cumulative fraction of mergers as a function of time for the GC case (red), the BW case (black), using a 5–15 $M_\odot$ mass distribution (purple), using an evaporation timescale dominated by 10 $M_\odot$ BHs (green) and using an evaporation timescale dominated by 30 $M_\odot$ BHs (blue). Cases that take a shorter time to reach a cumulative merger fraction of unity have a shorter average merger time and therefore a higher total merger rate, as shown in the right panel. Right panel: the total merger rate $\Gamma_{\rm total}$ as a function of the number of steady-state BH–BH binaries in the galactic nucleus $N_{\rm steady}$ for the various cases in the left panel. The shaded areas show upper and lower limits to the GC and BW rates corresponding to the bootstrap distribution. Also shown are the approximate BH binary replenishment timescales required to maintain the merger rates shown. The two shorter replenishment timescales, 10 Myr and 1 Myr, are probably unlikely to take place. Thus, the rate represented by the nominal GC and BW cases, which require a replenishment timescale of 100 Myr, is the most likely scenario.

Table 2
The Table above Lists the Average Evaporation Timescale, the Inverse of the Merger Frequency γ as Defined in Equation (9), and the Merger Fraction for Each of the Cases Shown in Figure 7

Case	$\langle t_{\rm evap}\rangle$ (yr)	$1/\gamma$ (yr)	$f_{\rm merge}$
Nominal GC	2.1×10^8	1.3×10^8	0.15
Nominal BW	1.2×10^8	6.3×10^7	0.07
BW, 5–15 $M_\odot$ BBH	7.7×10^7	1.1×10^7	0.03
BW, 10 $M_\odot$ BHt_{evap}	1.0×10^8	6.3×10^7	0.07
BW, 30 $M_\odot$ BHt_{evap}	5.9×10^6	2.5×10^6	0.03

Note. As can be seen from the table, a shorter average evaporation timescale means a shorter average merger timescale ($1/\gamma$) and a smaller merger fraction $f_{\rm merge}$. The binary replenishment timescale required for steady state is roughly on the same order of magnitude as the average evaporation and merger timescales.

Finally, motivated by the calculation of the rate of BH–BH mergers for > 0.1 pc by Petrovich & Antonini (2017), we follow their set of assumptions for a compact object formation rate between 2×10^{-5} and 10^{-4} yr^{-1}, with a fraction of surviving BH–BH binaries of 2.5%–4.5%. The merger fraction from Petrovich & Antonini (2017), along with these assumptions, yields a merger rate of 0.6–15 Gpc^{-3} yr^{-1}. Similarly, with our merger fraction and these assumptions, we find a merger rate of 0.7–14 Gpc^{-3} yr^{-1} for our < 0.1 pc regime. Therefore, assuming that these assumptions are correct, we conclude that the BH–BH merger rate in the proximity of galactic nuclei can be as significant as $\sim$30 Gpc^{-3} yr^{-1}.

We thank Michael Fitzgerald for insightful discussions about statistical analysis. B.M.H. acknowledges the support of the Eugene V. Cota-Robles Fellowship and the Graduate Dean's Scholar Award. S.N. acknowledges partial support from a Sloan Foundation Fellowship. F.A.R. and F.D. acknowledge support from NASA Grant NNX14AP92G and NSF Grant AST-1716762 at Northwestern University. This project has received funding from the European Research Council (ERC) under the European Union's Horizon 2020 research and innovation programme under grant agreement No. 638435 (GalNUC) and by the Hungarian National Research, Development, and Innovation Office grant NKFIH KH-125675.

ORCID iDs

Bao-Minh Hoang https://orcid.org/0000-0003-0992-0033
Smadar Naoz https://orcid.org/0000-0002-9802-9279
Frederic A. Rasio https://orcid.org/0000-0002-7132-418X
Fani Dosopoulou https://orcid.org/0000-0003-0657-3902

References

Abbott, B. P., Abbott, R., Abbott, T. D., et al. 2016a, PhRvX, 6, 041015
Abbott, B. P., Abbott, R., Abbott, T. D., et al. 2016b, PhRvL, 116, 061102
Abbott, B. P., Abbott, R., Abbott, T. D., et al. 2016c, Phys. Rev. D, 93, 122003
Abbott, B. P., Abbott, R., Abbott, T. D., et al. 2017a, PhRvL, 119, 141101
Abbott, B. P., Abbott, R., Abbott, T. D., et al. 2017b, ApJ, 851, L35
Aharon, D., & Perets, H. B. 2016, ApJL, 830, L1
Alexander, T., & Hopman, C. 2009, ApJ, 697, 1861
Antognini, J. M. O. 2015, MNRAS, 452, 3610
Antonini, F., Barausse, E., & Silk, J. 2015a, ApJ, 812, 72
Antonini, F., Barausse, E., & Silk, J. 2015b, ApJL, 806, L8
Antonini, F., Faber, J., Gualandris, A., & Merritt, D. 2010, ApJ, 713, 90
Antonini, F., Murray, N., & Mikkola, S. 2014, ApJ, 781, 45
Antonini, F., & Perets, H. B. 2012, ApJ, 757, 27
Antonini, F., & Rasio, F. A. 2016, ApJ, 831, 187
Arcavi, I., Gal-Yam, A., Sullivan, M., et al. 2014, ApJ, 793, 38
Bahcall, J. N., & Wolf, R. A. 1976, ApJ, 209, 214
Bahcall, J. N., & Wolf, R. A. 1977, ApJ, 216, 883
Bartko, H., Martins, F., Fritz, T. K., et al. 2009, ApJ, 697, 1741
Bartos, I., Haiman, Z., Marka, Z., et al. 2017a, NatCo, 8, 831
Bartos, I., Kocsis, B., Haiman, Z., & Márka, S. 2017b, ApJ, 835, 165
Baumgardt, H., Amaro-Seoane, P., & Schödel, R. 2018, A&A, 609, A28

Belczynski, K., Holz, D. E., Bulik, T., & O'Shaughnessy, R. 2016a, Nature, 534, 512
Belczynski, K., Repetto, S., Holz, D. E., et al. 2016b, ApJ, 819, 108
Belczynski, K., Sadowski, A., & Rasio, F. A. 2004, ApJ, 611, 1068
Binney, J., & Tremaine, S. 1987, Dynamics (Princeton, NJ: Princeton Univ. Press)
Bird, S., Cholis, I., Muñoz, J. B., et al. 2016, PhRvL, 116, 201301
Chang, P. 2009, MNRAS, 393, 224
Chatterjee, S., Rodriguez, C. L., & Rasio, F. A. 2017, ApJ, 834, 68
Clesse, S., & García-Bellido, J. 2017, PDU, 15, 142
Conselice, C. J., Blackburne, J. A., & Papovich, C. 2005, ApJ, 620, 564
de Mink, S. E., & Mandel, I. 2016, MNRAS, 460, 3545
Dosopoulou, F., & Antonini, F. 2017, ApJ, 840, 31
Dressler, A., & Gunn, J. E. 1983, ApJ, 270, 7
Dvorkin, I., Vangioni, E., Silk, J., Uzan, J.-P., & Olive, K. A. 2016, MNRAS, 461, 3877
Freitag, M., Amaro-Seoane, P., & Kalogera, V. 2006, ApJ, 649, 91
Gallego-Cano, E., Schödel, R., Dong, H., et al. 2018, A&A, 609, A26
Genzel, R., Eisenhauer, F., & Gillessen, S. 2010, RvMP, 82, 3121
Ghez, A. M., Salim, S., Weinberg, N. N., et al. 2008, ApJ, 689, 1044
Gnedin, O. Y., Ostriker, J. P., & Tremaine, S. 2014, ApJ, 785, 71
Gondán, L., Kocsis, B., Raffai, P., & Frei, Z. 2017, arXiv:1711.09989
Hartwig, T., Volonteri, M., Bromm, V., et al. 2016, MNRAS, 460, L74
Hopman, C. 2009, ApJ, 700, 1933
Hopman, C., & Alexander, T. 2006a, ApJ, 645, 1152
Hopman, C., & Alexander, T. 2006b, ApJL, 645, L133
Inayoshi, K., Kashiyama, K., Visbal, E., & Haiman, Z. 2016, MNRAS, 461, 2722
Inayoshi, K., Tamanini, N., Caprini, C., & Haiman, Z. 2017, PhRvD, 96, 063014
Jeans, J. H. 1919, MNRAS, 79, 408
Keshet, U., Hopman, C., & Alexander, T. 2009, ApJL, 698, L64
Kinugawa, T., Inayoshi, K., Hotokezaka, K., Nakauchi, D., & Nakamura, T. 2014, MNRAS, 442, 2963
Kinugawa, T., Miyamoto, A., Kanda, N., & Nakamura, T. 2016, MNRAS, 456, 1093
Kocsis, B. 2013, ApJ, 763, 122
Kocsis, B., & Levin, J. 2012, PhRvD, 85, 123005
Kocsis, B., & Tremaine, S. 2011, MNRAS, 412, 187
Li, G., Naoz, S., Kocsis, B., & Loeb, A. 2014, ApJ, 785, 116
Li, G., Naoz, S., Kocsis, B., & Loeb, A. 2015, MNRAS, 451, 1341
LIGO Scientific Collaboration, & Virgo Collaboration 2016a, PhRvL, 116, 241103
LIGO Scientific Collaboration, & Virgo Collaboration 2016b, PhRvL, 116, 061102
LIGO Scientific Collaboration, & Virgo Collaboration 2017, PhRvL, 118, 221101
Loeb, A. 2016, ApJL, 819, L21
Lu, J. R., Ghez, A. M., Hornstein, S. D., et al. 2009, ApJ, 690, 1463
Mandel, I., & de Mink, S. E. 2016, MNRAS, 458, 2634
Marchant, P., Langer, N., Podsiadlowski, P., Tauris, T. M., & Moriya, T. J. 2016, A&A, 588, A50
Meiron, Y., Kocsis, B., & Loeb, A. 2017, ApJ, 834, 200
Miller, M. C. 2002, ApJ, 581, 438
Naoz, S. 2016, ARA&A, 54, 441
Naoz, S., & Fabrycky, D. C. 2014, ApJ, 793, 137
Naoz, S., Farr, W. M., Lithwick, Y., Rasio, F. A., & Teyssandier, J. 2011, Natur, 473, 187
Naoz, S., Fragos, T., Geller, A., Stephan, A. P., & Rasio, F. A. 2016, ApJL, 822, L24
Naoz, S., Kocsis, B., Loeb, A., & Yunes, N. 2013, ApJ, 773, 187
Naoz, S., & Silk, J. 2014, ApJ, 795, 102
O'Leary, R. M., Kocsis, B., & Loeb, A. 2009, MNRAS, 395, 2127
O'Leary, R. M., Meiron, Y., & Kocsis, B. 2016, ApJ, 824, L12
O'Leary, R. M., Rasio, F. A., Fregeau, J. M., Ivanova, N., & O'Shaughnessy, R. 2006, ApJ, 637, 937
Peters, P. C. 1964, PhRv, 136, 1224
Petrovich, C., & Antonini, F. 2017, ApJ, 846, 146
Portegies Zwart, S. F., & McMillan, S. L. W. 2000, ApJL, 528, L17
Prodan, S., Antonini, F., & Perets, H. B. 2015, ApJ, 799, 118
Prodan, S., Murray, N., & Thompson, T. A. 2013, arXiv:1305.2191
Quinlan, G. D. 1996, NA, 1, 35
Raghavan, D., McAlister, H. A., Henry, T. J., et al. 2010, ApJS, 190, 1
Rauch, K. P., & Tremaine, S. 1996, NewA, 1, 149
Reisswig, C., Ott, C. D., Abdikamalov, E., et al. 2013, PhRvL, 111, 151101
Rodriguez, C. L., Chatterjee, S., & Rasio, F. A. 2016a, PhRvD, 93, 084029
Rodriguez, C. L., Morscher, M., Wang, L., et al. 2016b, MNRAS, 463, 2109
Sana, H., de Mink, S. E., de Koter, A., et al. 2012, Sci, 337, 444
Sasaki, M., Suyama, T., Tanaka, T., & Yokoyama, S. 2016, PhRvL, 117, 061101
Schödel, R., Gallego-Cano, E., Dong, H., et al. 2018, A&A, 609, A27
Silsbee, K., & Tremaine, S. 2017, ApJ, 836, 39
Sridhar, S., & Touma, J. R. 2016, MNRAS, 458, 4143
Stephan, A. P., Naoz, S., Ghez, A. M., et al. 2016, MNRAS, 460, 3494
Stone, N. C., Metzger, B. D., & Haiman, Z. 2017, MNRAS, 464, 946
Stone, N. C., & van Velzen, S. 2016, ApJL, 825, L14
Swinbank, A. M., Balogh, M. L., Bower, R. G., et al. 2012, MNRAS, 420, 672
Thompson, T. A. 2011, ApJ, 741, 82
Tremaine, S. 2005, ApJ, 625, 143
Tremaine, S., Gebhardt, K., Bender, R., et al. 2002, ApJ, 574, 740
Tsang, D. 2013, ApJ, 777, 103
VanLandingham, J. H., Miller, M. C., Hamilton, D. P., & Richardson, D. C. 2016, ApJ, 828, 77
Wen, L. 2003, ApJ, 598, 419
Will, C. M. 2004, ApJ, 611, 1080
Woosley, S. E. 2016, ApJ, 824, L10

THE ASTROPHYSICAL JOURNAL LETTERS, 875:L31 (6pp), 2019 April 20 https://doi.org/10.3847/2041-8213/ab14f7

Detecting Supermassive Black Hole–induced Binary Eccentricity Oscillations with LISA

Bao-Minh Hoang[1,2], Smadar Naoz[1,2], Bence Kocsis[3], Will M. Farr[4,5], and Jessica McIver[6]
[1] Department of Physics and Astronomy, University of California, Los Angeles, CA 90095, USA; bmhoang@astro.ucla.edu
[2] Mani L. Bhaumik Institute for Theoretical Physics, Department of Physics and Astronomy, UCLA, Los Angeles, CA 90095, USA
[3] Institute of Physics, Eötvös University, Pázmány P.s. 1/A, Budapest, 1117, Hungary
[4] Department of Physics and Astronomy, Stony Brook University, Stony Brook, NY 11794, USA
[5] Center for Computational Astrophysics, Flatiron Institute, 162 Fifth Avenue, New York, NY 10010, USA
[6] LIGO Laboratory—California Institute of Technology, Pasadena, CA 91125, USA
Received 2019 March 1; revised 2019 March 31; accepted 2019 April 1; published 2019 April 24

Abstract

Stellar-mass black hole binaries (BHBs) near supermassive black holes (SMBH) in galactic nuclei undergo eccentricity oscillations due to gravitational perturbations from the SMBH. Previous works have shown that this channel can contribute to the overall BHB merger rate detected by the Laser Interferometer Gravitational-Wave Observatory (LIGO) and Virgo Interferometer. Significantly, the SMBH gravitational perturbations on the binary's orbit may produce eccentric BHBs which are expected to be visible using the upcoming Laser Interferometer Space Antenna (LISA) for a large fraction of their lifetime before they merge in the LIGO/Virgo band. For a proof of concept, we show that the eccentricity oscillations of these binaries can be detected with LISA for BHBs in the local universe up to a few megaparsecs, with observation periods shorter than the mission lifetime, thereby disentangling this merger channel from others. The approach presented here is straightforward to apply to a wide variety of compact object binaries with a tertiary companion.

Key words: galaxies: nuclei – Galaxy: center – gravitational waves – quasars: supermassive black holes – stars: black holes – stars: kinematics and dynamics

1. Introduction

The recent detection of gravitational-wave (GW) emission from a merging neutron star binary (Abbott et al. 2017d) and merging black hole binaries (BHBs; Abbott et al. 2016a, 2016b, 2017a, 2017b, 2017c; The LIGO Scientific Collaboration & The Virgo Collaboration 2018) by the Laser Interferometer Gravitational-Wave Observatory (LIGO)/Virgo have ushered in an exciting new era of GW astrophysics. The astrophysical origin of the detected mergers is currently under debate, with numerous explanations proposed. These explanations can be very roughly divided into two main categories: mergers due to isolated binary evolution (e.g., Belczynski et al. 2016; de Mink & Mandel 2016; Mandel & de Mink 2016; Marchant et al. 2016), and mergers due to dynamical interactions (e.g., Portegies Zwart & McMillan 2000; Wen 2003; O'Leary et al. 2006, 2009, 2016; Antonini & Perets 2012; Kocsis & Levin 2012; Antonini et al. 2014; Antonini & Rasio 2016; Rodriguez et al. 2016; VanLandingham et al. 2016; Askar et al. 2017; Arca-Sedda & Gualandris 2018; Fragione & Kocsis 2018; Hoang et al. 2018; Randall & Xianyu 2018; Arca-Sedda & Capuzzo-Dolcetta 2019). Orbital eccentricity has been explored as a way to distinguish between these merger channels in both the LIGO/Virgo and Laser Interferometer Space Antenna (LISA) frequency bands. In contrast to mergers from isolated binary evolution, merging binaries from dynamical channels have been shown to have measurable eccentricities when they enter the LISA and/or LIGO/Virgo band, and can potentially be used as a way to distinguish between channels (e.g., O'Leary et al. 2009; Cholis et al. 2016; Gondán et al. 2018; Lower et al. 2018; Randall & Xianyu 2018; Rodriguez et al. 2018; Samsing 2018; Zevin et al. 2019). Unlike LIGO/Virgo, which can only detect merging BHBs in the final inspiral phase before merger, LISA will be able to detect eccentric stellar-mass BHBs for long timescales before they merge in the LIGO/Virgo band (e.g., O'Leary et al. 2006; Breivik et al. 2016; Nishizawa et al. 2016; Chen & Amaro-Seoane 2017; Nishizawa et al. 2017; D'Orazio & Samsing 2018; Kremer et al. 2019; Samsing & D'Orazio 2018). This provides us with invaluable insight into the dynamical evolution of eccentric binaries leading up to the merger, which has important implications about the astrophysical context in which merging binaries evolve.

It has been shown that tight binaries orbiting a third body on a much wider outer orbit (a hierarchical triple) can undergo large eccentricity oscillations on timescales longer than the BHB orbital timescale due to gravitational perturbations from the tertiary—the so-called eccentric Kozai–Lidov (EKL) mechanism (e.g., Kozai 1962; Lidov 1962; Naoz 2016). In the case of BHBs orbiting a supermassive black holes (SMBH), high eccentricities can lead to a faster merger via GW emission (e.g., Wen 2003; Antonini et al. 2014; Hoang et al. 2018). Furthermore, this BHB merger channel has been shown to possibly contribute to the overall merger rate at levels comparable to other dynamical channels of mergers (Hamers et al. 2018; Hoang et al. 2018). Before they merge, these binaries spend a long time (10^{2-9} yr) oscillating between high and low eccentricities (e.g., Hoang et al. 2018).

Eccentric binaries emit GWs over a wide range of frequencies that approximately peak at a frequency of $f_p(a, e) = (1 + e)^{1/2} (1 - e)^{-3/2} f_{\rm orb}(a)$, with $f_{\rm orb}(a) = (2\pi)^{-1}\sqrt{G(m_1 + m_2)}\,a^{-3/2}$, where m_1 and m_2 are the BHB component masses (we consider mass components of $m_1 = 30\,M_\odot$ and $m_2 = 20\,M_\odot$ for the rest of the Letter, which fall well within the mass distribution detected by LIGO/Virgo; The LIGO Scientific Collaboration & The Virgo Collaboration 2018), a is the semimajor axis, e is the orbital eccentricity, and G is the gravitational constant (e.g., O'Leary et al. 2009). In the left panels of Figure 1 we show the time evolution of f_p for two representative BHBs undergoing eccentricity oscillations while orbiting an SMBH with a mass of

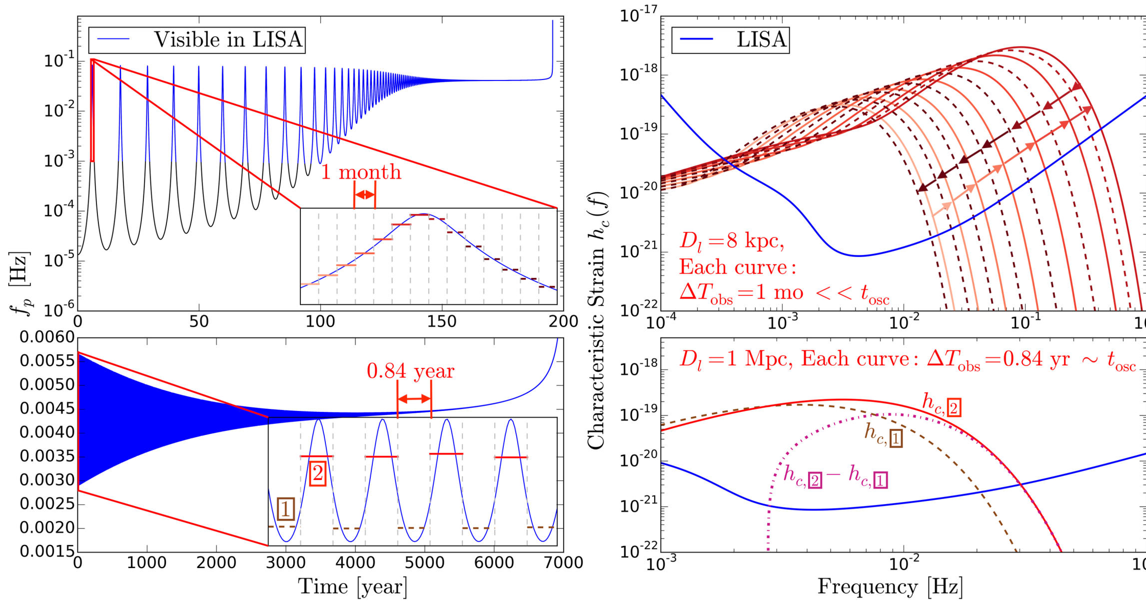

Figure 1. Two examples of stellar-mass BHBs near an SMBH that exhibits strain oscillations in the LISA band. Left panels: the time evolution of the pericenter frequency of two systems undergoing EKL cycles and GW emission. The initial parameters of the top (bottom) binary are $m_1 = 30\,M_\odot$, $m_2 = 20\,M_\odot$, $m_\bullet = 4 \times 10^6\,M_\odot$ ($1 \times 10^7\,M_\odot$), $a = 0.15$ (0.046 au), $a_{\rm out} = 250$ au, $e = 0.5$ (0.96), $e_{\rm out} = 0.9$, $i = 88°$ (90°), $g = 0°$ (135°), and $g_{\rm out} = 0°$. We place the top (bottom) system at a distance D_l of 8 kpc (1 Mpc). The proximity of the top system means that it is resolvable with an observation time interval $\Delta T_{\rm obs}$ that is much shorter than the eccentricity oscillation timescale. In contrast, the distance of the bottom system means that a $\Delta T_{\rm obs}$ longer than the eccentricity oscillation timescale is required to resolve the system. This difference of timescales results in two different observables: in the first case the evolution of the average f_p observed per $\Delta T_{\rm obs}$ tracks the evolution of the actual f_p (see the inset of top left panel); in the second case, if $\Delta T_{\rm obs}$ is a half integer multiple of the eccentricity oscillation timescale, the average f_p observed per $\Delta T_{\rm obs}$ oscillates (see the inset of bottom left panel). Right panels: characteristic strain oscillations of the corresponding left panel systems. Top: the first solid strain line has an S/N ~ 170. The strain moves to the right as the eccentricity increases (red solid lines), and moves back to the left as the eccentricity decreases due to EKL (red dashed lines). The left panel of the figure shows that this effect can be seen whenever the eccentricity is pumped up to extremal values throughout the binary's life. Bottom: the brown dashed line $h_{c,1}$ has an S/N of ~13 and the observed average f_p oscillates between two values, as shown by the two strain curves $h_{c,1}$ and $h_{c,2}$ (dashed and solid lines, respectively). We have also plotted the difference of the two strains $h_{c,2} - h_{c,1}$ (purple dotted–dashed line), which lies well above the LISA sensitivity curve and has an S/N of ~6.4.

$m_\bullet = 4 \times 10^6\,M_\odot (1 \times 10^7\,M_\odot)$, on an outer orbit of semimajor axis $a_{\rm out} = 250$ au, and eccentricity $e_{\rm out} = 0.9$. As can be seen from the figure, these BHBs are visible using LISA for a substantial part of their lifetime, providing an unprecedented opportunity for the study of their dynamics. We show in this Letter that the eccentricity oscillations they undergo are detectable with LISA with observational intervals $\Delta T_{\rm obs}$ shorter than the proposed LISA mission lifetime of 4 yr (Danzmann et al. 2017), thereby revealing their astrophysical origin[7]

2. Two Regimes of Detectable Eccentricity Oscillations

To illustrate the detectability of eccentricity oscillations in GW data, we divide the GW data stream into segments of time duration $\Delta T_{\rm obs}$. Generally, to accumulate a sufficient amount of signal-to-noise (S/N) within individual $\Delta T_{\rm obs}$ intervals, relatively short $\Delta T_{\rm obs}$ is sufficient to resolve systems with small D_l, where D_l is the luminosity distance of the BHB; conversely, much longer $\Delta T_{\rm obs}$ is required to resolve systems with large D_l. This dichotomy results in two distinct types of observable eccentricity oscillations depending on the ratio of $\Delta T_{\rm obs}$ to the timescale on which the eccentricity oscillates, $t_{\rm osc}$, which depends on both EKL and general relativistic effects (e.g., Naoz et al. 2013b; Antognini 2015; Naoz 2016; Randall & Xianyu 2018). In practice we do not calculate $t_{\rm osc}$, but simply calculate from numerical simulations the value of $\Delta T_{\rm obs}$ which will maximize the detectability of eccentricity oscillations (details are given later in this Letter).

Here we focus on two cases:

1. $\Delta T_{\rm obs} \ll t_{\rm osc}$. For BHBs at small luminosity distances D_l, the S/N accumulates rapidly and we can divide the data stream into short $\Delta T_{\rm obs}$ intervals that are much smaller than $t_{\rm osc}$ and measure the eccentricity separately for each interval. If the change in eccentricity between successive intervals is larger than the eccentricity measurement accuracy in each interval, the evolution of eccentricity can be detected by comparing the eccentricities in different observation intervals. We show an example of this in the top panels of Figure 1, with a BHB 8 kpc away, with the data stream divided into intervals of $\Delta T_{\rm obs} = 1$ month.
2. $\Delta T_{\rm obs} \sim t_{\rm osc}$ or $\Delta T_{\rm obs} > t_{\rm osc}$. For BHBs at greater D_l with weaker GWs, the data stream must be processed in longer $\Delta T_{\rm obs}$ intervals, that may be comparable to or larger than

[7] We note that while finalizing this manuscript, an independent study by Randall & Xianyu (2019) addressed the potential for detecting EKL oscillations with LISA for BHBs in triples. In our proof-of-concept work, we focus specifically on BHBs around an SMBH, and show that these EKL oscillations are indeed significant enough to be detected by LISA. We provide a method that will allow distinguishing a BHB near a tertiary mass, and also between systems with dynamics dominated by GW emission and those that are EKL dominated.

$t_{\rm osc}$. In this case, the eccentricity evolution cannot be measured as accurately as in the $\Delta T_{\rm obs} \ll t_{\rm osc}$ case. Nevertheless, the eccentricity variation between different $\Delta T_{\rm obs}$ intervals may still cause a significant change in the GW waveform that can be measured. In the bottom panels of Figure 1 we show eccentricity oscillations in a BHB 1 Mpc away, with the data stream divided into intervals of $\Delta T_{\rm obs} = 0.84$ yr ($\sim 1/2$ times the t_{osc} of the BHB). The change in the GW signal is well above the LISA noise.

Below we quantify the parameter space where stellar-mass BHBs are resolvable with LISA, and where their eccentricity oscillations are large enough to be detectable with LISA.

3. Detectability of Eccentric Stellar-mass BHBs with LISA

Unlike circular binaries, which emit GWs at a single frequency, equal to twice the orbital frequency, eccentric binaries emit at a wide range of orbital frequency harmonics. The complex GW dimensionless strain $h(a, e, t)$ of a binary of semimajor axis a and eccentricity e is then the sum of the strains at each orbital frequency harmonic $f_n = nf_{\rm orb}$ (Peters & Mathews 1963). We follow the calculation of the GW strain from (Kocsis et al. 2012), where $h(a, e, t)$ is defined as

$$h(a, e, t) = \sum_{n=1}^{\infty} h_n(a, e, f_n)\exp(2\pi i f_n t), \tag{1}$$

where

$$h_n(a, e, f_n) = \frac{2}{n}\sqrt{g(n, e)}\, h_0(a), \tag{2}$$

with $h_0(a)$ representing the dimensionless strain amplitude for circular binary orbit with masses m_1 and m_2 at a luminosity distance of D_l, averaged over the binary orientation, i.e.,

$$h_0(a) = \sqrt{\frac{32}{5}}\frac{G^2}{c^4}\frac{m_1 m_2}{D_l a}, \tag{3}$$

where c is the speed of light and $g(n, e)$ is defined as

$$g(n, e) = \frac{n^4}{32}\Bigg[\left(J_{n-2} - 2eJ_{n-1} + \frac{2}{n}J_n + 2eJ_{n+1} - J_{n+2}\right)^2 + (1 - e^2)(J_{n-2} - 2J_n + J_{n+2})^2 + \frac{4}{3n^2}J_n^2\Bigg], \tag{4}$$

where J_i is the ith Bessel function evaluated at ne (Peters & Mathews 1963). We have neglected a factor of $(1 + z)^2$ in $h_0(a)$ that accounts for the effects of Doppler shift due to the peculiar velocity of the source and cosmological redshift. The effects of peculiar velocity and redshift are equivalent to a change of apparent distance and object masses (Kocsis et al. 2006). However, since the furthest luminosity distances considered in this Letter are a few megaparsecs, the corresponding redshift z is very small and we do not expect this effect to significantly alter our results.

We may crudely approximate the characteristic strain of an evolving eccentric binary using the Fourier transform of a stationary binary as

$$h_c^2(a, e, f) = 4f^2|\tilde{h}(a, e, f)|^2 \times \min\left(1, \frac{f_n}{\dot{f}_n}\frac{1}{\Delta T_{\rm obs}}\right), \tag{5}$$

where $\tilde{h}(a, e, f)$ is the Fourier transform of Equation (1) over an observational period of $\Delta T_{\rm obs}$, and the factor inside the minimum function accounts for the fact that the signal power actually only accumulates for a time of $\min(\Delta T_{\rm obs}, f_n/\dot{f}_n)$ in each frequency bin as a and e vary slowly (Cutler & Flanagan 1994; Flanagan & Hughes 1998). We show $h_c(f)$ in the right panels of Figure 1 for the corresponding systems in the left panels. As can be seen from these figures, the strain spectrum will visibly oscillate with different f_p peak frequency due to the underlying eccentricity oscillations.

We note that a hallmark feature of EKL is oscillations in i—the inclination of the binary angular momentum vector with respect to the angular momentum vector of the outer orbit—that are out of phase with oscillations in e (e.g., Naoz 2016). Furthermore, as LISA orbits around the Sun, the angle between the BHB angular momentum and the line of the sight will also change. These combined effects result in variations in the binary inclination with respect to the line of sight, which we have neglected in the calculation above. However, variations in binary inclination will only modulate the amplitude of the signal without changing f_p. Thus, changes in f_p due to changes in e will still be detectable. Furthermore, the signal amplitude modulations due to oscillations in i may themselves be used to indicate the presence of EKL. Another effect that we have neglected in our strain calculation is the precession of the BHB pericenter due to both EKL and general relativity. Pericenter precession, like inclination oscillations, does not effect f_p, so we do not expect it to significantly alter the conclusions of this Letter. However, it will change the polarization of the waveform, which may also independently indicate the presence of EKL. We leave these considerations to a future study.

To quantify the parameter space where these binaries are detectable in LISA, we compute the S/N as a function of a and e as (e.g., Robson et al. 2018)

$$\mathrm{S/N}^2(a, e) = \int \frac{h_c^2(a, e, f)}{f^2 S_n(f)}df, \tag{6}$$

where $S_n(f)$ is the effective noise power spectral density of the detector, weighted by the sky and polarization-averaged signal response function of the instrument (e.g., Equation (1) in Robson et al. 2018). In the case that the LISA mission lifetime is extended to 10 yr (e.g., Danzmann et al. 2017), and assuming that at least two $\Delta T_{\rm obs}$ intervals are required to detect a change in eccentricity, we pick a maximum possible $\Delta T_{\rm obs}$ of 5 yr. Furthermore, we set the threshold for resolvability at S/N = 5. In Figure 2 we show in green the region in a and $1 - e$ parameter space of the inner binary where $\mathrm{S/N} \geqslant 5$ is achievable for $\Delta T_{\rm obs} \leqslant 5$ yr, for $D_l = 8$ kpc and $D_l = 1$ Mpc, respectively. In this initial S/N calculation we have neglected eccentricity evolution due to EKL.

4. Detectability of Eccentricity Evolution

Having established the parameter space where eccentric stellar-mass BHBs are visible to LISA, we now quantify LISA's ability to detect eccentricity changes in these binaries. We do this by finding the parameter space where the change in

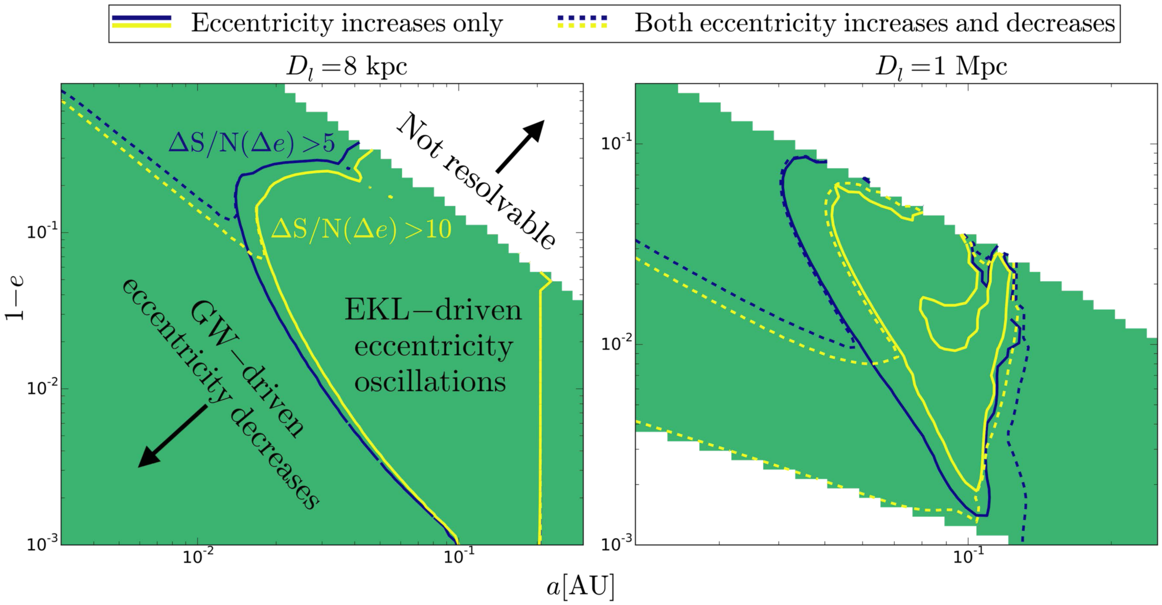

Figure 2. Map of the parameter space where SMBH-induced eccentricity oscillations are visible with LISA. In the left (right) panel we show the case for $D_l = 8$ kpc ($D_l = 1$ Mpc). The green area shows where systems are resolvable with $S/N \geqslant 5$ for $\Delta T_{\rm obs} \leqslant 5$ yr. Each BHB is placed on an orbit of $a_{\rm out} = 250$ au and $e_{\rm out} = 0.9$ around a SMBH with a mass of $m_\bullet = 4 \times 10^6 (1 \times 10^7)$ $M_\odot$ for the $D_l = 8$ kpc ($D_l = 1$ Mpc) case. The blue (yellow) contours enclose the areas where eccentricity changes are detectable at the level of $\Delta S/N(\Delta e) > 5$ (10). The solid contours enclose only the parameter space where the eccentricity increases between consecutive $\Delta T_{\rm obs}$ intervals (due to SMBH-induced EKL) are detectable. The dashed contours enclose the parameter space where both eccentricity increases and decreases are detectable. The eccentricity decrease can either be caused by GW emission or by EKL oscillations, which occupy two distinct regions of the parameter space (see plot labels). We note that going beyond a distance of a few megaparsecs reduces the EKL-driven area to a negligible part of the parameter space, and is omitted here to avoid clutter. The sharp cutoff to the right of the contours on the left panel comes from taking into account the Hill stability criterion.

eccentricity, Δe, induces a change in the waveform that has an S/N of 5 or greater. We will henceforth refer to the change in S/N caused by the change in eccentricity as $\Delta S/N(\Delta e)$. Note that this is a distinct quantity from the S/N of the system itself.

We run simulations of BHBs orbiting an SMBH, with a and e sampled from the parameter space shown in Figure 2. In our simulations we include the secular equations up to the octupole level of approximation (e.g., Naoz et al. 2013a), general relativity precession of the inner and outer orbits (e.g., Naoz et al. 2013b), and GW emission (Peters 1964). We consider an SMBH with a mass of 4×10^6 $(1 \times 10^7)\,M_\odot$ for the $D_l = 8$ kpc ($D_l = 1$ Mpc) case, and nominal outer orbit parameters $a_{\rm out} = 250$ au, $e_{\rm out} = 0.9$, and $\omega_{\rm out} = 0°$, where $\omega_{\rm out}$ is the argument of pericenter of the outer orbit. For the most comprehensive estimate of the region where Δe is large enough to result in a significant $\Delta S/N(\Delta e)$, we choose the mutual inclination i to be 90°, which maximizes the amplitude of eccentricity oscillations in a majority of cases. All that remains is to choose ω, the argument of pericenter of the inner orbit, which sets the phase of the oscillation and partially determines whether the change in eccentricity between consecutive $\Delta T_{\rm obs}$ is detectable. We run our simulations for three different values of ω: 0°, 45°, and 135° (e.g., Li et al. 2014). Lastly, we have restricted a in our simulations to be less than $\min[a_h, a_R]$, where $a_h = 0.1\, a_{\rm out}(1 - e_{\rm out}^2)/e_{\rm out}$, and $a_R = a_{\rm out}((m_1 + m_2)/3/m_\bullet)^{1/3}(1 - e_{\rm out})/(1 + e)$. The first is the condition to be a hierarchical triple, so that our secular equations of motion are applicable (e.g., Naoz 2016), and the second is the condition that the BHB does not cross the Roche limit of the SMBH (e.g., Naoz & Silk 2014). In all cases shown in Figure 2 we find that $a_R < a_h$. This condition causes the sharp cutoff in the right side of the contours seen in the left panel of Figure 2. Systems near this line may develop Hill instabilities as the inner BHB's eccentricity is excited, and be shorter lived than assumed here.

We then search through these simulations to find the value of $\Delta T_{\rm obs}$ that will maximize $\Delta S/N(\Delta e)$. We restrict $\Delta T_{\rm obs}$ to be greater than the value of $\Delta T_{\rm obs}$ that will give an S/N of 5, and to be smaller than 5 yr. We also maximize $\Delta S/N(\Delta e)$ with respect to ω, although we note that, in this proof-of-concept calculation, we have only sampled three fixed values of ω. Thus, we expect that the estimate given here is an underestimate of the parameter space where eccentricity oscillations are detectable. $\Delta S/N(\Delta e)$ is calculated by time-averaging the eccentricity evolution $e(t)$ over each $\Delta T_{\rm obs}$ interval, and using these averaged eccentricities to calculate the change in S/N between the two intervals using Equation (6).[8] In Figure 2 we show contours of where $\Delta S/N(\Delta e)$ is greater than 5 and 10. We distinguish between the cases where $\Delta S/N(\Delta e)$ results from an increase in eccentricity, and where $\Delta S/N(\Delta e)$ results from a decrease in eccentricity. Whereas the former can only be caused by EKL in our simulations, the latter can be caused by either EKL or GW emission. However, the two different types of eccentricity decreases occupy very distinct parts of the parameter space, as shown in Figure 2. We can see that EKL-driven eccentricity oscillations are detectable for a large fraction of the BHB parameter space, out to a few megaparsecs.

[8] Note that for simplicity we have assumed a constant a over consecutive $\Delta T_{\rm obs}$ intervals. This approximation holds well for most of the EKL-driven systems. However, for systems for which GW emission is significant, a is shrinking over $\Delta T_{\rm obs}$ (for example, far left systems in Figure 2).

5. Discussion

We present here a novel approach to distinguish eccentric stellar-mass BHBs that undergo eccentricity oscillations induced by an SMBH from other sources of GWs. It has been suggested that stellar binaries exist in high abundance in the vicinity of our galactic center, and thus also in other galactic nuclei (Ott et al. 1999; Martins et al. 2006; Pfuhl et al. 2014; Stephan et al. 2016; Hailey et al. 2018; Naoz et al. 2018; Stephan et al. 2019). In particular, Stephan et al. (2019) showed that the formation rate of compact object binaries (including EKL) is about $10^{-6}\,\mathrm{yr}^{-1}$ at the center of a Milky Way–like galaxy. Assuming a galaxy density of Milky Way–like galaxies is $0.02\,\mathrm{Mpc}^{-3}$ (Conselice et al. 2005), we find that inside the Local Group sphere ($\sim$3 Mpc, where we expect eccentricity oscillations to be detectable[9]), the rate of formation of compact object binaries is $\sim 2 \times 10^{-6}\,\mathrm{yr}^{-1}$. EKL contributes to the merger, and therefore the depletion, of BH binaries after about 10^8 yr (e.g., Hoang et al. 2018). Thus, if we assume that all binaries in galactic nuclei are depleted due to EKL, we estimate that about 200 binaries may be in the relevant parameter space detectable by LISA. On the other hand, if we assume that no binaries are depleted due to EKL, we have that over the lifetime of the Local Group ($\sim$10 Gyr), there are potentially $\sim$20,000 binaries that can have their eccentricity evolution detected in LISA. The true number is likely between these two limits.

In this proof-of-concept calculation, we have shown that eccentricity changes in a stellar-mass BHB induced by gravitational perturbations from a nearby SMBH is detectable by LISA (e.g., Figures 1 and 2). This could be used as a method of distinguishing these GW sources from sources in other astrophysical contexts. Constraining the binary's eccentricity and semimajor axis with LISA's future waveform templates could disentangle the evolutionary path of the system. Notably, detecting a binary in the EKL-driven regime can infer the existence of a nearby SMBH (or another tertiary). Furthermore, some of the physical parameters of the system, such as tertiary mass, eccentricity, and semimajor axis can be constrained.

It is not unlikely that the LISA mission lifetime will be extended beyond 4 yr. A 10 yr lifetime can potentially broaden the region in parameter space where eccentricity oscillations are detectable, as well as the distance to which they are detectable. However, we note that in the $D_l = 8$ kpc case, these eccentricity oscillations can be detected on a timescale of months (see the upper two panels of Figure 1). We found that the parameter space in which EKL-driven oscillations can be detected extends to a distance of a few megaparsecs.

We note that for this proof-of-concept calculation we adopted the secular approximation, however, some of the systems in Figures 1 and 2 deviate from pure secular dynamics. These systems may exhibit rapid (orbital timescales) eccentricity oscillations (e.g., Ivanov et al. 2005; Antognini et al. 2014; Antonini et al. 2014), which are at very low amplitude compared to the envelope eccentricity oscillations and may average out. We leave it to a future study to investigate whether these non-secular oscillations are significant. Furthermore, the deviation of the secular approximation may ultimately result in higher eccentricity spikes than the one calculated using the secular approximation (e.g., Katz et al. 2011; Bode & Wegg 2013), which will only strengthen the overall effect, but potentially complicate the analysis. We estimate the region of parameter space where non-secular effects might become important as where the EKL oscillation timescale is within a factor of a few larger than the outer orbital period (for a definition of the EKL timescale, see Naoz 2016). For an SMBH with a mass of $4 \times 10^6\,M_\odot$ and the nominal orbital parameters assumed in Figure 2, we find that the EKL oscillation timescale will be within a factor of 2 (5) of the outer orbital period for $a_{\mathrm{out}} \gtrsim 0.16\,(0.12)$ au. As can be seen in Figure 2, these non-secular effects, if at all detectable, will be most likely detected at small D_l like 8 kpc. Finally, we note that some of these systems may be shorter lived than assumed here since as e increases the binary may cross the SMBH Hill radius (as noted in other systems; e.g., Li et al. 2015).

The methodology presented here is straightforward to extend to stellar-mass BHBs around any tertiary, BH–SMBH binary with an SMBH companion, as well as triples containing any compact objects such as ones containing white dwarfs and neutron stars. The EKL mechanism is pervasive for a large set of astrophysical scenarios (e.g., Ford et al. 2000; Naoz 2016) and for a wide range of triple masses. Thus, the detection of EKL in different triple systems with LISA may allow us to distinguish between different triple orbital configurations, in particular, the tertiary's mass, outer orbit separation, eccentricity, and inclination. Localization within a galaxy will further allow disentanglement between the orbital parameters. Additionally, the approach shown here can help disentangle between binaries in triples and binaries of non-triple origin, since the latter will not exhibit oscillations in the characteristic strain-frequency parameter space. Thus, the proposed methodology here can serve as a potentially powerful method to disentangle different GW sources.

Furthermore, in this proof-of-concept Letter we have only focused on one effect of EKL—the oscillation in eccentricity—when there are in fact other EKL-induced effects like oscillation in inclination and precession of pericenter that can leave detectable imprints on the GW waveform. Thus, the detectability of EKL with GW may be possible for a wider range of systems than predicted by this work.

B.M.H. and S.N. acknowledge the partial support of NASA grant No. 80NSSC19K0321. S.N. also thanks Howard and Astrid Preston for their generous support. This project has received funding from the European Research Council (ERC) under the European Union's Horizon 2020 research and innovation program under grant agreement No. 638435 (GalNUC) and by the Hungarian National Research, Development, and Innovation Office grant NKFIH KH-125675 (to B.K.).

ORCID iDs

Bao-Minh Hoang https://orcid.org/0000-0003-0992-0033
Smadar Naoz https://orcid.org/0000-0002-9802-9279
Bence Kocsis https://orcid.org/0000-0002-4865-7517
Will M. Farr https://orcid.org/0000-0003-1540-8562
Jessica McIver https://orcid.org/0000-0003-0316-1355

References

Abbott, B. P., Abbott, R., Abbott, T. D., et al. 2016a, PhRvL, 116, 241103
Abbott, B. P., Abbott, R., Abbott, T. D., et al. 2016b, PhRvL, 116, 061102
Abbott, B. P., Abbott, R., Abbott, T. D., et al. 2017a, PhRvL, 118, 221101
Abbott, B. P., Abbott, R., Abbott, T. D., et al. 2017b, ApJL, 851, L35

[9] Note that eccentric binaries themselves can be detected in LISA to much larger distances (e.g., Fang et al. 2019).

Abbott, B. P., Abbott, R., Abbott, T. D., et al. 2017c, PhRvL, 119, 141101
Abbott, B. P., Abbott, R., Abbott, T. D., et al. 2017d, PhRvL, 119, 161101
Antognini, J. M., Shappee, B. J., Thompson, T. A., & Amaro-Seoane, P. 2014, MNRAS, 439, 1079
Antognini, J. M. O. 2015, MNRAS, 452, 3610
Antonini, F., Murray, N., & Mikkola, S. 2014, ApJ, 781, 45
Antonini, F., & Perets, H. B. 2012, ApJ, 757, 27
Antonini, F., & Rasio, F. A. 2016, ApJ, 831, 187
Arca-Sedda, M., & Capuzzo-Dolcetta, R. 2019, MNRAS, 483, 152
Arca-Sedda, M., & Gualandris, A. 2018, MNRAS, 477, 4423
Askar, A., Szkudlarek, M., Gondek-Rosińska, D., Giersz, M., & Bulik, T. 2017, MNRAS, 464, L36
Belczynski, K., Holz, D. E., Bulik, T., & O'Shaughnessy, R. 2016, Natur, 534, 512
Bode, J., & Wegg, C. 2013, arXiv:1310.5745
Breivik, K., Rodriguez, C. L., Larson, S. L., Kalogera, V., & Rasio, F. A. 2016, ApJL, 830, L18
Chen, X., & Amaro-Seoane, P. 2017, ApJL, 842, L2
Cholis, I., Kovetz, E. D., Ali-Haïmoud, Y., et al. 2016, PhRvD, 94, 084013
Conselice, C. J., Blackburne, J. A., & Papovich, C. 2005, ApJ, 620, 564
Cutler, C., & Flanagan, É. E. 1994, PhRvD, 49, 2658
Danzmann, K., et al. LISA Mission L3 Proposal 2017, https://www.elisascience.org/files/publications/LISA_L3_20170120.pdf
de Mink, S. E., & Mandel, I. 2016, MNRAS, 460, 3545
D'Orazio, D. J., & Samsing, J. 2018, MNRAS, 481, 4775
Fang, X., Thompson, T. A., & Hirata, C. M. 2019, arXiv:1901.05092
Ford, E. B., Kozinsky, B., & Rasio, F. A. 2000, ApJ, 535, 385
Fragione, G., & Kocsis, B. 2018, PhRvL, 121, 161103
Flanagan, É. É., & Hughes, S. A. 1998, PhRvD, 57, 4566
Gondán, L., Kocsis, B., Raffai, P., & Frei, Z. 2018, ApJ, 860, 5
Hailey, C. J., Mori, K., Bauer, F. E., et al. 2018, Natur, 556, 70
Hamers, A. S., Bar-Or, B., Petrovich, C., & Antonini, F. 2018, ApJ, 865, 2
Hoang, B.-M., Naoz, S., Kocsis, B., Rasio, F. A., & Dosopoulou, F. 2018, ApJ, 856, 140
Ivanov, P. B., Polnarev, A. G., & Saha, P. 2005, MNRAS, 358, 1361
Katz, B., Dong, S., & Malhotra, R. 2011, PhRvL, 107, 181101
Kocsis, B., Gáspár, M. E., & Márka, S. 2006, ApJ, 648, 411
Kocsis, B., & Levin, J. 2012, PhRvD, 85, 123005
Kocsis, B., Ray, A., & Portegies Zwart, S. 2012, ApJ, 752, 67
Kozai, Y. 1962, AJ, 67, 591
Kremer, K., Rodriguez, C. L., Amaro-Seoane, P., et al. 2019, PhRvD, 99, 063003
Li, G., Naoz, S., Holman, M., & Loeb, A. 2014, ApJ, 791, 86
Li, G., Naoz, S., Kocsis, B., & Loeb, A. 2015, MNRAS, 451, 1341
Lidov, M. L. 1962, P&SS, 9, 719
Lower, M. E., Thrane, E., Lasky, P. D., & Smith, R. 2018, PhRvD, 98, 083028
Mandel, I., & de Mink, S. E. 2016, MNRAS, 458, 2634
Marchant, P., Langer, N., Podsiadlowski, P., Tauris, T. M., & Moriya, T. J. 2016, A&A, 588, A50
Martins, F., Trippe, S., Paumard, T., et al. 2006, ApJL, 649, L103
Naoz, S. 2016, ARA&A, 54, 441
Naoz, S., Farr, W. M., Lithwick, Y., Rasio, F. A., & Teyssandier, J. 2013a, MNRAS, 431, 2155
Naoz, S., Ghez, A. M., Hees, A., et al. 2018, ApJL, 853, L24
Naoz, S., Kocsis, B., Loeb, A., & Yunes, N. 2013b, ApJ, 773, 187
Naoz, S., & Silk, J. 2014, ApJ, 795, 102
Nishizawa, A., Berti, E., Klein, A., & Sesana, A. 2016, PhRvD, 94, 064020
Nishizawa, A., Sesana, A., Berti, E., & Klein, A. 2017, MNRAS, 465, 4375
O'Leary, R. M., Kocsis, B., & Loeb, A. 2009, MNRAS, 395, 2127
O'Leary, R. M., Meiron, Y., & Kocsis, B. 2016, ApJL, 824, L12
O'Leary, R. M., Rasio, F. A., Fregeau, J. M., Ivanova, N., & O'Shaughnessy, R. 2006, ApJ, 637, 937
Ott, T., Eckart, A., & Genzel, R. 1999, ApJ, 523, 248
Peters, P. C. 1964, PhRv, 136, 1224
Peters, P. C., & Mathews, J. 1963, PhRv, 131, 435
Pfuhl, O., Alexander, T., Gillessen, S., et al. 2014, ApJ, 782, 101
Portegies Zwart, S. F., & McMillan, S. L. W. 2000, ApJL, 528, L17
Randall, L., & Xianyu, Z.-Z. 2018, ApJ, 864, 134
Randall, L., & Xianyu, Z.-Z. 2019, arXiv:1902.08604
Robson, T., Cornish, N., & Liu, C. 2018, arXiv:1803.01944
Rodriguez, C. L., Amaro-Seoane, P., Chatterjee, S., & Rasio, F. A. 2018, PhRvL, 120, 151101
Rodriguez, C. L., Chatterjee, S., & Rasio, F. A. 2016, PhRvD, 93, 084029
Samsing, J. 2018, PhRvD, 97, 103014
Samsing, J., & D'Orazio, D. J. 2018, MNRAS, 481, 5445
Stephan, A. P., Naoz, S., Ghez, A. M., et al. 2016, MNRAS, 460, 3494
Stephan, A. P., Naoz, S., Ghez, A. M., et al. 2019, arXiv:1903.00010
The LIGO Scientific CollaborationThe Virgo Collaboration 2018, arXiv:1811.12940
VanLandingham, J. H., Miller, M. C., Hamilton, D. P., & Richardson, D. C. 2016, ApJ, 828, 77
Wen, L. 2003, ApJ, 598, 419
Zevin, M., Samsing, J., Rodriguez, C., Haster, C.-J., & Ramirez-Ruiz, E. 2019, ApJ, 871, 91

THE ASTROPHYSICAL JOURNAL, 901:125 (7pp), 2020 October 1 https://doi.org/10.3847/1538-4357/abafa3

Detecting Kozai–Lidov Imprints on the Gravitational Waves of Intermediate-mass Black Holes in Galactic Nuclei

Barnabás Deme[1], Bao-Minh Hoang[2,3], Smadar Naoz[2,3], and Bence Kocsis[4,1]
[1] Institute of Physics, Eötvös University, Pázmány P.s. 1/A, Budapest, 1117, Hungary; deme.barnabas@gmail.com
[2] Department of Physics and Astronomy, University of California, Los Angeles, CA 90095, USA
[3] Mani L. Bhaumik Institute for Theoretical Physics, Department of Physics and Astronomy, UCLA, Los Angeles, CA 90095, USA
[4] Rudolf Peierls Centre for Theoretical Physics, Clarendon Laboratory, Parks Road, Oxford OX1 3PU, UK
Received 2020 May 13; revised 2020 August 10; accepted 2020 August 11; published 2020 September 29

Abstract

A third object in the vicinity of a binary system causes variations in the eccentricity and the inclination of the binary through the Kozai–Lidov (KL) effect. We examine if such variations leave a detectable imprint on the gravitational waves of a binary consisting of intermediate-mass black holes and stellar-mass objects. As a proof of concept, we present an example where LISA may detect the KL-modulated gravitational wave signals of such sources from at least a distance of 1 Mpc if the perturbation is caused by a supermassive black hole tertiary. Although the quick pericenter precession induced by general relativity significantly reduces the appropriate parameter space for this effect by quenching the KL oscillations, we still find reasonable parameters where the KL effect may be detected with high signal-to-noise ratios.

Unified Astronomy Thesaurus concepts: Intermediate-mass black holes (816); Gravitational wave sources (677)

1. Introduction

According to the current paradigm, nearly all galaxies, including our own, host a supermassive black hole (SMBH) at their centers (Ghez et al. 2008; Genzel et al. 2010; Kormendy & Ho 2013). Being the engine of galactic nuclear activity, they have a large influence both on their immediate environment (e.g., Inoue et al. 2020) and on more extended scales, which leads to correlations between the SMBH and the host galaxy properties (King 2003). Observations such as periodic active galactic nucleus (AGN) variability show that some SMBHs are found in binaries (Kelley et al. 2019). They are the natural consequences of galaxy mergers predicted by the ΛCDM model (e.g., Di Matteo et al. 2005; Hopkins et al. 2006; Robertson et al. 2006). The SMBH at the center of the Milky Way may also have a massive binary companion (see Gualandris & Merritt 2009; Gualandris et al. 2010; Naoz et al. 2020, for observational constraints). SMBH binaries play a key role in galaxy evolution (e.g., Begelman et al. 1980; Blecha & Loeb 2008). They explain the mass deficit of stars observed in the centers of galaxies (Merritt 2006; Gualandris & Merritt 2012), they lead to the ejection of hyper velocity stars (e.g., Yu & Tremaine 2003; Fragione & Gualandris 2019; Luna et al. 2019; Rasskazov et al. 2019), affect tidal disruption and GW events (e.g., Ivanov et al. 2005; Chen et al. 2009, 2011; Sesana et al. 2011; Wegg & Nate Bode 2011; Chen & Liu 2013; Meiron & Laor 2013; Li et al. 2015; Fragione et al. 2020), and lead to an electromagnetic signature from dark matter annihilation (Naoz & Silk 2014; Naoz et al. 2019). The inspiral of such SMBH binaries will be targets for the future space-borne gravitational wave (GW) observatory LISA[5] (e.g., Amaro-Seoane et al. 2017).

[5] https://lisa.nasa.gov/

The mass spectrum of SMBHs arguably extends down to the regime of intermediate-mass black holes (IMBHs; see Greene et al. 2019 and Mezcua 2017 for recent reviews). An SMBH-IMBH binary may reside in the nucleus of some galaxies. The IMBHs may form in SMBH accretion disks (Goodman & Tan 2004; McKernan et al. 2012) or they may be transported to the galactic center region by infalling globular clusters that also help to form the nuclear star clusters around SMBHs (Portegies Zwart et al. 2006; Mastrobuono-Battisti et al. 2014). Gravitational wave (GW) astronomy, which has recently opened a new window on the universe (Abbott et al. 2016), may directly test the existence of IMBHs in galactic nuclei.

There are multiple dynamical processes in the nuclear regions of galaxies, which may affect the binaries' GWs. The perturbations associated with the SMBH in nuclear star clusters may be significant. The SMBH perturber leads to the acceleration of a binary's center of mass, which may be detected by LISA (Yunes et al. 2011). Furthermore, variations caused by relativistic beaming, Doppler, and gravitational redshift associated with the SMBH companion may also lead to potentially detectable signatures (Meiron et al. 2017). In this paper, we examine if the Kozai–Lidov (KL) effect of the SMBH leads to detectable variations on binaries in nuclear star clusters.

The KL mechanism has been long recognized to be one of the important dynamical processes in galactic nuclei (see Naoz 2016 for a review). It describes the long-term dynamics of a hierarchical triple system in separation, i.e., when two of the bodies constitute a tight inner binary, which is orbited by a more distant tertiary (outer binary). This third object perturbs the inner binary in such a way that it exhibits eccentricity and inclination oscillations with nearly constant semimajor axis (Kozai 1962; Lidov 1962). It can be shown that the octupole-order perturbation by the third body can pump up the eccentricity to very high values close to unity (Lithwick & Naoz 2011) which leads to gravitational wave bursts during close periapsis encounters (O'Leary et al. 2009; Kocsis & Levin 2012). The KL torque from an SMBH may result in the

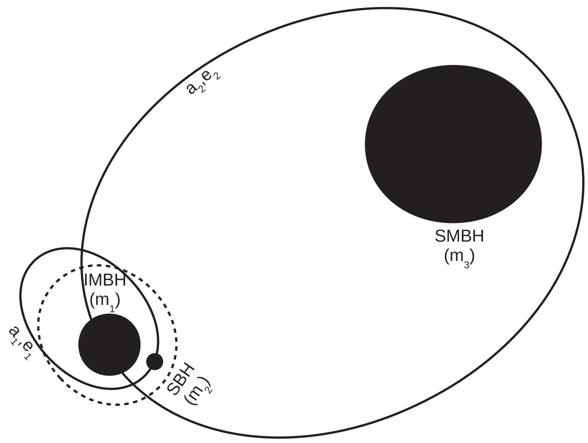

Figure 1. The configuration under consideration. The dotted ellipse shows KL-modulated inner orbit.

merger of compact object binaries (e.g., Antonini et al. 2014; Hoang et al. 2018).[6] The eccentricity oscillations from KL effects are directly detectable in the inspiral phase long before the merger of the inner binary, which causes a periodic shift in the GW strain signal (Hoang et al. 2019; Randall & Xianyu 2019; Gupta et al. 2020).

In this paper we examine how the mass and initial orbital parameters of the inner binary affect LISA's ability to identify the KL effect of the SMBH on binaries in galactic nuclei (see also Emami & Loeb 2020). We show that if the inner binary consists of an IMBH and a stellar-mass black hole (see Figure 1), LISA may directly detect the KL oscillations from a distance of 1 Mpc.

This paper is structured as follows. In Section 2 we introduce the timescales, which have a key role in the dynamics we investigate. In Section 3 we calculate the signal-to-noise ratio (S/N) and in Section 4 we discuss our results.

2. Timescales and Constraints

The relevant timescales for our study are the KL time ($T_{\rm KL}$), the general relativistic (GR) apsidal precession time ($T_{\rm GR}$), and the GW inspiral time ($T_{\rm GW}$) (Peters 1964; Naoz 2016):

$$T_{\rm KL} = \frac{a_2^3(1-e_2^2)^{3/2}(m_1+m_2)^{1/2}}{G^{1/2}a_1^{3/2}m_3}, \tag{1}$$

$$T_{\rm GR,1} = \frac{a_1^{5/2}c^2(1-e_1^2)}{G^{3/2}(m_1+m_2)^{3/2}}, \tag{2}$$

$$T_{\rm GW,1} = \frac{5c^5a_1^4}{64G^3m_1m_2(m_1+m_2)F(e_1)}, \tag{3}$$

$$T_{\rm GW,2} = \frac{5c^5a_2^4}{64G^3(m_1+m_2)m_3(m_1+m_2+m_3)F(e_2)}, \tag{4}$$

where the 1 and 2 subscripts refer to the inner and outer binaries, respectively, and

$$F(e) = \frac{1+\frac{73}{24}e^2+\frac{37}{96}e^4}{(1-e^2)^{7/2}}. \tag{5}$$

Long-lived triples must satisfy the Hill stability criterion, i.e.,

$$\frac{a_1}{a_2} \lesssim \frac{1-e_2}{1+e_1}\left(\frac{m_1+m_2}{3m_3}\right)^{1/3}, \tag{6}$$

and we restrict attention to sufficiently hierarchical configurations so that we can neglect the terms beyond octupole in the expansion of the Hamiltonian

$$\frac{a_1}{a_2} \lesssim 0.1\frac{1-e_2^2}{e_2}. \tag{7}$$

Equations (6) and (7) show that Equation (6) is always more strict if $(m_1+m_2)/m_3 \lesssim 0.024$. In particular, Hill-stable inner binaries with 10 and $10^5\,M_\odot$ around a $10^8\,M_\odot$ SMBH have $(m_1+m_2)/m_3 \sim 0.001$ and automatically satisfy the hierarchy criterion.

It is useful to express Equations (1)–(4) with distances normalized by the corresponding gravitational radii:

$$R_{\rm g1} = \frac{G(m_1+m_2)}{c^2}, \quad R_{\rm g3} = \frac{Gm_3}{c^2}, \tag{8}$$

and with the mass ratios $\mu_1 = m_1/m_3$ and $\mu_2 = m_2/m_3$ as

$$\frac{T_{\rm KL}}{R_{\rm g3}/c} = \frac{(1-e_2^2)^{3/2}}{(\mu_1+\mu_2)}\frac{(a_2/R_{\rm g3})^3}{(a_1/R_{\rm g1})^{3/2}}, \tag{9}$$

$$\frac{T_{\rm GR,1}}{R_{\rm g3}/c} = (1-e_1^2)(\mu_1+\mu_2)(a_1/R_{\rm g1})^{5/2}, \qquad (1\ )$$

$$\frac{T_{\rm GW,1}}{R_{\rm g3}/c} = \frac{5}{64F(e_1)}\frac{(\mu_1+\mu_2)^3}{\mu_1\mu_2}\left(\frac{a_1}{R_{\rm g1}}\right)^4, \tag{11}$$

$$\frac{T_{\rm GW,2}}{R_{\rm g3}/c} = \frac{5}{64F(e_2)}\frac{(a_2/R_{\rm g3})^4}{(\mu_1+\mu_2)(1+\mu_1+\mu_2)} \tag{12}$$

and the Hill stability criterion reads

$$\frac{a_1/R_{\rm g1}}{a_2/R_{\rm g3}} < 3^{-1/3}\frac{1-e_2}{1+e_1}(\mu_1+\mu_2)^{-2/3}. \tag{13}$$

Figure 2 shows the parameter space for different separations and mass ratios where these timescales are in the suitable range for the KL effect to play a role during LISA observations. We show cases where $T_{\rm KL} < 10$ yr, $T_{\rm GR,1} > 10$ yr, $T_{\rm GW,1} > 10^8$ yr, and $T_{\rm GW,2} > 10^8$ yr for $m_3 = 10^8\,M_\odot$. The values of the timescales are chosen arbitrarily, but in the case of GR and KL times (10 yr) we took into account the operational time of LISA. We also note that once $T_{\rm GR,1} < T_{\rm KL}$, the KL mechanism is quenched, i.e., the amplitude of the eccentricity oscillations is significantly damped; however, we will show that they are still detectable. The right panels show higher μ_1 (i.e., higher m_1), while the bottom one shows higher μ_2. The initial outer eccentricity is set to $e_2 = 10^{-6}$, which remains approximately constant during the evolution since $\mu_2 \ll 1$. This condition also implies that the evolution is well approximated by the quadrupole term of the Hamiltonian. Thus Equation (1) is quite accurate and the outer argument of pericenter does not

[6] The mergers in such a scenario can be further facilitated by other dynamical effects, including mass-segregation (O'Leary et al. 2009), vector resonant relaxation (Hamers et al. 2018), "gas-capture" binary formation in AGN disks (Tagawa et al. 2020) or resonant(-like) general relativistic effects (Naoz et al. 2013; Fang & Huang 2020; Liu & Lai 2020).

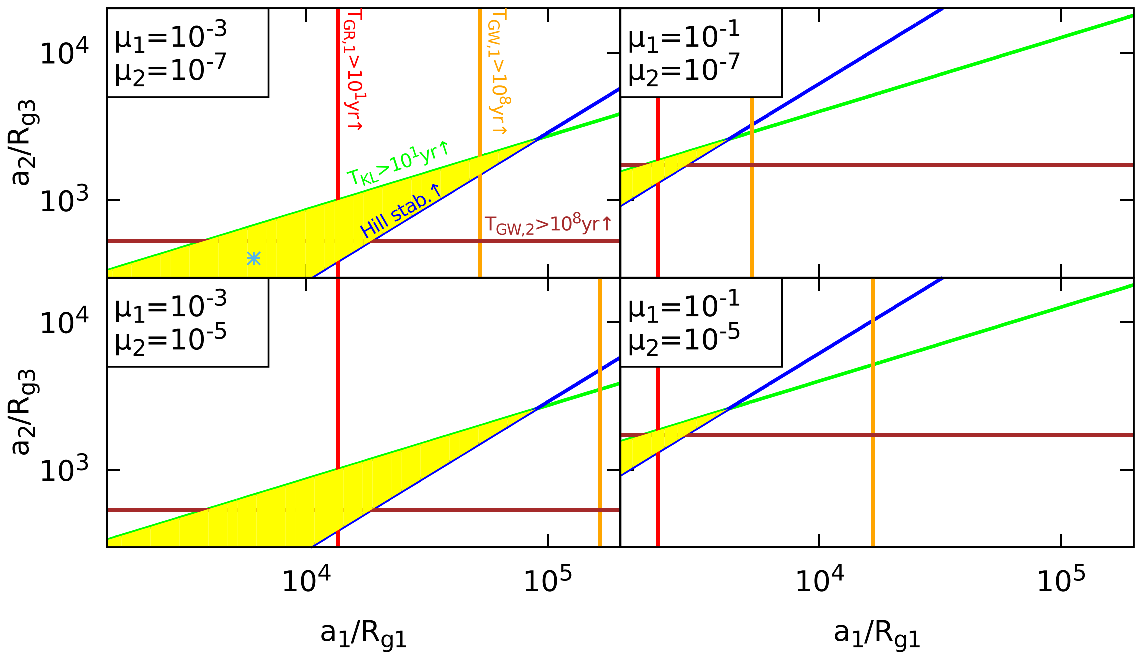

Figure 2. Timescales and Hill stability criterion for repressive systems. We consider three black holes in a hierarchical configuration, where $m_3 = 10^8\,M_\odot$ and the masses of the other two are given with ratios $\mu_1 = m_1/m_3$ and $\mu_2 = m_2/m_3$ in the legends. The gravitational radius of the the tertiary, the length unit, is $R_{g3} = 0.987$ au, while the eccentricities are set to $e_1 = 0.985$ and $e_2 = 10^{-6}$ initially. The yellow zone indicates the ideal region for detecting SMBH-induced KL oscillations, where the KL timescale is on the order of LISA's lifetime and the system is Hill-stable. The blue asterisk indicates the initial condition of a representative simulation shown in Figure 3 ($a_1/R_{g1} = 6077.6$, $a_2/R_{g3} = 405.22$).

need to be accounted for as the quadrupole Hamiltonian is independent of it (the so-called "happy coincidence" Lidov & Ziglin 1976). The ideal zone in the parameter space, where the triple is Hill stable and KL oscillations may occur in LISA observations, is the highlighted yellow area between the green and the blue curves. This region is larger in the case of the left panels. More specifically, in what follows we focus on the top left, where $m_1 = 10^5\,M_\odot$ and $m_2 = 10\,M_\odot$ and where the GR and GW timescales are slightly longer than in the bottom left. Further decreasing μ_2 would also decrease the GR timescale, allowing KL to pump the eccentricity higher, but $\mu_2 < 10^{-8}$ with $m_3 = 10^8\,M_\odot$ would result in unphysically low compact object masses. Most of the yellow zone is of little use, though, because high a_1 gives weak GW signal for sources outside of the Milky Way. For this reason, in what follows we restrict the inner semimajor axis to the range $a_1 \in [1; 10]$ au, i.e., a_1/R_{g1} between $\sim 10^3$ and 10^4.

Since the triple system under investigation takes place in a nuclear star cluster, we calculate the relevant timescales of its interactions with the surrounding objects. For the sake of simplicity, we consider uniform masses for the cluster members, $m_* = 1\,M_\odot$. Assuming that the cluster is virialized, the kinetic energy of the cluster stars in the vicinity of the outer binary is $m_*\sigma^2 = Gm_3m_*/a_2$. Comparing it with the total energy of the inner binary, $Gm_1m_2/(2a_1)$, we find that the inner binary is hard if

$$a_1 \leqslant a_{1,\mathrm{hard}} = \frac{m_1 m_2}{m_3 m_*} a_2 \tag{14}$$

or equivalently if

$$\frac{a_1/R_{g1}}{a_2/R_{g3}} \leqslant \frac{m_1 m_2}{(m_1 + m_2)m_*} \approx \frac{m_2}{m_*}, \tag{15}$$

where the last approximate equality holds in the limit $m_2 \ll m_1$. In what follows we will highlight the representative case of $m_1 = 10^5\,M_\odot$, $m_2 = 10\,M_\odot$, $m_3 = 10^8\,M_\odot$, and $a_2 =$ 400 au (see the caption of Figure 2), for which $a_{1,\mathrm{hard}} = 4$ au. According to Heggie's law (Heggie 1975), these binaries get even harder due to the flybys of the surrounding stars, while those that are soft ($a_1 > a_{1,\mathrm{hard}}$) get even softer until they finally evaporate. The characteristic timescales of these processes are (Binney & Tremaine 2008)

$$T_{\mathrm{hard}} = \frac{\sigma}{7.6Gnm_*a_1}\frac{m_2}{m_1} = \frac{1}{7.6\sqrt{G}\,n_0}\frac{m_3^{1/2}m_2}{m_*m_1a_1a_2^{1/2-\gamma}} \approx 1852\ \mathrm{yr}, \tag{16}$$

$$T_{\mathrm{ev}} = \frac{\sqrt{3}\,\sigma(m_1 + m_2)}{32\sqrt{\pi}\,Gnm_*^2a_1\ln\Lambda} = \frac{\sqrt{3}}{32\sqrt{\pi G}\,n_0\ln\Lambda}\frac{\sqrt{m_3}\,(m_1 + m_2)}{m_*^2a_1a_2^{1/2-\gamma}} \approx 2.3 \times 10^{10}\ \mathrm{yr}, \tag{17}$$

where the masses and a_2 are as previously and a_1 is set to 5 au, the mean of its interval in our investigations, for the Coulomb logarithm we assumed $\Lambda = m_3/m_*$ (Alexander 2017), and for the number density we assumed $n = n_0(a_2/400\ \mathrm{au})^{-\gamma}$, where

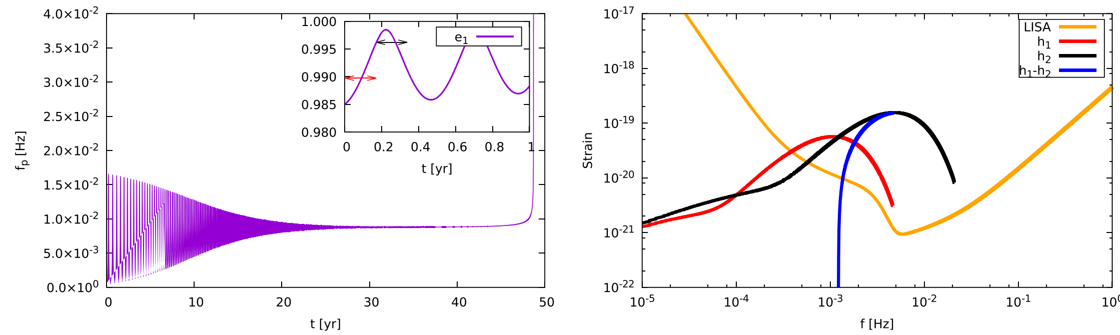

Figure 3. Left: pericenter frequency evolution of the IMBH-SBH inner binary initiated in the parameter space from the black asterisk in Figure 2. It oscillates in the LISA frequency band due to the KL torque from the SMBH tertiary, but later becomes damped by the quick pericenter precession induced by GR. The in-set figure shows the first two KL-peaks in the eccentricity. The horizontal black and red arrows show the interval of averaging (2 months). We use these mean values for calculating the strain (shown in black and red in the right panel). We note that the GW inspiral time is only $\sim$50 yr, even though Equation (3) predicts much longer values from the initial parameters ($T_{\mathrm{GW},1} \approx 1.4 \times 10^4$ yr), because the eccentricity is increased to very high values. Right: LISA sensitivity curve and the strain for the two 2 month intervals marked in the inset of the left panel. h_1 corresponds to $a_1 = 5.999887$ au, $e_1 = 0.989745$ and $\mathrm{S/N} = 5.81\,(D_{\mathrm{L}}/\mathrm{Mpc})^{-1}$, while h_2 to $a_1 = 5.968728$ au, $e_1 = 0.996220$, and $\mathrm{S/N} = 117\,(D_{\mathrm{L}}/\mathrm{Mpc})^{-1}$. The blue curve shows the difference of the strains in response to the changing orbital parameters in the inner binary, either due to the KL mechanism or GWs.

$\gamma = 7/4$ (Bahcall & Wolf 1976) and $n_0 = 10^9\ \mathrm{pc}^{-3}$ so the number density is $\approx 10^6\ \mathrm{pc}^{-3}$ at 0.1 pc (Neumayer et al. 2020). We note that the extrapolation of the Bahcall–Wolf formula to such small distances may be inaccurate, as the number density is reduced by the central SMBH. The distance where stars are not replenished efficiently is where the gravitational wave inspiral time into the SMBH is less than the two-body relaxation $a_2 \lesssim 10^3 R_{g3} \approx 10^3$ au (Gondán et al. 2018). Inside of this region the depletion of stars increases the hardening and the evaporation timescales.

Further, Deme et al. (2020) showed that a small population of IMBHs in the galactic nucleus perturbs the outer orbit of compact objects around the SMBH, which also ultimately decreases the number of binaries in the galactic center in $\approx 10^6$ yr.

Binary formation through triple interactions is even less probable. Its timescale is (Binney & Tremaine 2008)

$$T_{\mathrm{form}} = \frac{\sigma^9}{n^2 G^5 m_1^5} = \frac{1}{\sqrt{G} n_0^2} \frac{m_3^{9/2}}{m_1^5 a_2^{9/2-2\gamma}} \approx 2.43 \times 10^{12}\ \mathrm{yr}, \tag{18}$$

which is well beyond the age of the universe.[7]

We conclude that binary hardening, evaporation, binary disruption by IMBHs, and three-body encounters are all much longer than LISA's expected lifetime, so these effects are unlikely to take place during the observation, hence they do not directly influence our results.

Figure 3 demonstrates the time evolution of the system for a representative example shown with a star in Figure 2 at a distance of 1 Mpc. We simulate the system using the secular OSPE code. The left panel shows the pericenter frequency evolution of the inner binary. Its oscillatory behavior at the beginning is due to the KL effect, which is later quenched by GR precession. The inset of the left panel shows the first year of the inner eccentricity evolution. One way to detect the KL effect in practice is to average the GW strain over time in two-month-long intervals, indicated by horizontal arrows. We calculate the strain spectra for these averaged intervals, which are shown in the right panel of Figure 3. In order to detect the KL oscillations, both the GW spectral amplitude (black and red curves) and its variation (blue curve) are required to be above the LISA sensitivity curve (denoted by orange). Technically, by the difference of the strains we mean the strain of the difference of the GW signals obtained from two subsequent observational time segments.

3. Signal-to-noise Ratios

In order to estimate the detectability of the signal within an observation segment of time duration T_{obs}, we calculate the S/N following Hoang et al. (2019)

$$\mathrm{S/N}^2 = 4 \int \frac{|\tilde{h}|^2}{S_n} df, \tag{19}$$

where $\tilde{h}$ is the Fourier transform of the GW strain signal and $S_n \equiv S(f_n)$ is the LISA spectral noise amplitude. For short time segments that satisfy $T_{\mathrm{GW1}} \gg T_{\mathrm{obs}}$, and that the orbital time around the SMBH is sufficiently long, i.e., $T_{\mathrm{orb3}} = 2\pi [a_3^3/G(m_1 + m_2 + m_3)]^{1/2} \gg T_{\mathrm{obs}}$ we may substitute the the strain for a fixed semimajor axis a_1 (Peters 1964).

The left panel of Figure 4 shows the S/N for the *initial* parameters of the secular evolution (calculated with $T_{\mathrm{obs}} = 2$ months), i.e., the GW signal we would measure from the inner binary at the beginning. A red asterisk marks here the initial values used in the representative example shown in Figure 3. The relevant timescales for the *initial* configuration are indicated with lines. However, note that these timescales change significantly during the evolution.

In order to calculate how the S/N changes during the KL evolution, we run $\sim$4000 simulations, each for 20 yr and with $a_2 = 400$ au, $e_2 = 10^{-6}$. The right panel of Figure 4 indicates the maximum ΔS/N, i.e., the highest change in the S/N during the evolution between two subsequent observational segments (T_{obs}) for the system initiated from that particular point of the (a_1/R_{g1}, $1 - e_1$) parameter space. Here ΔS/N is maximized over the argument of the inner pericenter ω_1 in a way that it is varied in a grid from 0° to 360° keeping the rest of the initial

[7] We note that binary formation is much more efficient in an AGN disk through the gas-capture mechanism (Tagawa et al. 2020) or GW capture by close encounters.

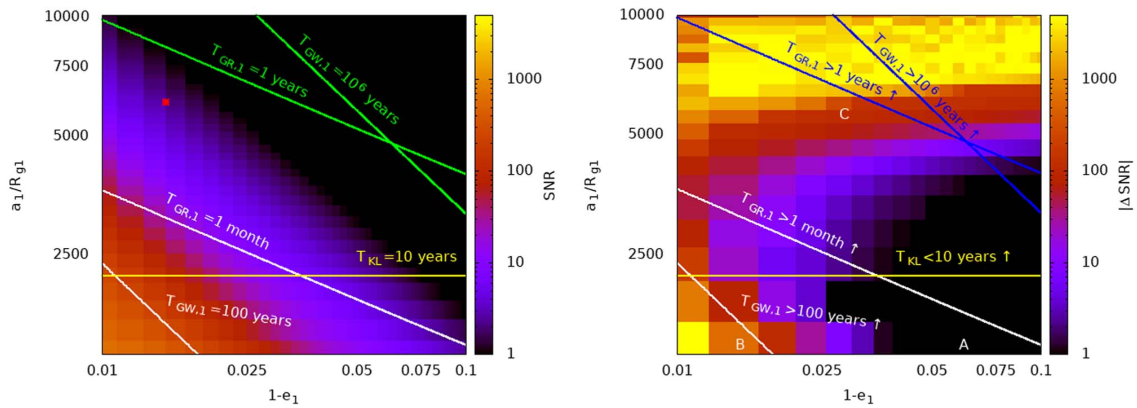

Figure 4. Left: S/N of the GW signal from the IMBH-SBH inner binary calculated from the *initial* orbital parameters e_1 and a_1/R_{g1} for an observation time $T_{obs} = 2$ months for sources at 1 Mpc. The red asterisk corresponds to the same initial position as the one marked in Figure 2. We emphasize that the orbital parameters significantly change in time due to the KL oscillations, GR precession and GW radiation. By the same manner, timescales indicated by the lines reduce significantly, too. Right: the highest change in S/N during the evolution between two subsequent averaging time segments, maximized over both ω_1 and T_{obs}. In order to demonstrate the underlying dynamics we show the evolution of the orbital elements from three different parts of the parameter space, denoted by A, B, and C, in Figure 5.

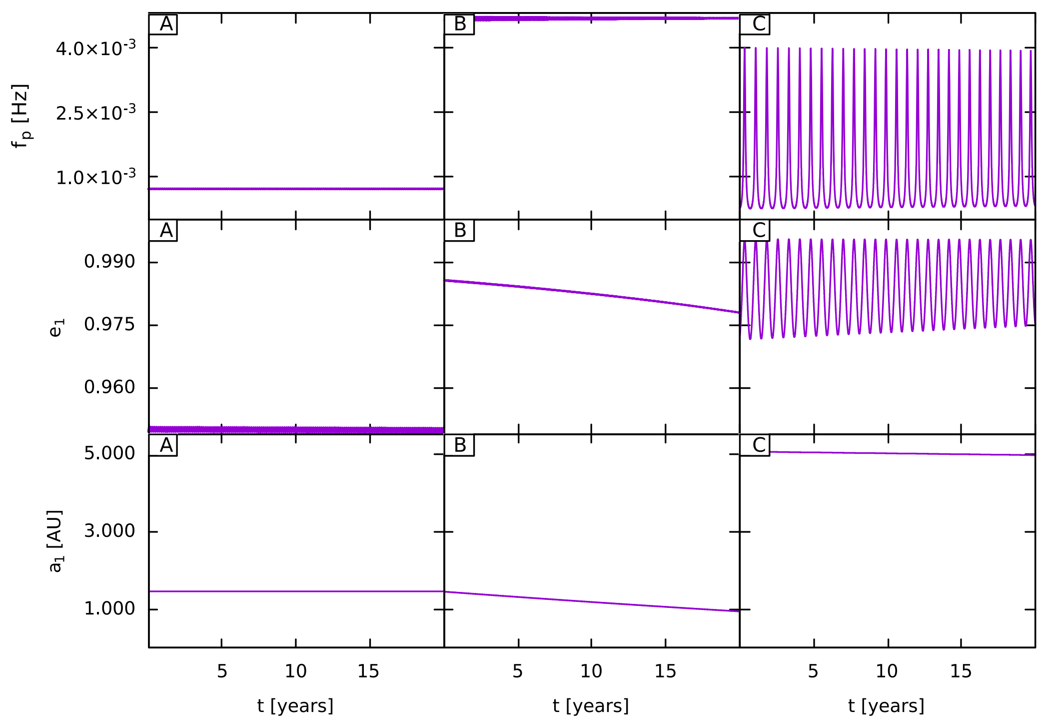

Figure 5. The orbital element evolution of the three systems sampled from the right panel of Figure 4. Evolutions A and B are both highly damped by GR. The high $\Delta S/N$ value at B is the result of the strong GW decay.

elements fixed, choosing the ω_1 that resulted in the highest $|\Delta S/N|$. We also optimize for the T_{obs} observational time: we calculate the $\Delta S/N$ for $T_{obs} \in \{10^{-1}, 10^0, 10^1\}$ yr and choose whichever gives the highest change in S/N during the evolution. We note that it makes the predictions of the right panel somewhat pessimistic: the $\Delta S/N$ values could be further increased if we chose T_{obs} that fits eccentricity oscillation timescale better.

The right panel of Figure 4 shows that the high $\Delta S/N$ values are found at large initial a_1 independently of e_1 and at small a_1 and $1 - e_1$. This is not unexpected because for the former the KL time is shortest at high a_1 while the GR precession and inspiral time are longer there (see Equation (1)); therefore, KL oscillations are less damped there. Interestingly, in this region the binary would not be detected without the KL oscillations, which push the binary to high eccentricities. For small a_1 and

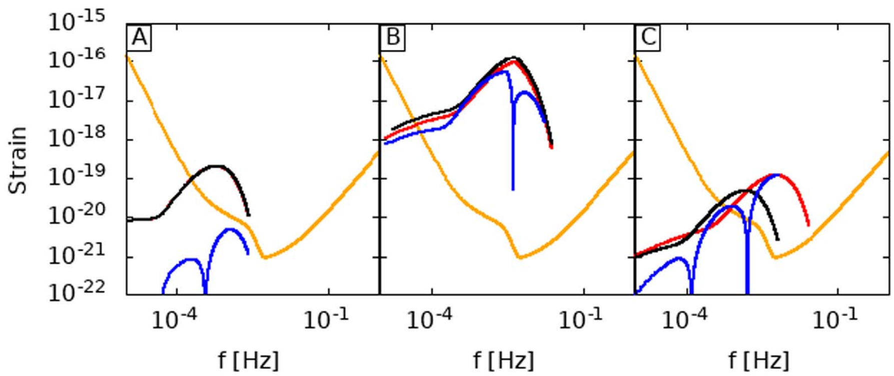

Figure 6. The GW spectra of the systems sampled from the right panel of Figure 4. The black and red curves correspond to the signals that give the highest $\Delta S/N$ during the evolution. The blue curve is the difference of them. In case A the black and red curves are so close to each other that they are not separable by eye.

high e_1, the orbital parameters change rapidly due to the GW inspiral independently of the KL effect, which explains the lower left peak of $\Delta S/N$ in Figure 4.

To better understand this behavior, we select three representative points (denoted by A, B, and C in Figure 4) and plot the time evolution of their orbital elements in Figure 5 and the GW spectral amplitude in Figure 6. The first row of panels shows the pericenter frequency calculated as

$$f_p = \frac{1}{2\pi}\sqrt{\frac{G(m_1+m_2)}{a_1^3}\frac{(1+e_1)}{(1-e_1)^3}}. \tag{20}$$

The figures show that Case C exhibits multiple prominent KL oscillation cycles, which leads to a high $\Delta S/N$. However, in Case B, KL oscillations are quenched by the rapid GR precession. We note that even in such a quenched case there are some small oscillations ($\Delta e \sim 10^{-4}$, $T_{\rm GR} \sim 10^{-2}$ yr, e.g., Naoz et al. 2013), but they do not produce significant $\Delta S/N$ because of the small change in the eccentricity. The high $\Delta S/N$ is obtained with $T_{\rm obs} = 10$ yr: the reason for this is that most of the variation of the orbital parameters is caused by the GW inspiral (not by the SMBH), so we need to have a $T_{\rm obs}$ that is comparable to the inspiral time, $T_{\rm GW,1} \approx 57$ yr. The high $\Delta S/N$ is thus mostly independent of the KL effect. In case A, the orbital parameters are almost constant as the system is neither inspiraling nor does it exhibit KL oscillations.

4. Discussion and Conclusion

We have shown that the dynamical imprint of SMBHs may be significantly detected with LISA from 1 Mpc for compact objects orbiting IMBHs in galactic nuclei. Figure 4 showed the initial orbital parameters where this identification is possible. We found that the imprint of KL oscillations is most prominent for IMBH sources orbited by a stellar-mass compact object that orbits around an SMBH. A binary of two stellar-mass compact objects also exhibits similar oscillations in the vicinity of an SMBH, but in this case either the GW strain amplitude is much smaller or the GR precession rate is higher, which decreases the KL oscillation amplitude. Further, KL oscillations are also less prominent in hierarchical SMBH triples since in this case the KL timescale is typically much longer than the observation time.

To demonstrate the detectability of KL oscillations in a robust way, we calculated the variations of the S/N during the observation in fixed $T_{\rm obs}$ duration segments of the total observation period, and marginalized over the value of $T_{\rm obs}$. This analysis showed that the variations due to the KL effect can be highly significant and detectable with LISA to at least 1 Mpc.

While we have highlighted cases where the full KL oscillations may be detected with LISA with very high significance, the true parameter space where the KL effect may be detected is certainly much larger. Since the number of GW cycles is of order $N_{\rm GW} \sim T_{\rm obs} f_{\rm orb} \sim T_{\rm obs} f_p (1-e_1)^{3/2}$ (Equation (20)), a very small variation of eccentricity of order

$$4 \times 10^{-4}\left(\frac{T_{\rm obs}}{4\ {\rm yr}}\right)^{-2/3}\left(\frac{f_p}{1\ {\rm mHz}}\right)^{-2/3} \tag{21}$$

may cause order unity change in the number of detected cycles during a 4 yr observation. Thus, the KL effect may be significant even if only a 10^{-3} fraction of a full KL cycle is observed. Furthermore, KL oscillations may push the binary to such high eccentricities that the binary merges during the observation. For merging binaries, the number of GW cycles is proportional to the inverse GW timescale, which for asymptotically high e_1 close to unity is proportional to $(1-e_1^2)^{-7/2}$ (Equation (3)), implying an even higher sensitivity to eccentricity. Thus, the KL effect of inspiraling GW sources may be highly significant even in cases where the observation time and/or the GW inspiral time is much shorter than the KL timescale.

While we leave the detailed GW data analysis exploration of KL imprints to a future study, these arguments suggest that the detection prospects of the KL effect may be possible even beyond the case of IMBH-stellar-mass compact object triples around SMBHs.

This project has received funding from the European Research Council (ERC) under the European Union's Horizon 2020 research and innovation program under grant agreement No. 638435 (GalNUC) and by the Hungarian National Research, Development, and Innovation Office grant NKFIH KH-125675. B.M.H. and S.N. acknowledge the partial support of NASA grant Nos. 80NSSC19K0321 and 80NSSC20K0505. S.N. also thanks Howard and Astrid Preston for their generous support.

ORCID iDs

Barnabás Deme https://orcid.org/0000-0003-4016-9778
Bao-Minh Hoang https://orcid.org/0000-0003-0992-0033
Smadar Naoz https://orcid.org/0000-0002-9802-9279
Bence Kocsis https://orcid.org/0000-0002-4865-7517

References

Abbott, B. P., Abbott, R., Abbott, T. D., et al. 2016, PhRvX, 6, 041015
Alexander, T. 2017, ARA&A, 55, 17
Amaro-Seoane, P., Audley, H., Babak, S., et al. 2017, arXiv:1702.00786
Antonini, F., Murray, N., & Mikkola, S. 2014, ApJ, 781, 45
Bahcall, J. N., & Wolf, R. A. 1976, ApJ, 209, 214
Begelman, M. C., Blandford, R. D., & Rees, M. J. 1980, Natur, 287, 307
Binney, J., & Tremaine, S. 2008, Galactic Dynamics: Second Edition (Princeton, NJ: Princeton Univ. Press)
Blecha, L., & Loeb, A. 2008, MNRAS, 390, 1311
Chen, X., & Liu, F. K. 2013, ApJ, 762, 95
Chen, X., Madau, P., Sesana, A., & Liu, F. K. 2009, ApJL, 697, L149
Chen, X., Sesana, A., Madau, P., & Liu, F. K. 2011, ApJ, 729, 13
Deme, B., Meiron, Y., & Kocsis, B. 2020, ApJ, 892, 130
Di Matteo, T., Springel, V., & Hernquist, L. 2005, Natur, 433, 604
Emami, R., & Loeb, A. 2020, MNRAS, 495, 536
Fang, Y., & Huang, Q.-G. 2020, arXiv:2004.09390
Fragione, G., & Gualandris, A. 2019, MNRAS, 489, 4543
Fragione, G., Loeb, A., Kremer, K., & Rasio, F. A. 2020, ApJ, 897, 46
Genzel, R., Eisenhauer, F., & Gillessen, S. 2010, RvMP, 82, 3121
Ghez, A. M., Salim, S., Weinberg, N. N., et al. 2008, ApJ, 689, 1044
Gondán, L., Kocsis, B., Raffai, P., & Frei, Z. 2018, ApJ, 860, 5
Goodman, J., & Tan, J. C. 2004, ApJ, 608, 108
Greene, J. E., Strader, J., & Ho, L. C. 2019, arXiv:1911.09678
Gualandris, A., Gillessen, S., & Merritt, D. 2010, MNRAS, 409, 1146
Gualandris, A., & Merritt, D. 2009, ApJ, 705, 361
Gualandris, A., & Merritt, D. 2012, ApJ, 744, 74
Gupta, P., Suzuki, H., Okawa, H., & Maeda, K.-I. 2020, PhRvD, 101, 104053
Hamers, A. S., Bar-Or, B., Petrovich, C., & Antonini, F. 2018, ApJ, 865, 2
Heggie, D. C. 1975, MNRAS, 173, 729
Hoang, B.-M., Naoz, S., Kocsis, B., Farr, W. M., & McIver, J. 2019, ApJL, 875, L31
Hoang, B.-M., Naoz, S., Kocsis, B., Rasio, F. A., & Dosopoulou, F. 2018, ApJ, 856, 140
Hopkins, P. F., Hernquist, L., Cox, T. J., et al. 2006, ApJS, 163, 1
Inoue, K. T., Matsushita, S., Nakanishi, K., & Minezaki, T. 2020, ApJL, 892, L18
Ivanov, P. B., Polnarev, A. G., & Saha, P. 2005, MNRAS, 358, 1361
Kelley, L. Z., Haiman, Z., Sesana, A., & Hernquist, L. 2019, MNRAS, 485, 1579
King, A. 2003, ApJL, 596, L27
Kocsis, B., & Levin, J. 2012, PhRvD, 85, 123005
Kormendy, J., & Ho, L. C. 2013, ARA&A, 51, 511
Kozai, Y. 1962, AJ, 67, 591
Li, G., Naoz, S., Kocsis, B., & Loeb, A. 2015, MNRAS, 451, 1341
Lidov, M. L. 1962, P&SS, 9, 719
Lidov, M. L., & Ziglin, S. L. 1976, CeMec, 13, 471
Lithwick, Y., & Naoz, S. 2011, ApJ, 742, 94
Liu, B., & Lai, D. 2020, PhRvD, 102, 023020
Luna, A., Minniti, D., & Alonso-García, J. 2019, ApJL, 887, L39
Mastrobuono-Battisti, A., Perets, H. B., & Loeb, A. 2014, ApJ, 796, 40
McKernan, B., Ford, K. E. S., Lyra, W., & Perets, H. B. 2012, MNRAS, 425, 460
Meiron, Y., Kocsis, B., & Loeb, A. 2017, ApJ, 834, 200
Meiron, Y., & Laor, A. 2013, MNRAS, 433, 2502
Merritt, D. 2006, ApJ, 648, 976
Mezcua, M. 2017, IJMPD, 26, 1730021
Naoz, S. 2016, ARA&A, 54, 441
Naoz, S., Kocsis, B., Loeb, A., & Yunes, N. 2013, ApJ, 773, 187
Naoz, S., & Silk, J. 2014, ApJ, 795, 102
Naoz, S., Silk, J., & Schnittman, J. D. 2019, ApJL, 885, L35
Naoz, S., Will, C. M., Ramirez-Ruiz, E., et al. 2020, ApJL, 888, L8
Neumayer, N., Seth, A., & Böker, T. 2020, A&ARv, 28, 4
O'Leary, R. M., Kocsis, B., & Loeb, A. 2009, MNRAS, 395, 2127
Peters, P. C. 1964, PhRv, 136, 1224
Portegies Zwart, S. F., Baumgardt, H., McMillan, S. L. W., et al. 2006, ApJ, 641, 319
Randall, L., & Xianyu, Z.-Z. 2019, arXiv:1902.08604
Rasskazov, A., Fragione, G., Leigh, N. W. C., et al. 2019, ApJ, 878, 17
Robertson, B., Bullock, J. S., Cox, T. J., et al. 2006, ApJ, 645, 986
Sesana, A., Gualandris, A., & Dotti, M. 2011, MNRAS, 415, L35
Tagawa, H., Haiman, Z., & Kocsis, B. 2020, ApJ, 898, 25
Wegg, C., & Nate Bode, J. 2011, ApJL, 738, L8
Yu, Q., & Tremaine, S. 2003, ApJ, 599, 1129
Yunes, N., Miller, M. C., & Thornburg, J. 2011, PhRvD, 83, 044030

CHAPTER 4

Single-Single Interactions: Implications for LIGO

Theoretical models of galactic nuclei have long predicted a built up cusp of COs in nuclear clusters (e.g. Bahcall & Wolf, 1976, 1977). Moreover, as we show in Hoang et al. (2022), a majority of massive stellar binaries are disrupted by natal kicks, and a majority of the resulting single COs are retained in the cluster. Thus, we expect a large number of single compact remnants in galactic nuclei. In dense clusters, objects frequently undergo close, almost parabolic encounters with each other (Quinlan & Shapiro, 1987; Lee, 1993). In encounters of this type between two COs, a burst of energy is released in the form of GWs (Peters & Mathews, 1963; Turner, 1977). If enough enough energy is released to overcome the kinetic energy of the encounter, a very eccentric binary will form and very quickly merge (Lee, 1993; O'Leary et al., 2009, e.g.). This mechanism has been previously invoked to explain BH-BH mergers in galactic nuclei (O'Leary et al., 2009; Tsang, 2013; Gondán et al., 2018b, e.g.).

In Hoang et al. (2020), presented below, we explore GW captures as a way to create NSBH mergers in nuclear, globular, and young stelar clusters Hoang et al. (2020). Thus far, two NSBH mergers have been detected by LIGO/Virgo, leading to an inferred NSBH merger rate in the local universe to be 45^{+75}_{-33} Gpc^{-3}yr^{-1}, when assuming that the detected mergers are representative of the overall NSBH population; or 130^{+112}_{-69} Gpc^{-3}yr^{-1}, when assuming a broader underlying mass spectrum (Abbott et al., 2021a). We found that GW captures is unlikely to be the dominant formation channel for NSBH mergers. However, this conclusion is based on theoretical stellar cusp densities models, which the merger rate directly depends on. Furthermore, unlike other formation channels, most mergers from GW captures have been shown to be still very eccentric in the LIGO band, providing a natural way to identify them (Takátsy et al., 2019; Gondán et al., 2018a; Gondán & Kocsis, 2019, 2021). Thus, assuming that templates for eccentric GW mergers are developed, we will be able to use observational rates of NS-BH mergers to inform our understanding of the density distributions of COs in galactic nuclei and other types of clusters.

The Astrophysical Journal, 903:8 (9pp), 2020 November 1 https://doi.org/10.3847/1538-4357/abb66a

Neutron Star–Black Hole Mergers from Gravitational-wave Captures

Bao-Minh Hoang[1,2], Smadar Naoz[1,2], and Kyle Kremer[3,4,5,6]
[1] Department of Physics and Astronomy, University of California, Los Angeles, Los Angeles, CA 90095, USA; bmhoang@astro.ucla.edu
[2] Mani L. Bhaumik Institute for Theoretical Physics, Department of Physics and Astronomy, UCLA, Los Angeles, CA 90095, USA
[3] Department of Physics & Astronomy, Northwestern University, Evanston, IL 60208, USA
[4] Center for Interdisciplinary Exploration & Research in Astrophysics (CIERA), Northwestern University, Evanston, IL 60208, USA
[5] The Observatories of the Carnegie Institution for Science, Pasadena, CA 91101, USA
[6] Theoretical Astrophysics, and Walter Burke Institute for Theoretical Physics, Caltech, Pasadena, CA 91125, USA
Received 2020 July 14; revised 2020 September 3; accepted 2020 September 4; published 2020 October 26

Abstract

LIGO's third observing run (O3) has reported several neutron star–black hole (NSBH) merger candidates. From a theoretical point of view, NSBH mergers have received less attention in the community than either binary black holes, or binary neutron stars. Here we examine single–single (sin–sin) gravitational wave (GW) captures in different types of star clusters—galactic nuclei, globular clusters, and young stellar clusters—and compare the merger rates from this channel to other proposed merger channels in the literature. There are currently large uncertainties associated with every merger channel, making a definitive conclusion about the origin of NSBH mergers impossible. However, keeping these uncertainties in mind, we find that sin–sin GW capture is unlikely to significantly contribute to the overall NSBH merger rate. In general, it appears that isolated binary evolution in the field or in clusters, and dynamically interacting binaries in triple configurations, may result in a higher merger rate.

Unified Astronomy Thesaurus concepts: Neutron stars (1108); Stellar mass black holes (1611); Gravitational wave sources (677); Young star clusters (1833); Globular star clusters (656); Galactic center (565); Stellar dynamics (1596)

1. Introduction

The recent gravitational wave (GW) detections of merging binary black holes (BBHs) and binary neutron stars (BNSs; Abbott et al. 2016a, 2016b, 2017a, 2017b, 2017c, 2017d, 2019a) by LIGO/Virgo have ushered in a golden age of GW astrophysics. The first (O1) and second (O2) observing runs of the advanced LIGO/Virgo detector network have yielded inferred estimates for the merger rate of BBHs (9.7–101 $\mathrm{Gpc^{-3}\,yr^{-1}}$) and BNSs (110–3840 $\mathrm{Gpc^{-3}\,yr^{-1}}$) (Abbott et al. 2019b). A very diverse range of mechanisms and astrophysical environments have been invoked to explain these mergers, such as dynamical interactions in globular clusters (GCs; e.g., Portegies Zwart & McMillan 2000; Wen 2003; O'Leary et al. 2006, 2016; Antonini et al. 2014; Rodriguez et al. 2016; Kremer et al. 2020b; Samsing et al. 2020) and galactic nuclei (GN; e.g., O'Leary et al. 2009; Antonini & Perets 2012; Kocsis & Levin 2012; Ramirez-Ruiz et al. 2015; Hoang et al. 2018; Fernández & Kobayashi 2019), active galactic nuclei (e.g., McKernan et al. 2012; Bartos et al. 2017; Stone et al. 2017; Secunda et al. 2019), isolated binary evolution in the field (e.g., Belczynski et al. 2016; de Mink & Mandel 2016; Mandel & de Mink 2016; Marchant et al. 2016), Population III stars (e.g., Kinugawa et al. 2014, 2016; Dvorkin et al. 2016; Hartwig et al. 2016; Inayoshi et al. 2016), and primordial black holes (e.g., Bird et al. 2016; Sasaki et al. 2016; Clesse & García-Bellido 2017).

The nondetection of any neutron star–black hole (NSBH) mergers during O1 and O2 puts a 90% confidence interval upper limit on the NSBH merger rate of 0–610 $\mathrm{Gpc^{-3}\,yr^{-1}}$. However, there are currently several candidates for NSBH mergers in O3 and it is likely that there will be a confirmed detection within the decade (see The LIGO Scientific collaboration 2020). NSBHs are much less well studied than either BBHs or BNSs. However, over the years there have been a number of studies estimating the rate of NSBH mergers from a number of channels. In this work we explore a relatively unexplored channel for producing NSBH mergers—eccentric GW captures in dense clusters. GW captures have been well studied as a promising formation mechanism for BBHs, particularly in GN. NSBH captures are less straightforward than BBH captures due to the potential presence of tidal effects. Furthermore, NSs and BHs interact with each other less often than they do with members of their own species due to mass segregation in clusters. We explore these complications in three different types of clusters in this work: GNs, GCs, and young stellar clusters (YSCs). We then compare our results to results from other channels, consider the limits of the different channels, and finally discuss likely origins for a future NSBH merger detection in LIGO. We begin by summarizing the various channels that have been proposed to explain NSBH mergers below:

1. *Mergers in the Field*: The most well studied channel for merging NSBH is binary evolution in the field. Early studies using population synthesis have resulted in a large range of merger rates, 0.68–42.8 $\mathrm{yr^{-1}}$ in aLIGO, due to many uncertainties in binary evolution models (e.g., Sipior & Sigurdsson 2002; Pfahl et al. 2005; Belczynski et al. 2007, 2010; O'Shaughnessy et al. 2010). Belczynski et al. (2011) studied X-ray source Cyg X-1—a likely NSBH progenitor—and found an "empirical" rate of NSBH mergers based on the evolution of this system: (2–14) $\times\,10^{-10}\,\mathrm{yr^{-1}\,gal^{-1}}$ (inferred volumetric rate $\sim$0.002–0.014 $\mathrm{Gpc^{-3}\,yr^{-1}}$), which is much smaller than the previously estimated rates from population synthesis. A more recent binary population synthesis study by Dominik et al. (2015) estimated NSBH merger rates in aLIGO to be 0.6–1.2 $\mathrm{yr^{-1}}$ for a standard binary evolution model, up to 3.6–5.7 $\mathrm{yr^{-1}}$ for an optimistic common envelope evolution model, and down to 0.03–0.3 $\mathrm{yr^{-1}}$ for

a pessimistic model with high BH kicks (inferred volumetric rate across all models $\sim$0.1–14 $\mathrm{Gpc^{-3}\,yr^{-1}}$). More recently, Kruckow et al. (2018) found an optimistic upper limit to NSBH mergers via isolated binary evolution in the field of up to $\sim$53 $\mathrm{Gpc^{-3}\,yr^{-1}}$.

2. *Mergers in Globular Clusters*: NSs have been well-observed in GCs dating back to the 1970s as both X-ray (e.g., Clark 1975; Heinke et al. 2005) and radio sources (e.g., Lyne et al. 1987; Ransom 2008). Over the past decade, a growing amount of evidence has suggested GCs also retain BH populations (e.g., Strader et al. 2012; Giesers et al. 2019). Thus the question of NSBH formation in GCs arises naturally. Several studies have suggested that the rate of NSBH mergers is much lower in GCs than in the field through various lines of reasoning (Phinney 1991; Grindlay et al. 2006; Sadowski et al. 2008). A few authors have since calculated the rates of NSBH mergers in GC through dynamical processes. For example, Clausen et al. (2013) studied binary–single (bin–sin) interactions in a static cluster potential, and found a merger rate of $\sim$0.01–0.17 $\mathrm{Gpc^{-3}\,yr^{-1}}$. More recently, Ye et al. (2020) studied dynamically formed NSBHs in GCs using the code CMC (Cluster Monte Carlo, see Kremer et al. 2020b for details), and found a rate of 0.009–0.06 $\mathrm{Gpc^{-3}\,yr^{-1}}$. Arca Sedda (2020) studied hyperbolic bin–sin interactions in dense clusters, and found an NSBH merger rate of 3.2×10^{-3} –0.25 $\mathrm{Gpc^{-3}\,yr^{-1}}$ in GCs. The upper limits of these GC rates are indeed only comparable to the lower limits of the theoretical field rates, supporting the idea that field channels dominate over GC channels for NSBH mergers. Note that all three of the aforementioned studies focused on *binary-mediated* interactions, i.e., binary–single (bin–sin), and binary–binary (bin–bin) interactions, and did not include *single–single (sin–sin)* encounters, which will be the focus of this paper.

3. *Mergers in Galactic Nuclei*: The extent of previous studies for NSBH mergers in GN are similarly limited. For example, Arca Sedda (2020) studied bin–sin mergers in GN and found a rate of $\sim 9 \times 10^{-3}$–1.5×10^{-2} $\mathrm{Gpc^{-3}\,yr^{-1}}$. O'Leary et al. (2009) focused on mergers of BBHs in GN resulting from sin–sin GW captures (e.g., Quinlan & Shapiro 1987; Lee 1993), using compact object densities resulting from Fokker–Planck simulations. They estimated that the rate of NSBH mergers from this channel will be roughly $10^{-11}\,\mathrm{yr^{-1}\,gal^{-1}}$ for a GN around a $4 \times 10^6\,M_\odot$ SMBH, or 1% of the BBH rate. Tsang (2013) also estimated the rate of NSBH mergers in GN, but using density profiles of an isothermal sphere instead of density profiles from a Fokker–Planck simulation, and found a merger rate of $\sim 7 \times 10^{-11}$–$9 \times 10^{-10}\,\mathrm{yr^{-1}\,gal^{-1}}$ for a GN surrounding a $4 \times 10^6\,M_\odot$ SMBH (calculated from their Equation (A9)).

We note that there is a great deal of subtlety and uncertainty concerning the conversion of a per galaxy merger rate for fixed SMBH mass to a volumetric/expected detection rate for GW captures in GN. The most straightforward way is to simply multiply the per galaxy rate by a galaxy number density in the universe to find the volumetric rate; and then multiply the volumetric rate by the volume observable by LIGO to find an expected detection rate. However, as O'Leary et al. (2009) noted, there may be significant variance in central cusp densities between different GNs with the *same SMBH mass*. Since the rate of GW captures scales as density squared, this variance may lead to an enhancement of the aforementioned volumetric/expected detection rate by a factor of ξ. The true value of ξ is highly uncertain. Whereas O'Leary et al. (2009) and Kocsis & Levin (2012) estimate ξ to be $\gtrsim$30, Tsang (2013) found that ξ is at most $\sim$14 under very optimistic assumptions. O'Leary et al. (2009) and Tsang (2013) found volumetric (expected LIGO detection) rates of $\sim$0.07 $\mathrm{Gpc^{-3}\,yr^{-1}}$ ($\sim$1 $\mathrm{yr^{-1}}$) and $\sim$0.05–0.6 $\mathrm{Gpc^{-3}\,yr^{-1}}$ ($\sim$1.6–20 $\mathrm{yr^{-1}}$), respectively, using their different values of ξ. Without enhancement from ξ, these rates will decrease to roughly $\sim$0.002 $\mathrm{Gpc^{-3}\,yr^{-1}}$ ($\sim$0.03 $\mathrm{yr^{-1}}$) and $\sim$0.004–0.05 $\mathrm{Gpc^{-3}\,yr^{-1}}$ (0.1–1.5 $\mathrm{yr^{-1}}$), respectively. Due to the high uncertainty in the value of ξ, in this work we calculate and adopt GW capture rates *without* ξ as our fiducial rates, which yields conservative estimations. However, we will discuss the implications for LIGO should ξ be significant. Aside from GW captures, GN can be the site of binary mergers induced by interactions with the SMBH (e.g., Antonini & Perets 2012; Naoz 2016; Stephan et al. 2016, 2019; Hoang et al. 2018), via the Eccentric Kozai–Lidov Mechanism (EKL Kozai 1962; Lidov 1962; Naoz 2016). Recently Lu & Naoz (2019) suggested that supernova natal kicks can tend to shrink the post supernova separation. Moreover they showed that these systems are more likely to stay in a triple configuration near an SMBH. On the other had, a supernova kick rarely keeps stellar-mass tertiary. Thus, torques from the SMBH can lead to enhancement of NSBH mergers, compared to field binaries.

Subsequently, Stephan et al. (2019) studied stellar binary evolution in GN with EKL including self-consistent post-main sequence stellar evolution and found that LIGO may detect NSBH mergers from this mechanism at a rate of 2–5 $\mathrm{yr^{-1}}$ (inferred volumetric rate: 0.17–0.33 $\mathrm{Gpc^{-3}\,yr^{-1}}$). Fragione et al. (2019a) performed a study of compact binary mergers in GN induced by EKL, considering different binary parameter distributions and SMBH masses, and found an NSBH merger rate of 0.06–0.1 $\mathrm{Gpc^{-3}\,yr^{-1}}$. Comparing these EKL rates to the sin–sin GW capture rates from O'Leary et al. (2009) and Tsang (2013), we see that if ξ is small (i.e., the variance in GN density is low), mergers induced by EKL will dominate over mergers from GW captures in GN. Conversely, if ξ is significant, then mergers from GW captures will be either comparable to or dominate over mergers from EKL.

Recently, McKernan et al. (2020) studied compact object binary mergers in AGN disks, the gas that has previously been shown to potentially accelerate binary mergers (e.g., McKernan et al. 2012; Bartos et al. 2017; Stone et al. 2017; Secunda et al. 2019). They found that this channel can potentially produce NSBH mergers at rates of $f_{\mathrm{AGN,BBH}}$ (10–300) $\mathrm{Gpc^{-3}\,yr^{-1}}$, where $f_{\mathrm{AGN,BBH}}$ is the fraction of BBH mergers observed by LIGO that come from the AGN channel. They expect that 10%–20% of NSBH mergers from this channel will have electromagnetic counterparts, which can help disentangle this channel from others.

4. *Mergers in Young Stellar Clusters*: Most stars, including massive stars that are BH and NS progenitors, are born in YSCs (Carpenter 2000; Lada & Lada 2003; Porras et al. 2003). Their higher density relative to the galactic field means that compact binaries can form from dynamical interactions similar to those in GCs, as well as from stellar binary evolution. As a result, a number of studies have explored YSCs as a possible birthplace for BBHs (e.g., Portegies Zwart & McMillan 2002; Banerjee et al. 2010; Kouwenhoven et al. 2010; Goswami et al. 2014; Ziosi et al. 2014; Mapelli 2016; Banerjee 2017, 2018; Fujii et al. 2017; Di Carlo et al. 2019; Kumamoto et al. 2019; Rastello et al. 2019), with promising results. Recently, Rastello et al. (2020) studied the formation of NSBHs in YSCs from redshifts 0–15. They found that YSCs can produce NSBHs that merge in the local universe (redshift <0.1) at a rate of $\sim 28\,\mathrm{Gpc}^{-3}\,\mathrm{yr}^{-1}$, through a combination of binary evolution and dynamical interactions. Most of these NSBHs will be ejected from YSCs before they merge, and so will ostensibly be "field" binaries when they are detected by LIGO. However, NSBHs that formed in YSCs have a different mass spectrum from those that formed in true isolation in the field, and may be differentiated in this way. The rate found in Rastello et al. (2020) is likely an optimistic estimation of the YSC merger rate, due to the following reasons. Rastello et al. (2020) assume an NS natal kick distribution with an rms of $15\,\mathrm{km\ s}^{-1}$, whereas observational studies of pulsar proper motions in the literature show that a majority of NSs likely receive very large natal kicks ($\sim$200–500 $\mathrm{km\ s}^{-1}$) at birth (e.g., Hansen & Phinney 1997; Lorimer et al. 1997; Cordes & Chernoff 1998; Fryer et al. 1999; Hobbs et al. 2004, 2005; Beniamini & Piran 2016). High velocity natal kicks tend to disrupt binaries and may significantly reduce the rate of NSBH formation from binary evolution. In addition, the high stellar densities and fractal initial conditions adopted in Rastello et al. (2020) may not be representative of all YSCs, and therefore may overestimate the influence of dynamics. For comparison, lower density models found in another recent work, Fragione & Banerjee (2020), resulted in an upper limit of 3×10^{-3} $\mathrm{Gpc}^{-3}\,\mathrm{yr}^{-1}$ for the NSBH merger rate from binary evolution and dynamical exchanges in YSCs. Note that while the analysis in Rastello et al. (2020) and Fragione & Banerjee (2020) included dynamical binary interactions and exchanges, they also did not include sin–sin GW capture. We will give an order of magnitude upper limit estimation of the rate of NSBH mergers due to sin–sin GW captures in YSCs in this work.
5. *Mergers in Triples:* Stellar multiplicity studies have shown that $\sim$15% of massive stars—progenitors of BHs and NSs—have at least two stellar companions (e.g., Raghavan et al. 2010; Sana et al. 2013; Dunstall et al. 2015; Jiménez-Esteban et al. 2019). Several studies have explored the formation of BBH mergers in stellar triples and quadruples (e.g., Antonini et al. 2017; Silsbee & Tremaine 2017; Fragione & Kocsis 2019; Liu & Lai 2019). Recently, Fragione & Loeb (2019a) and Fragione & Loeb (2019b) studied NSBH mergers in field triples and found merger rates of $\sim 1.9 \times 10^{-4}$–$22\,\mathrm{Gpc}^{-3}\,\mathrm{yr}^{-1}$, where the wide range comes from uncertainties in the metallicity of the progenitor population, and the magnitude of BH and NS natal kick velocities.

The paper is organized as follows: We begin with describing the basic equations that govern sin–sin GW capture in Section 2. We then calculate the sin–sin NSBH merger rate in GCs, GNs, and YSCs in Section 3. Finally, we offer our discussions about the most probably NSBH merger channels in Section 4.

2. Single–Single Gravitational-wave Captures

Two compact objects undergoing a close encounter can emit enough gravitational wave energy to become a bound binary. Because these encounters are relativistic, and the velocity dispersion of galactic nuclei and other clusters are much less than the speed of light, they are almost always nearly parabolic (Quinlan & Shapiro 1987; Lee 1993). We consider these approximately parabolic encounters and subsequent gravitational wave captures of stellar-mass black holes of mass m_{BH} and neutron stars of mass m_{NS}, total mass $M_{\mathrm{tot}} = m_{\mathrm{BH}} + m_{\mathrm{NS}}$, a symmetric mass ratio $\eta = m_{\mathrm{BH}} m_{\mathrm{NS}}/((m_{\mathrm{BH}} + m_{\mathrm{NS}})^2)$, a relative velocity of v_{rel}, and an impact parameter of b. The energy that is emitted in GWs in such an encounter is (Peters & Mathews 1963; Turner 1977):

$$\Delta E_{\mathrm{GW}} = -\frac{85\pi G^{7/2}}{12\sqrt{2}\,c^5}\frac{\eta^2 M_{\mathrm{tot}}^{9/2}}{r_{\mathrm{p}}^{7/2}}, \tag{1}$$

where c is the speed of light, G is the gravitational constant, and r_{p} is the distance of closest approach of the encounter:

$$r_p = \left(\sqrt{\frac{1}{b^2} + \frac{G^2 M_{\mathrm{tot}}^2}{b^4 v_{\mathrm{rel}}^4}} + \frac{G M_{\mathrm{tot}}}{b^2 v_{\mathrm{rel}}^2}\right)^{-1}. \tag{2}$$

If $|\Delta E_{\mathrm{GW}}| > \frac{1}{2} M_{\mathrm{tot}} \eta v_{\mathrm{rel}}^2$ (the kinetic energy of the encounter), a bound NSBH binary is formed (e.g., Lee 1993). This criterion implies a maximum impact parameter b_{max} to form a bound binary (e.g., O'Leary et al. 2009; Gondán et al. 2018a):

$$b_{\mathrm{max}} = \left(\frac{340\pi\eta}{3}\right)^{1/7} \frac{G M_{\mathrm{tot}}}{c^2} \left(\frac{v_{\mathrm{rel}}}{c}\right)^{-9/7}. \tag{3}$$

There is also a minimum impact parameter b_{min} to form bound binaries, as encounters with $b < b_{\mathrm{min}}$ will result in a direct collision rather than a bound binary. These encounters may result in an electromagnetic event but will likely not result in any strong GW signals. This collisional impact parameter is defined as (Gondán et al. 2018a),

$$b_{\mathrm{min}} = \frac{4 G M_{\mathrm{tot}}}{c^2} \left(\frac{v_{\mathrm{rel}}}{c}\right)^{-1}. \tag{4}$$

The total GW capture cross section is thus:

$$\sigma(m_{\mathrm{BH}}, m_{\mathrm{NS}}, v_{\mathrm{rel}}) = \pi(b_{\mathrm{max}}^2 - b_{\mathrm{min}}^2). \tag{5}$$

We note that during these encounters, energy is also lost due to tidal oscillations in the neutron star excited by the black hole (e.g., Press & Teukolsky 1977), and contributes to σ. To check whether we should include this effect in our calculations or whether it can be safely neglected, we approximate the tidal energy dissipated during a parabolic encounter according to the

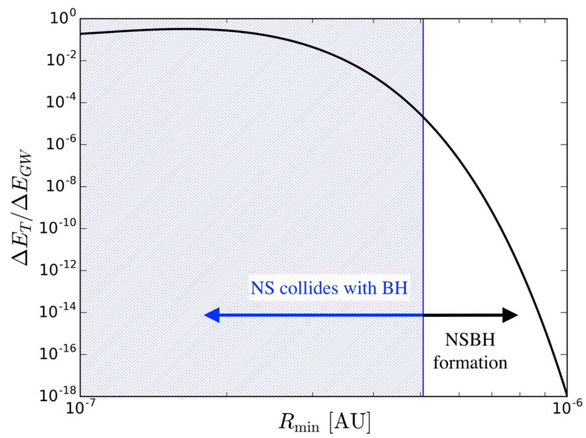

Figure 1. Ratio of energy lost to tides to energy lost to GWs ($\Delta E_{\rm T}/\Delta E_{\rm GW}$), as a function of encounter periastron ($R_{\rm min}$). Plotted for parabolic encounters between a 5 $M_\odot$ BH and a 1.4 $M_\odot$ NS. The region highlighted blue denotes encounters with impact parameter less than $b_{\rm min}$ (given by Equation (4))—these encounters will result in a direct collision between the BH and NS. The region of interest for us is the region to the right of the blue line, where an NSBH can form. In this region, $\Delta E_{\rm T}/\Delta E_{\rm GW} < 10^{-4}$, an extremely small value. We note that encounters between an NS and a BH of mass greater than 5 $M_\odot$ will result in even smaller values of $\Delta E_{\rm T}/\Delta E_{\rm GW}$. Thus, we conclude that we can ignore tidal effects in our calculations.

formalism presented in Press & Teukolsky (1977):

$$\Delta E_{\rm T} = \left(\frac{Gm_{\rm NS}^2}{R_{\rm NS}}\right)\left(\frac{m_{\rm BH}}{m_{\rm NS}}\right)^2 \sum_{l=2,3,\ldots}\left(\frac{R_{\rm NS}}{R_{\rm min}}\right)^{2l+2} T_l, \tag{6}$$

where $R_{\rm NS}$ is the radius of the neutron star, $R_{\rm min}$ is the periastron of the approach, and T_l are dimensionless values associated with each spherical harmonic l (see Press & Teukolsky 1977 for calculation of T_l). We only consider the quadrupole mode ($l = 2$), which dominates over the other modes (Press & Teukolsky 1977). We approximate the NS as a polytropic star of index $n = 0.5$ (e.g., Finn 1987), and use values from Table 1 of Kokkotas & Schafer (1995) to aid in the calculation of T_l. Note that since there is a minimum impact parameter, there is a minimum possible value of $R_{\rm min}$. For a parabolic encounter the relationship between the impact parameter and the periastron distance is:

$$R_{\rm min}(b) = \frac{b^2 v_{\rm rel}^2}{2GM_{\rm tot}}. \tag{7}$$

Thus, combining Equations (4) and (7), we find the minimum possible $R_{\rm min}$ to be:

$$R_{\rm min}(b_{\rm min}) = \frac{8GM_{\rm tot}}{c^2}. \tag{8}$$

Encounters with $R_{\rm min} < R_{\rm min}(b_{\rm min})$ will result in a direct collision between the BH and NS instead of a bound binary. In Figure 1 we plot $\Delta E_{\rm T}/\Delta E_{\rm GW}$—the ratio of energy lost to tidal oscillations to the energy lost to gravitational waves—as a function of $R_{\rm min}$, for a 5 $M_\odot$ BH and a 1.4 $M_\odot$ NS. We have also marked the region where $R_{\rm min} < R_{\rm min}(b_{\rm min})$. We see that in the region of interest where $R_{\rm min} > R_{\rm min}(b_{\rm min})$, i.e., where bound binaries can form, $\Delta E_{\rm T}/\Delta E_{\rm GW} < 10^{-4}$, an extremely small value. We have verified (not shown to avoid clutter) that for larger BH masses, $\Delta E_{\rm T}/\Delta E_{\rm GW}$ is even smaller. This is consistent with previous studies about NS–NS captures (e.g., Gold et al. 2012; Chirenti et al. 2017). Thus, we can safely neglect tides in our calculation of the capture cross section.

3. Event Rates

The rate of NSBH binary formation for a single cluster is:

$$\begin{aligned}\Gamma_{\rm cl} = &\int dr\, 4\pi r^2 n_{\rm BH}(r) n_{\rm NS}(r)\\ &\times \int dm_{\rm BH}\, \mathcal{F}_{\rm BH}(m_{\rm BH}) \int dm_{\rm NS}\, \mathcal{F}_{\rm NS}(m_{\rm NS})\\ &\times \int dv_{\rm rel}\, \psi_{m_{\rm BH},m_{\rm NS}}(r, v_{\rm rel})\sigma v_{\rm rel},\end{aligned} \tag{9}$$

where $n_{\rm BH}(r)$ and $n_{\rm NS}(r)$ are the number densities of black holes and neutron stars, respectively; $\mathcal{F}_{\rm BH}(m_{\rm BH})$ and $\mathcal{F}_{\rm NS}(m_{\rm NS})$ are the mass probability distributions for black holes and neutron stars, respectively; $\psi_{m_{\rm BH},m_{\rm NS}}(r, v_{\rm rel})$ is the distribution of the relative velocity between $m_{\rm BH}$ and $m_{\rm NS}$ at r.

For GCs, we approximate the BH and NS populations of each cluster as following a Maxwellian velocity distribution. Thus, the BH and NS populations have velocity dispersions of $v_{\rm d,BH}$ and $v_{\rm d,NS}$, respectively. We then calculate the average relative velocity between BHs and NSs in a cluster, $\langle v_{\rm rel}\rangle = \sqrt{(8/\pi)(v_{\rm d,BH}^2 + v_{\rm d,NS}^2)}$, and use this constant value in Equation (9). Note that in this calculation we have neglected any mass or r dependence in $v_{\rm rel}$ for simplicity. Thus we have:

$$\int_{\rm GC} dv_{\rm rel}\, \psi_{m_{\rm BH},m_{\rm NS}}(r, v_{\rm rel})\sigma v_{\rm rel} \approx \sigma\langle v_{\rm rel}\rangle. \tag{10}$$

For GNs, O'Leary et al. (2009) showed that the last integral in Equation (9) is only weakly dependent on the relative velocity distribution, and is well approximated by:

$$\int_{\rm GN} dv_{\rm rel}\, \psi_{m_{\rm BH},m_{\rm NS}}(r, v_{\rm rel})\sigma v_{\rm rel} \approx \sigma v_c(r), \tag{11}$$

where $v_c(r) = \sqrt{Gm_{\rm SMBH}/r}$ is the circular velocity at r and σ is evaluated at $v_{\rm rel} = v_c(r)$.

We can then calculate the nominal volumetric NSBH merger rate due to sin–sin GW capture:

$$\Gamma_{\rm NSBH} = n_{\rm cl}\Gamma_{\rm cl}, \tag{12}$$

where $n_{\rm cl}$ is the density of clusters (either GN or GC, we use a slightly different calculation for YSCs, see Section 3.3) in the local universe and $\Gamma_{\rm cl}$ is the rate per cluster. Note that even though the capture rate is not technically the same as the merger rate, the vast majority of binaries that form due to GW capture tend to be very tight, eccentric, and merge very quickly after capture. Thus, the capture rate is an extremely good approximation of the merger rate (e.g., O'Leary et al. 2009; Gondán et al. 2018a).

3.1. Globular Clusters

We calculate the capture rates for a single simulated cluster that is representative of a typical Milky Way cluster (initial cluster mass $4 \times 10^5\, M_\odot$, final mass $2 \times 10^5\, M_\odot$, core radius ~1 pc, galactocentric distance of 8 kpc with Milky Way–like potential, and metallicity of $0.01 Z_\odot$), taken from the latest CMC catalog (Kremer et al. 2020b). We compare the contribution from younger clusters versus older clusters by considering this simulated cluster at 1 Gyr and 10 Gyr. To

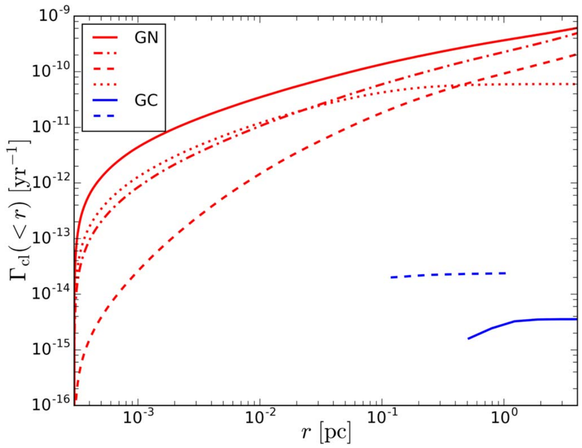

Figure 2. Cumulative merger rate per cluster $\Gamma_{\rm cl}$ (yr^{-1}) as a function of r. Note that for GN cases (red), r denotes the distance from the SMBH; whereas for GC cases (blue), r denotes the distance away from GC center. The GC lines do not extend below $r \sim 0.1$ pc because our GC models do not show NSs in the inner regions of the cluster, see Section 3.1 for more details. For GN cases, the four different curves correspond to four different GN evolution models from Figures 1 and 2 of AP16 (see Section 3.2 for a short description of Models 1–4, and AP16 for full details): solid—Model 1, dashed–dotted—Model 2, dashed—Model 3, dotted—Model 4. For GC cases, the solid line corresponds to the 1 Gyr case, and the dashed line corresponds to the 10 Gyr case.

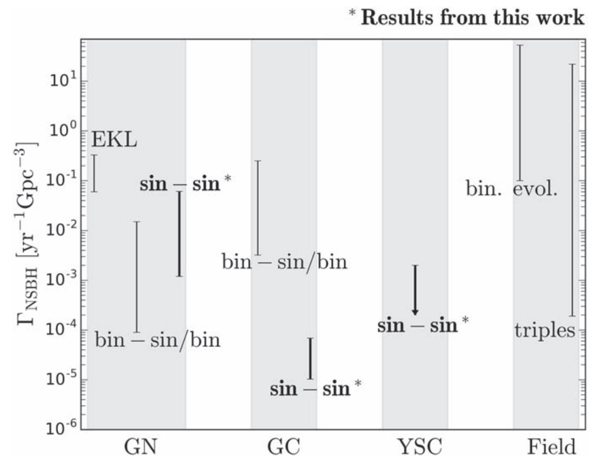

Figure 3. Comparison of NSBH merger rates from various channels. We group merger channels into four major categories: mergers taking place in galactic nuclei (GN), globular clusters (GCs), young stellar clusters (YSCs), and the galactic field. Within the GN category we highlight three channels: EKL-assisted mergers (Stephan et al. 2019); binary-mediated interactions (bin–sin/bin; Arca Sedda 2020); and sin–sin GW captures (this work). Within the GC category we show rates from binary-mediated interactions (bin–sin/bin; Clausen et al. 2013; Arca Sedda 2020; Ye et al. 2020); and sin–sin GW captures (this work). Within the YSC category we show the rate from sin–sin GW captures (this work). We denote this rate with an arrow to indicate that this is an upper limit estimation. Within the Field category we show rates from isolated bin. evol. (iso. bin; Dominik et al. 2015; Kruckow et al. 2018); and field triples (Fragione & Loeb 2019a, 2019b).

perform the integral in Equation (9), we numerically calculate the densities $n_{\rm BH}(r)$ and $n_{\rm NS}(r)$, and the mass distributions $\mathcal{F}_{\rm BH}(m_{\rm BH})$ and $\mathcal{F}_{\rm NS}(m_{\rm NS})$ from the simulation data (note this particular simulation contains 527 BHs and 825 NSs at $t = 1$ Gyr and contains 38 BHs and 778 NSs at $t = 10$ Gyr). As previously mentioned in this section, we adopt Maxwellian velocity distribution for the BH and NS populations. We fit the BH and NS velocities with respect to cluster center to a Maxwellian distribution in order to find their velocity dispersions, and from those velocity dispersions calculate the average relative velocity $\langle v_{\rm rel}\rangle$ (see Equation (10)). In Figure 2, we show the cumulative merger rate of a cluster as a function of distance, r, from the center for the young (blue, solid line) and old (blue, dashed line) cluster.

We find a total merger rate per GC of $\Gamma_{\rm cl,GC} \sim 4 \times 10^{-15}\,{\rm yr}^{-1}$ ($2 \times 10^{-14}\,{\rm yr}^{-1}$) for the 1 Gyr (10 Gyr) GC. In the younger 1 Gyr cluster, the BH population contains many higher mass BHs (mass range 5–40 $M_\odot$). Through mass segregation, this BH population forms a dense subsystem in the cluster's center that subsequently generates significant energy through "BH burning" (the cumulative effect of dynamical binary formation, hardening, and ejections; for review, see Kremer et al. 2020a). This process influences the large-scale structural properties of the host cluster, in particular, delaying the onset of cluster core collapse by preventing the migration of lower-mass stars, including NSs, to the cluster's center (e.g., Merritt et al. 2004; Mackey et al. 2008; Breen & Heggie 2013; Peuten et al. 2016; Wang et al. 2016; Arca Sedda et al. 2018; Kremer et al. 2019; Ye et al. 2020). As a result, there is only density overlap between BHs and NSs in the outer regions of the cluster where densities are low (i.e., there are no NSs in the inner most regions where the BHs dominate). This results in an extremely low rate of capture.

However, as the cluster ages, the total number of retained BHs decreases as a result of the dynamics within the BH subsystem (see, e.g., Morscher et al. 2015). Additionally, because the highest mass BHs are dynamically ejected first, as the cluster ages, the BH mass distribution becomes increasingly dominated by lower-mass BHs (5–15 $M_\odot$). As a consequence of these effects, the energy generated through the BH burning process (and therefore effect of the BHs on the cluster's radial profile) becomes less significant as the cluster ages. Thus, the NS population is able to infiltrate the inner regions of the cluster more effectively, resulting in more overlap between the BH and NS in the $r \sim 0.05$–1 pc region, where densities are higher. As a result, in general the NSBH GW capture rate is higher in dynamically older GCs than in dynamically younger ones. However, even in the 10 Gyr GC, the NSBH capture rate is extremely low. Adopting $n_{\rm cl} = 2.9\,{\rm Mpc}^{-3}$ for the density of GCs in the universe (e.g., Portegies Zwart & McMillan 2000), we find volumetric rates of $\Gamma_{\rm NSBH,GC} \sim 10^{-5}\,{\rm Gpc}^{-3}\,{\rm yr}^{-1}$ ($7 \times 10^{-5}\,{\rm Gpc}^{-3}\,{\rm yr}^{-1}$) for the 1 Gyr (10 Gyr) case. This is at least one order of magnitude below every other proposed channel, see Figure 3. Thus, we conclude that single–single GW capture is not a major contributor to the NSBH merger rate in GCs.

3.2. Galactic Nuclei

It has been shown (e.g., Bahcall & Wolf 1977) that a spherically symmetric multimass stellar population orbiting an SMBH within its radius of influence will relax into a power-law number density profile of the form $n \propto r^{-\alpha}$, where α varies with mass. The most massive members of the cluster will tend to segregate to the center of the cluster. This problem has been studied by various authors using the Fokker–Planck formalism with various assumptions about the GN environment (e.g., Bahcall & Wolf 1977; Freitag et al. 2006; Hopman & Alexander 2006; Alexander & Hopman 2009; Keshet et al. 2009; O'Leary et al. 2009; Aharon & Perets 2016). For this work we calculate GW capture rates in GN using

BH and NS density profiles from four different scenarios studied by Aharon & Perets (2016; henceforth AP16). AP16 studied a cluster surrounding an SMBH of mass $4 \times 10^6 M_\odot$, composed of a two-mass populations of BH ($10 M_\odot$ and $30 M_\odot$), NS ($1.4 M_\odot$), white dwarfs ($0.6 M_\odot$), and main-sequence stars ($1 M_\odot$). We digitally analyzed their Figures 1 and 2 to obtain BH and NS density estimates from the four different GN evolution models they considered: Model 1—cluster evolved from preexisting cusp with compact object (CO) formation in outer cluster regions, does not include $30 M_\odot$ BH population; Model 2—similar to Model 1, but includes the $30 M_\odot$ BH population; Model 3—built-up cluster with in situ star formation in the outer cluster regions; Model 4—cluster evolved from preexisting cusp with CO formation in the inner cluster regions. See AP16 for more details about the assumptions that went into the calculation of these density profiles. We approximate the relative velocity of an encounter at distance r with the circular velocity at distance r, as shown in Equation (11). We show the cumulative merger rate per GN as a function of r for these four scenarios in Figure 2.

We find a total merger rate per GN ranging from $\Gamma_{\rm cl,GN} \sim 6 \times 10^{-11}$–$6 \times 10^{-10}\,{\rm yr}^{-1}$ for our four GN evolution scenarios. The density of GN in the universe is a very uncertain value, but is often assumed in the literature to be in the range of $\sim$0.02–0.04 ${\rm Mpc}^{-3}$ (e.g., Conselice et al. 2005; Tsang 2013). However, considering a wide range of SMBH masses it may be as high as $\sim 0.1\,{\rm Mpc}^{-3}$ (Aller & Richstone 2002; O'Leary et al. 2009). Thus, we adopt $n_{\rm cl} = 0.02$–$0.1\,{\rm Mpc}^{-3}$ for the cosmic density of GN. We then find a total volumetric rate of NSBH mergers in GN due to sin–sin GW captures of $\Gamma_{\rm NSBH,GN} \sim 0.001$–$0.06\,{\rm Gpc}^{-3}\,{\rm yr}^{-1}$

As explained in the 1 (also see O'Leary et al. 2009 and Tsang 2013), this rate may be enhanced by a factor of ξ, which accounts for the variance in central cusp densities between different GNs. The value of ξ is highly uncertain, but it may be as high as a few tens (O'Leary et al. 2009). Thus, our nominal rate of $\Gamma_{\rm NSBH,GN} \sim 0.001$–$0.06\,{\rm Gpc}^{-3}\,{\rm yr}^{-1}$ is a conservative one.

3.3. Young Stellar Clusters

We perform an order of magnitude estimation adopting models of massive YSCs from Banerjee (2017, 2018). We calculate the number density distributions of BHs and NSs, $n_{\rm BH}(r)$ and $n_{\rm NS}(r)$, from the cumulative radial distributions obtained by digitally analyzing the left-hand side plots of Figure 8 from Banerjee (2018). These radial distributions are given for a cluster with initial mass $M_{\rm cl}(t = 0) = 7.5 \times 10^4$ $M_\odot$ and metallicity $Z = 0.01\,Z_\odot$, in snapshots at $t = 100$ Myr, 1000 Myr, 5000 Myr, 7500 Myr, and 10 Gyr[7] We assume a cluster velocity dispersion of 3 km s^{-1} for $v_{\rm rel}$ (e.g., Portegies Zwart et al. 2010), and single mass distributions of BH and NS of $20 M_\odot$ and $1.4 M_\odot$, respectively. We calculate the per cluster merger rate, $\Gamma_{\rm cl,YSC}$, at different time snapshots using Equation (9). The per cluster merger rate for our nominal YSC model rapidly decreases as the cluster ages, going from $\Gamma_{\rm cl,YSC} \sim 10^{-13}\,{\rm yr}^{-1}$ at $t = 100$ Myr to $\Gamma_{\rm cl,YSC} \sim 10^{-16}\,{\rm yr}^{-1}$ for $t > 5$ Gyr. This is in contrast to what we see with our nominal GC model, where the per cluster rate slightly increases with age. This is primarily due to the fact the half-mass–radius of our nominal YSC model increases from $\sim$2 to $\sim$15 pc between 100 Myr and 10 Gyr, as shown in Figure 2 of Banerjee (2018). Cluster expansion leads to a decrease in stellar density, which greatly lowers the frequency of dynamical captures.

We then calculate the volumetric rate similarly to Ziosi et al. (2014):

$$\Gamma_{\rm NSBH,YSC} \approx \frac{\Gamma_{\rm cl,YSC}}{M_{\rm cl}(0)}\, t_{\rm eff}\, \rho_{\rm SF}\, f_{\rm SF}\,, \qquad (13)$$

where $\rho_{\rm SF} = 1.5 \times 10^{-2} M_\odot\,{\rm Mpc}^{-3}$ is the density of star formation at redshift 0 (adopted from Hopkins & Beacom 2006), and $f_{\rm SF} = 0.8$ is the fraction of star formation that takes place in YSCs (e.g., Lada & Lada 2003). Note that we calculate the locally detectable rate using the local star formation density—as opposed to an integrated cosmological calculation, like that found in Rastello et al. (2020)—since there is not typically a large time delay between binary formation and binary merger in the sin–sin GW capture channel (O'Leary et al. 2009; Gondán et al. 2018a). In other words, an NSBH formed via GW capture that merges in the local universe almost certainly formed in the local universe. In light of this, and also since we have found that the per cluster merger rate is strongly dominated by the very early YSC evolution, we consider an "effective" lifetime for our cluster to be $t_{\rm eff} = 100$ Myr (even though a $7.5 \times 10^4 M_\odot$ cluster can live up to about 10 Gyr). Thus, we take $\Gamma_{\rm cl,YSC}$ in Equation (13) to be $\Gamma_{\rm cl,YSC}(t = 100\,{\rm Myr}) \approx 10^{-13}\,{\rm yr}^{-1}$. We find $\Gamma_{\rm NSBH,YSC} \approx 2 \times 10^{-3}\,{\rm Gpc}^{-3}\,{\rm yr}^{-1}$.

We note that this is an upper limit rate estimation for the following reasons. First of all, our nominal YSC model, with a mass of $7.5 \times 10^4 M_\odot$,[8] is much more massive and contains more stellar and compact objects than the average YSC/open cluster (for comparison, the cluster models in Rastello et al. 2020 have masses ranging from 3×10^2–$10^3 M_\odot$). Thus, by using this cluster model as our fiducial model, we are overestimating the per cluster contribution for the average YSC. Second, our nominal YSC has a low metallicity of $Z = 0.01\,Z_\odot$. Since lower cluster metallicity increases the number of compact objects formed, our fiducial cluster metallicity is on the optimistic end of the spectrum.

We see that our optimistic estimation for the sin–sin merger rate in YSCs is still very low compared to the majority of other merger channels, as seen in Figure 3. Thus, we can conclude that sin–sin GW capture in YSCs most likely do not contribute to the overall NSBH merger rate.

4. Discussion

In Figure 3, we compile and compare the predicted NSBH merger rates from the merger channels discussed in Section 1,

[7] The radial distributions are normalized with respect to the total number of bound BH and NS in the cluster, $N_{\rm BH,bound}$ and $N_{\rm NS,bound}$, which are unfortunately not given in either Banerjee (2018) or Banerjee (2018) for a $M_{\rm cl}(0) = 7.5 \times 10^4$ $M_\odot$ cluster. However, the time evolution of $N_{\rm BH,bound}$ is given for four other cluster masses in the range $M_{\rm cl}(0) = (1$–$5) \times 10^4$ $M_\odot$ in Figure 4 of Banerjee (2017). Based on numbers obtained from Banerjee (2017), Figure 4, we fit $N_{\rm BH,bound}(M_{\rm cl})$ with both a linear and quadratic distribution to extrapolate a range for $N_{\rm BH,bound}(M_{\rm cl}(0) = 7.5 \times 10^4)$ at the different time snapshots. $N_{\rm NS,bound}$ is given for a $M_{\rm cl}(0) \approx 3 \times 10^4$ $M_\odot$ in Figure 2 of Banerjee (2017), from which we can calculate the ratio $N_{\rm NS,bound}/N_{\rm BH,bound}$ for $M_{\rm cl}(0) \approx 3 \times 10^4$ $M_\odot$. Assuming that this ratio is roughly constant with increasing cluster mass, we can calculate $N_{\rm NS,bound}(M_{\rm cl}(0) = 7.5 \times 10^4)$ from the extrapolated $N_{\rm BH,bound}$ values. We can now unnormalize $n_{\rm BH}(r)$ and $n_{\rm NS}(r)$ and estimate per cluster sin–sin capture rate.

[8] These relatively more massive young clusters are often referred to in the literature as "young *massive* clusters" (YMCs), see Portegies Zwart et al. (2010) for a review.

as well as the results from this work. We group these channels into four major categories: mergers taking place in GN, GC, YSC, and the galactic field. For the GN category we include the following channels: EKL-assisted mergers (rate from Stephan et al. 2019); binary mediated interactions (rate from Arca Sedda 2020); and sin–sin GW captures (rate compiled from O'Leary et al. 2009; Tsang 2013, and this work). For the GC category we include the following channels: binary mediated interactions (rate compiled from Clausen et al. 2013; Ye et al. 2020, and Arca Sedda 2020); and sin–sin GW captures (rate from this work). For the YSC category we include sin–sin GW captures (rate from this work). For the field channel we used the rates from Dominik et al. (2015) and Kruckow et al. (2018).

We see from Figure 3 that sin–sin GW captures are highly unlikely to be the dominant mechanism for the production of NSBH mergers. Indeed, sin–sin GW captures do not appear to contribute to the overall NSBH rate in any significant way. The most major caveat to this statement concerns the sin–sin estimate in the GN category. As discussed in Section 1, the sin–sin rates for GN estimated in this work may be underestimated by a "ξ" factor, which is due to the variance of stellar densities in the GN cusp. The actual value of ξ remains highly uncertain—there are both pessimistic (Tsang 2013) and optimistic (O'Leary et al. 2009) estimates of ξ in the literature. If we assume an optimistic value for ξ of a few tens, then the sin–sin GW capture rates in GN will be comparable to both the EKL and field rates.

In the future, once LIGO has detected a statistical population of NSBH mergers, we will know whether the sin–sin merger rates have been systematically underestimated here by looking at the eccentricity distribution of these mergers. It has been shown that aLIGO can distinguish eccentric stellar-mass compact binary mergers from circular ones for $e \gtrsim 0.05$–0.081 at 10 Hz (Lower et al. 2018; Gondán & Kocsis 2019). Broadly speaking, mergers from dynamical channels are expected to be more eccentric in the LIGO band than mergers from isolated binary evolution in the field, which are expected to be predominantly circular (e.g., O'Leary et al. 2009; Cholis et al. 2016; Gondán et al. 2018b; Lower et al. 2018; Rodriguez et al. 2018b; Randall & Xianyu 2018; Samsing 2018; Zevin et al. 2019). Among dynamical merger channels, some channels are predicted to yield more eccentric mergers than others. For example, Rodriguez et al. (2018a) found that roughly 6% of BBH mergers from bin–sin interactions in GCs have $e \gtrsim 0.05$ in the LIGO band.[9] For NSBH mergers from bin–sin encounters in GN, Arca Sedda (2020) found that none will have eccentricity above the minimum detection threshold in the LIGO band, but that a large fraction have $e > 0.1$ in the LISA band. Some EKL mergers are also expected to have detectable eccentricities in the LIGO band. Both Fragione et al. (2019b) and Fragione & Bromberg (2019) found that a nonnegligible fraction of BBH EKL mergers will have detectable eccentricity in the LIGO band. However, sin–sin GW capture is by far and away the merger channel that results in the most eccentric mergers in the LIGO band. Takátsy et al. (2019) studied BBH mergers in GN from both EKL and sin–sin GW captures, and found that ~75% of sin–sin GW capture mergers will have $e > 0.1$ in the LIGO band, as opposed to only ~10% for EKL. Thus, if future NSBH merger observations show a preponderance of eccentric mergers, then it is likely that we have underestimated our sin–sin merger rates here, and most likely in the context of GN.

The current nominal estimates shown in Figure 3 show four channels that are possible dominant contributors to the NSBH merger rate. These channels have overlapping statistical uncertainties, and are isolated binary evolution, triples in the field, binary-mediated interactions in GCs, and EKL in GN.[10] There is a high probability that the future observed NSBH merger population is a "blend" of two or more merger channels. We may be able to disentangle the contributions from different channels by looking at merger distributions in eccentricity, mass, spin, etc., as different merger channels produce different characteristic distributions in the merger parameter space (e.g., Rodriguez et al. 2018a; Takátsy et al. 2019; Arca Sedda 2020; Rastello et al. 2020). However, different channels do sometimes overlap in merger parameter space, so it may be very difficult to fully quantify the contribution of each merger channel to the observed distributions. We may also be able to classify individual GW sources (although this is probably not be possible for a majority of GW mergers). This can be accomplished with the detection of electromagnetic counterparts (e.g., Lee et al. 2010; Tsang 2013), or through the detection of imprints on the GW waveform present with some merger channels. For instance, for some EKL-assisted mergers in GN, the gravitational pull of the SMBH on the merging binary can be detected in both LIGO and LISA due to induced GW phase shifts (Inayoshi et al. 2017; Meiron et al. 2017), and eccentricity variations (Hoang et al. 2019; Randall & Xianyu 2019; Deme et al. 2020; Emami & Loeb 2020; Gupta et al. 2020).

We thank Bence Kocsis for helpful discussions. B.M.H. and S.N. acknowledge the partial support of NASA grant No. 80NSSC19K0321 and No. 80NSSC20K0505. S.N. also thanks Howard and Astrid Preston for their generous support. K.K. is supported by an NSF Astronomy and Astrophysics Postdoctoral Fellowship under award AST-2001751.

ORCID iDs

Bao-Minh Hoang https://orcid.org/0000-0003-0992-0033
Smadar Naoz https://orcid.org/0000-0002-9802-9279
Kyle Kremer https://orcid.org/0000-0002-4086-3180

References

Abbott, B. P., Abbott, R., Abbott, T. D., et al. 2016a, PhRvL, 116, 061102
Abbott, B. P., Abbott, R., Abbott, T. D., et al. 2016b, PhRvL, 116, 241103
Abbott, B. P., Abbott, R., Abbott, T. D., et al. 2017a, PhRvL, 119, 161101
Abbott, B. P., Abbott, R., Abbott, T. D., et al. 2017b, PhRvL, 118, 221101
Abbott, B. P., Abbott, R., Abbott, T. D., et al. 2017c, ApJL, 851, L35
Abbott, B. P., Abbott, R., Abbott, T. D., et al. 2017d, PhRvL, 119, 141101
Abbott, B. P., Abbott, R., Abbott, T. D., et al. 2019a, ApJL, 882, L24
Abbott, B. P., Abbott, R., Abbott, T. D., et al. 2019b, PhRvX, 9, 031040
Aharon, D., & Perets, H. B. 2016, ApJL, 830, L1
Alexander, T., & Hopman, C. 2009, ApJ, 697, 1861

[9] Rodriguez et al. (2018a) distinguish between bin–sin mergers that take place *after* one or more bin–sin encounters, and mergers that take place *during* a bin–sin encounter due to significant GW emission at close passage. They have termed the latter "GW capture" mergers. These mergers make up virtually all of their mergers with $e \gtrsim 0.05$ in the LIGO band. While the physical mechanism underlying the GW emission in these "GW capture" mergers is the same physical mechanism underlying GW emission in sin–sin GW captures, and despite of the similar name, we stress that they are a completely distinct merger channel. For the purposes of this work, we group them with the other bin–sin mergers in GCs. For more information about these mergers, see Samsing (2018) and Rodriguez et al. (2018a, 2018b).

[10] Note that the degree of uncertainty in the different channels varies considerably.

Aller, M. C., & Richstone, D. 2002, AJ, 124, 3035
Antonini, F., Murray, N., & Mikkola, S. 2014, ApJ, 781, 45
Antonini, F., & Perets, H. B. 2012, ApJ, 757, 27
Antonini, F., Toonen, S., & Hamers, A. S. 2017, ApJ, 841, 77
Arca Sedda, M. 2020, CmPhy, 3, 43
Arca Sedda, M., Askar, A., & Giersz, M. 2018, MNRAS, 479, 4652
Bahcall, J. N., & Wolf, R. A. 1977, ApJ, 216, 883
Banerjee, S. 2017, MNRAS, 467, 524
Banerjee, S. 2018, MNRAS, 473, 909
Banerjee, S., Baumgardt, H., & Kroupa, P. 2010, MNRAS, 402, 371
Bartos, I., Kocsis, B., Haiman, Z., & Márka, S. 2017, ApJ, 835, 165
Belczynski, K., Bulik, T., & Bailyn, C. 2011, ApJL, 742, L2
Belczynski, K., Dominik, M., Bulik, T., et al. 2010, ApJL, 715, L138
Belczynski, K., Holz, D. E., Bulik, T., & O'Shaughnessy, R. 2016, Natur, 534, 512
Belczynski, K., Taam, R. E., Kalogera, V., Rasio, F. A., & Bulik, T. 2007, ApJ, 662, 504
Beniamini, P., & Piran, T. 2016, MNRAS, 456, 4089
Bird, S., Cholis, I., Muñoz, J. B., et al. 2016, PhRvL, 116, 201301
Breen, P. G., & Heggie, D. C. 2013, MNRAS, 432, 2779
Carpenter, J. M. 2000, AJ, 120, 3139
Chirenti, C., Gold, R., & Miller, M. C. 2017, ApJ, 837, 67
Cholis, I., Kovetz, E. D., Ali-Haïmoud, Y., et al. 2016, PhRvD, 94, 084013
Clark, G. W. 1975, ApJL, 199, L143
Clausen, D., Sigurdsson, S., & Chernoff, D. F. 2013, MNRAS, 428, 3618
Clesse, S., & García-Bellido, J. 2017, PDU, 15, 142
Conselice, C. J., Blackburne, J. A., & Papovich, C. 2005, ApJ, 620, 564
Cordes, J. M., & Chernoff, D. F. 1998, ApJ, 505, 315
de Mink, S. E., & Mandel, I. 2016, MNRAS, 460, 3545
Deme, B., Hoang, B.-M., Naoz, S., & Kocsis, B. 2020, ApJ, 901, 125
Di Carlo, U. N., Giacobbo, N., Mapelli, M., et al. 2019, MNRAS, 487, 2947
Dominik, M., Berti, E., O'Shaughnessy, R., et al. 2015, ApJ, 806, 263
Dunstall, P. R., Dufton, P. L., Sana, H., et al. 2015, A&A, 580, A93
Dvorkin, I., Vangioni, E., Silk, J., Uzan, J.-P., & Olive, K. A. 2016, MNRAS, 461, 3877
Emami, R., & Loeb, A. 2020, MNRAS, 495, 536
Fernández, J. J., & Kobayashi, S. 2019, MNRAS, 487, 1200
Finn, L. S. 1987, MNRAS, 227, 265
Fragione, G., & Banerjee, S. 2020, ApJL, 901, L16
Fragione, G., & Bromberg, O. 2019, MNRAS, 488, 4370
Fragione, G., Grishin, E., Leigh, N. W. C., Perets, H. B., & Perna, R. 2019a, MNRAS, 488, 47
Fragione, G., & Kocsis, B. 2019, MNRAS, 486, 4781
Fragione, G., Leigh, N. W. C., & Perna, R. 2019b, MNRAS, 488, 2825
Fragione, G., & Loeb, A. 2019a, MNRAS, 486, 4443
Fragione, G., & Loeb, A. 2019b, MNRAS, 490, 4991
Freitag, M., Amaro-Seoane, P., & Kalogera, V. 2006, ApJ, 649, 91
Fryer, C. L., Woosley, S. E., & Hartmann, D. H. 1999, ApJ, 526, 152
Fujii, M. S., Tanikawa, A., & Makino, J. 2017, PASJ, 69, 94
Giesers, B., Kamann, S., Dreizler, S., et al. 2019, A&A, 632, A3
Gold, R., Bernuzzi, S., Thierfelder, M., Brügmann, B., & Pretorius, F. 2012, PhRvD, 86, 121501
Gondán, L., & Kocsis, B. 2019, ApJ, 871, 178
Gondán, L., Kocsis, B., Raffai, P., & Frei, Z. 2018a, ApJ, 855, 34
Gondán, L., Kocsis, B., Raffai, P., & Frei, Z. 2018b, ApJ, 860, 5
Goswami, S., Kiel, P., & Rasio, F. A. 2014, ApJ, 781, 81
Grindlay, J., Portegies Zwart, S., & McMillan, S. 2006, NatPh, 2, 116
Gupta, P., Suzuki, H., Okawa, H., & Maeda, K.-i. 2020, PhRvD, 101, 104053
Hansen, B. M. S., & Phinney, E. S. 1997, MNRAS, 291, 569
Hartwig, T., Volonteri, M., Bromm, V., et al. 2016, MNRAS, 460, L74
Heinke, C. O., Grindlay, J. E., Edmonds, P. D., et al. 2005, ApJ, 625, 796
Hoang, B.-M., Naoz, S., Kocsis, B., Farr, W. M., & McIver, J. 2019, ApJL, 875, L31
Hoang, B.-M., Naoz, S., Kocsis, B., Rasio, F. A., & Dosopoulou, F. 2018, ApJ, 856, 140
Hobbs, G., Lorimer, D. R., Lyne, A. G., & Kramer, M. 2005, MNRAS, 360, 974
Hobbs, G., Lyne, A. G., Kramer, M., Martin, C. E., & Jordan, C. 2004, MNRAS, 353, 1311
Hopkins, A. M., & Beacom, J. F. 2006, ApJ, 651, 142
Hopman, C., & Alexander, T. 2006, ApJL, 645, L133
Inayoshi, K., Kashiyama, K., Visbal, E., & Haiman, Z. 2016, MNRAS, 461, 2722
Inayoshi, K., Tamanini, N., Caprini, C., & Haiman, Z. 2017, PhRvD, 96, 063014
Jiménez-Esteban, F. M., Solano, E., & Rodrigo, C. 2019, AJ, 157, 78
Keshet, U., Hopman, C., & Alexander, T. 2009, ApJL, 698, L64
Kinugawa, T., Inayoshi, K., Hotokezaka, K., Nakauchi, D., & Nakamura, T. 2014, MNRAS, 442, 2963
Kinugawa, T., Miyamoto, A., Kanda, N., & Nakamura, T. 2016, MNRAS, 456, 1093
Kocsis, B., & Levin, J. 2012, PhRvD, 85, 123005
Kokkotas, K. D., & Schafer, G. 1995, MNRAS, 275, 301
Kouwenhoven, M. B. N., Goodwin, S. P., Parker, R. J., et al. 2010, MNRAS, 404, 1835
Kozai, Y. 1962, AJ, 67, 591
Kremer, K., Chatterjee, S., Ye, C. S., Rodriguez, C. L., & Rasio, F. A. 2019, ApJ, 871, 38
Kremer, K., Ye, C. S., Chatterjee, S., Rodriguez, C. L., & Rasio, F. A. 2020a, in IAU Symp. 351, Star Clusters: From the Milky Way to the Early Universe, ed. A. Bragaglia et al. (Cambridge: Cambridge Univ. Press), 357
Kremer, K., Ye, C. S., Rui, N. Z., et al. 2020b, ApJS, 247, 48
Kruckow, M. U., Tauris, T. M., Langer, N., Kramer, M., & Izzard, R. G. 2018, MNRAS, 481, 1908
Kumamoto, J., Fujii, M. S., & Tanikawa, A. 2019, MNRAS, 486, 3942
Lada, C. J., & Lada, E. A. 2003, ARA&A, 41, 57
Lee, M. H. 1993, ApJ, 418, 147
Lee, W. H., Ramirez-Ruiz, E., & van de Ven, G. 2010, ApJ, 720, 953
Lidov, M. L. 1962, P&SS, 9, 719
Liu, B., & Lai, D. 2019, MNRAS, 483, 4060
Lorimer, D. R., Bailes, M., & Harrison, P. A. 1997, MNRAS, 289, 592
Lower, M. E., Thrane, E., Lasky, P. D., & Smith, R. 2018, PhRvD, 98, 083028
Lu, C. X., & Naoz, S. 2019, MNRAS, 484, 1506
Lyne, A. G., Brinklow, A., Middleditch, J., Kulkarni, S. R., & Backer, D. C. 1987, Natur, 328, 399
Mackey, A. D., Wilkinson, M. I., Davies, M. B., & Gilmore, G. F. 2008, MNRAS, 386, 65
Mandel, I., & de Mink, S. E. 2016, MNRAS, 458, 2634
Mapelli, M. 2016, MNRAS, 459, 3432
Marchant, P., Langer, N., Podsiadlowski, P., Tauris, T. M., & Moriya, T. J. 2016, A&A, 588, A50
McKernan, B., Ford, K. E. S., Lyra, W., & Perets, H. B. 2012, MNRAS, 425, 460
McKernan, B., Ford, K. E. S., & O'Shaughnessy, R. 2020, MNRAS, 498, 4088
Meiron, Y., Kocsis, B., & Loeb, A. 2017, ApJ, 834, 200
Merritt, D., Piatek, S., Portegies Zwart, S., & Hemsendorf, M. 2004, ApJL, 608, L25
Morscher, M., Pattabiraman, B., Rodriguez, C., Rasio, F. A., & Umbreit, S. 2015, ApJ, 800, 9
Naoz, S. 2016, ARA&A, 54, 441
O'Leary, R. M., Kocsis, B., & Loeb, A. 2009, MNRAS, 395, 2127
O'Leary, R. M., Meiron, Y., & Kocsis, B. 2016, ApJL, 824, L12
O'Leary, R. M., Rasio, F. A., Fregeau, J. M., Ivanova, N., & O'Shaughnessy, R. 2006, ApJ, 637, 937
O'Shaughnessy, R., Kalogera, V., & Belczynski, K. 2010, ApJ, 716, 615
Peters, P. C., & Mathews, J. 1963, PhRv, 131, 435
Peuten, M., Zocchi, A., Gieles, M., Gualandris, A., & Hénault-Brunet, V. 2016, MNRAS, 462, 2333
Pfahl, E., Podsiadlowski, P., & Rappaport, S. 2005, ApJ, 628, 343
Phinney, E. S. 1991, ApJL, 380, L17
Porras, A., Christopher, M., Allen, L., et al. 2003, AJ, 126, 1916
Portegies Zwart, S. F., & McMillan, S. L. W. 2000, ApJL, 528, L17
Portegies Zwart, S. F., & McMillan, S. L. W. 2002, ApJ, 576, 899
Portegies Zwart, S. F., McMillan, S. L. W., & Gieles, M. 2010, ARA&A, 48, 431
Press, W. H., & Teukolsky, S. A. 1977, ApJ, 213, 183
Quinlan, G. D., & Shapiro, S. L. 1987, ApJ, 321, 199
Raghavan, D., McAlister, H. A., Henry, T. J., et al. 2010, ApJS, 190, 1
Ramirez-Ruiz, E., Trenti, M., MacLeod, M., et al. 2015, ApJL, 802, L22
Randall, L., & Xianyu, Z.-Z. 2018, ApJ, 864, 134
Randall, L., & Xianyu, Z.-Z. 2019, arXiv:1902.08604
Ransom, S. M. 2008, in IAU Symp. 246, Dynamical Evolution of Dense Stellar Systems, ed. E. Vesperini, M. Giersz, & A. Sills (Cambridge: Cambridge Univ. Press), 291
Rastello, S., Amaro-Seoane, P., Arca-Sedda, M., et al. 2019, MNRAS, 483, 1233
Rastello, S., Mapelli, M., Di Carlo, U. N., et al. 2020, MNRAS, 497, 1563
Rodriguez, C. L., Amaro-Seoane, P., Chatterjee, S., et al. 2018a, PhRvD, 98, 123005
Rodriguez, C. L., Amaro-Seoane, P., Chatterjee, S., & Rasio, F. A. 2018b, PhRvL, 120, 151101

Rodriguez, C. L., Chatterjee, S., & Rasio, F. A. 2016, PhRvD, 93, 084029
Sadowski, A., Belczynski, K., Bulik, T., et al. 2008, ApJ, 676, 1162
Samsing, J. 2018, PhRvD, 97, 103014
Samsing, J., D'Orazio, D. J., Kremer, K., Rodriguez, C. L., & Askar, A. 2020, PhRvD, 101, 123010
Sana, H., de Koter, A., de Mink, S. E., et al. 2013, A&A, 550, A107
Sasaki, M., Suyama, T., Tanaka, T., & Yokoyama, S. 2016, PhRvL, 117, 061101
Secunda, A., Bellovary, J., Mac Low, M.-M., et al. 2019, ApJ, 878, 85
Silsbee, K., & Tremaine, S. 2017, ApJ, 836, 39
Sipior, M. S., & Sigurdsson, S. 2002, ApJ, 572, 962
Stephan, A. P., Naoz, S., Ghez, A. M., et al. 2016, MNRAS, 460, 3494
Stephan, A. P., Naoz, S., Ghez, A. M., et al. 2019, ApJ, 878, 58
Stone, N. C., Metzger, B. D., & Haiman, Z. 2017, MNRAS, 464, 946
Strader, J., Chomiuk, L., Maccarone, T. J., Miller-Jones, J. C. A., & Seth, A. C. 2012, Natur, 490, 71
Takátsy, J., Bécsy, B., & Raffai, P. 2019, MNRAS, 486, 570
The LIGO Scientific collaboration 2020, Gravitational-Wave Candidate Event Database, https://gracedb.ligo.org/
Tsang, D. 2013, ApJ, 777, 103
Turner, M. 1977, ApJ, 216, 610
Wang, L., Spurzem, R., Aarseth, S., et al. 2016, MNRAS, 458, 1450
Wen, L. 2003, ApJ, 598, 419
Ye, C. S., Fong, W.-f., Kremer, K., et al. 2020, ApJL, 888, L10
Zevin, M., Samsing, J., Rodriguez, C., Haster, C.-J., & Ramirez-Ruiz, E. 2019, ApJ, 871, 91
Ziosi, B. M., Mapelli, M., Branchesi, M., & Tormen, G. 2014, MNRAS, 441, 3703

CHAPTER 5

Conclusion

Understanding the evolution of binaries is crucial to understanding the overall dynamic and evolution of nuclear star clusters. In this dissertation I have used binary and triple dynamics to better understand the life and death of binaries in galactic nuclei. I have shown how interactions with other objects in galactic nuclei, most importantly with the SMBH itself, affect the observable modes and signatures of stellar and CO binaries. These signatures can be found in both the electromagnetic and gravitational wave spectra, and observable with a wide variety of present and future instruments.

A majority of massive stars in galactic nuclei are expected to be in binaries, similarly to their galactic field counterparts (Raghavan et al., 2010; Moe & Di Stefano, 2017). Furthermore, massive stars end their lives in violent supernovae, receiving large natal velocity kicks that can significantly affect internal binary dynamics. In the inner region of galactic nuclei, where binaries orbit the SMBH with speeds ranging from hundreds to thousands of kilometers per second, these natal kicks have the potential to trigger a wide variety of astrophysical phenomena. In Hoang et al. (2022) from Chapter 2, we model how massive stellar binaries in the Galactic Center evolve when they undergo natal kicks. We show that these natal kicks trigger the creation of both electromagnetic observables (X-ray binaries, hypervelocity stars & binaries, and tidal disruption events), and gravitational wave events (EMRIs, direct plunges, and binary CO mergers). The findings regarding X-ray binaries are particularly exciting. We have shown that the population of X-ray binaries in the Galactic Center can be used as a diagnostic for the magnitude of BH natal kicks, which remain debated. Furthermore, natal kicks in binaries orbiting an SMBH can create hypervelocity X-ray binaries. In addition, most objects are retained in the nuclear cluster post-kicks, building up population of single and binary COs in the Galactic Center. This CO population can result in gravitational wave mergers, which is addressed in Chapters 3 and 4.

The recent discoveries of LIGO/Virgo, and the promise of future GW observatories like LISA, has made it possible to observe and study the hitherto invisible CO binaries, with important implications for the CO population in galactic nuclei. CO binaries in galactic nuclei reside in a dynamically unique environment, undergoing interactions with both the SMBH and the other members of the dense nuclear cluster, resulting in distinct observational signatures. The publications presented in Chapter 3 model how the SMBH can induce GW mergers of CO binaries via the EKL mechanism, and how mergers from this channel can be distinguished by the future LISA mission. In Hoang et al. (2018), we calculate the rate of mergers of BH binaries in galactic nuclei and found a strong direct dependence on the number of binaries per galactic nuclei. Thus, if can we get an estimate of the rate of GW mergers from this mechanism, we can get a number estimate of the CO population per galactic nuclei. In order to have a good estimate of the observed rate of CO mergers in galactic nuclei, we need a way to distinguish this type of merger from mergers coming from other channels. We show in Hoang et al. (2019) a method to detect SMBH-induced eccentricity oscillations in binary black holes with the future GW observatory LISA. LISA can detect stellar-mass CO binaries for a large fraction of their lifetime, long before they merge in the LIGO frequency band. We show that LISA can detect changes in binary eccentricity due to gravitational perturbations from the SMBH, for sources up to a few Mpc away. In addition to BH binaries, we can apply this formalism to a variety of CO binaries. In Deme et al. (2020) we apply this technique to binaries consisting of an IMBH and a stellar-mass CO in galactic nuclei. We show that similarly to the case in Hoang et al. (2019), LISA will be able to detect EKL-induced eccentricity oscillations in these binaries, out to a few Mpcs. In general, the identification of formation channel for observed GW events pose a challenge, due to the multitude of possible mechanisms, and their observational degeneracies. The studies presented here show that it is possible, with LISA, to detect the unique GW signatures of binaries undergoing EKL-driven merger in galactic nuclei.

Single COs in dense clusters, although not emitting GWs by themselves, undergo frequent close encounters that may lead to GW events detectable by LIGO. In Hoang et al. (2020) from Chapter 4, we model single-single captures of NSs and BHs in clusters (nuclear, globular, and young stellar clusters), which form highly eccentric NSBH binaries that merge in the LIGO frequency range. We also compile and compare the rate of NSBH mergers from this channel to other channels proposed in the literature. Our investigation shows that GW captures in clusters is not likely the main contributor to the overall NSBH merger rate. However, of the three types of clusters investigated, NSBH captures in galactic nuclei resulted in the highest merger rate, and this result can help us learn more about the population of COs in galactic nuclei. This is because our result depends on several assumptions about the population of COs in galactic nuclei, chiefly among which is the assumption on the density of compact objects. We have used theoretical models for the density of COs in the types of clusters we studied. Assuming we have templates for eccentric GW mergers in the future, we can very easily distinguish mergers resulting from captures because they remain eccentric in the LIGO band. Thus, once we have a statistical population of observed NSBH mergers in the future, we will be able to use these observations to inform our understanding of CO densities in clusters.

In conclusion, the evolution of binaries in galactic nuclei is coupled to the SMBH, and we have used gravitational dynamics to explore the effect this relationship has on the observational signatures of binaries. We have shown that during the process of becoming COs, the dynamical evolution of stellar binaries can result in a variety of electromagnetic observables such as X-ray binaries, and hypervelocity stars & binaries, and also gravitational wave events like EMRIs. The single and binary COs remaining comprise an exciting opportunity to study galactic nuclei in a brand new way. The GW signals of CO binaries in galactic nuclei contain the unique fingerprint of the SMBH's gravitational influence, which can be detected with LISA. Moreover, future LIGO observations of NSBH mergers can shed light on the properties of the population of dark remnants in nuclear clusters. I have demonstrated in this dissertation the different ways in which population of stellar binaries in galactic nuclei can be observed and identified during the process of, and after becoming COs. This work provides a roadmap of how we can use future electromagnetic and gravitational wave observations to better understand the underlying binary population; and thus better understand the star formation and overall history of galactic nuclei.

Bibliography

Abbott, R., Abbott, T. D., Abraham, S., et al. 2021a, ApJL, 915, L5

Abbott, R., Abbott, T. D., Abraham, S., et al. 2021b, ApJL, 913, L7

Antonini, F. & Perets, H. B. 2012, ApJ, 757, 27

Bahcall, J. N. & Wolf, R. A. 1976, ApJ, 209, 214

Bahcall, J. N. & Wolf, R. A. 1977, ApJ, 216, 883

Bartko, H., Martins, F., Fritz, T. K., et al. 2009, ApJ, 697, 1741

Bartos, I., Kocsis, B., Haiman, Z., & Márka, S. 2017, ApJ, 835, 165

Belczynski, K., Holz, D. E., Bulik, T., & O'Shaughnessy, R. 2016, Nature, 534, 512

Bethe, H. A. & Brown, G. E. 1998, ApJ, 506, 780

Bortolas, E. & Mapelli, M. 2019, MNRAS, 485, 2125

Bortolas, E., Mapelli, M., & Spera, M. 2017, MNRAS, 469, 1510

Breivik, K., Rodriguez, C. L., Larson, S. L., Kalogera, V., & Rasio, F. A. 2016, ApJL, 830, L18

Chen, X. & Amaro-Seoane, P. 2017, ApJL, 842, L2

Chu, D. S., Do, T., Hees, A., et al. 2018, ApJ, 854, 12

Cordes, J. M. & Chernoff, D. F. 1998, ApJ, 505, 315

de Mink, S. E. & Mandel, I. 2016, MNRAS, 460, 3545

Deme, B., Hoang, B.-M., Naoz, S., & Kocsis, B. 2020, ApJ, 901, 125

Dexter, J. & O'Leary, R. M. 2014, ApJL, 783, L7

Do, T., Lu, J. R., Ghez, A. M., et al. 2013a, ApJ, 764, 154

Do, T., Martinez, G. D., Yelda, S., et al. 2013b, ApJL, 779, L6

D'Orazio, D. J. & Samsing, J. 2018, MNRAS, 481, 4775

Fragos, T., Willems, B., Kalogera, V., et al. 2009, ApJ, 697, 1057

Fryer, C. L., Woosley, S. E., & Hartmann, D. H. 1999, ApJ, 526, 152

Gautam, A. K., Do, T., Ghez, A. M., et al. 2019, ApJ, 871, 103

Genzel, R., Schödel, R., Ott, T., et al. 2003, ApJ, 594, 812

Gondán, L. & Kocsis, B. 2019, ApJ, 871, 178

Gondán, L. & Kocsis, B. 2021, MNRAS, 506, 1665

Gondán, L., Kocsis, B., Raffai, P., & Frei, Z. 2018a, ApJ, 855, 34

Gondán, L., Kocsis, B., Raffai, P., & Frei, Z. 2018b, ApJ, 860, 5

Gualandris, A., Colpi, M., Portegies Zwart, S., & Possenti, A. 2005, ApJ, 618, 845

Hailey, C. J., Mori, K., Bauer, F. E., et al. 2018, Nature, 556, 70

Hansen, B. M. S. & Phinney, E. S. 1997, MNRAS, 291, 569

Hills, J. G. 1988, Nature, 331, 687

Hoang, B.-M., Naoz, S., Kocsis, B., Farr, W. M., & McIver, J. 2019, ApJL, 875, L31

Hoang, B.-M., Naoz, S., Kocsis, B., Rasio, F. A., & Dosopoulou, F. 2018, ApJ, 856, 140

Hoang, B.-M., Naoz, S., & Kremer, K. 2020, ApJ, 903, 8

Hoang, B.-M., Naoz, S., & Sloneker, M. 2022, arXiv e-prints, arXiv:2204.03661

Hobbs, G., Lyne, A. G., Kramer, M., Martin, C. E., & Jordan, C. 2004, MNRAS, 353, 1311

Kremer, K., Rodriguez, C. L., Amaro-Seoane, P., et al. 2019, PRD, 99, 063003

Lee, M. H. 1993, ApJ, 418, 147

Lorimer, D. R., Bailes, M., & Harrison, P. A. 1997, MNRAS, 289, 592

Lu, C. X. & Naoz, S. 2019, MNRAS, 484, 1506

Lu, J. R., Do, T., Ghez, A. M., et al. 2013, ApJ, 764, 155

Lu, J. R., Ghez, A. M., Hornstein, S. D., et al. 2009, ApJ, 690, 1463

Macquart, J. P., Kanekar, N., Frail, D. A., & Ransom, S. M. 2010, ApJ, 715, 939

Mandel, I. & de Mink, S. E. 2016, MNRAS, 458, 2634

Martins, F., Trippe, S., Paumard, T., et al. 2006, ApJL, 649, L103

Miller, M. C. & Hamilton, D. P. 2002, ApJ, 576, 894

Moe, M. & Di Stefano, R. 2017, ApJS, 230, 15

Muno, M. P., Lu, J. R., Baganoff, F. K., et al. 2005, ApJ, 633, 228

Naoz, S. 2016, ARA&A, 54, 441

Naoz, S., Ghez, A. M., Hees, A., et al. 2018, ApJL, 853, L24

Nishizawa, A., Berti, E., Klein, A., & Sesana, A. 2016, PRD, 94, 064020

Nishizawa, A., Sesana, A., Berti, E., & Klein, A. 2017, MNRAS, 465, 4375

O'Leary, R. M., Kocsis, B., & Loeb, A. 2009, MNRAS, 395, 2127

O'Leary, R. M., Rasio, F. A., Fregeau, J. M., Ivanova, N., & O'Shaughnessy, R. 2006, ApJ, 637, 937

Ott, T., Eckart, A., & Genzel, R. 1999, ApJ, 523, 248

Peters, P. C. & Mathews, J. 1963, Physical Review, 131, 435

Pfahl, E. & Loeb, A. 2004, ApJ, 615, 253

Pfuhl, O., Alexander, T., Gillessen, S., et al. 2014, ApJ, 782, 101

Phifer, K., Do, T., Meyer, L., et al. 2013, ApJL, 773, L13

Portegies Zwart, S. F. & McMillan, S. L. W. 2000, ApJL, 528, L17

Portegies Zwart, S. F. & Yungelson, L. R. 1998, A&A, 332, 173

Prodan, S., Antonini, F., & Perets, H. B. 2015, ApJ, 799, 118

Quinlan, G. D. & Shapiro, S. L. 1987, ApJ, 321, 199

Rafelski, M., Ghez, A. M., Hornstein, S. D., Lu, J. R., & Morris, M. 2007, ApJ, 659, 1241

Raghavan, D., McAlister, H. A., Henry, T. J., et al. 2010, ApJS, 190, 1

Randall, L. & Xianyu, Z.-Z. 2019, arXiv e-prints, arXiv:1902.08604 [astro-ph.HE]

Repetto, S., Davies, M. B., & Sigurdsson, S. 2012, MNRAS, 425, 2799

Rodriguez, C. L., Chatterjee, S., & Rasio, F. A. 2016, PRD, 93, 084029

Samsing, J. & D'Orazio, D. J. 2018, MNRAS, 481, 5445

Schödel, R., Genzel, R., Ott, T., & Eckart, A. 2003, Astronomische Nachrichten Supplement, 324, 535

Stephan, A. P., Naoz, S., Ghez, A. M., et al. 2016, MNRAS, 460, 3494

Stone, N. C., Metzger, B. D., & Haiman, Z. 2017, MNRAS, 464, 946

Takátsy, J., Bécsy, B., & Raffai, P. 2019, MNRAS, 486, 570

Tsang, D. 2013, ApJ, 777, 103

Turner, M. 1977, ApJ, 216, 610

Tutukov, A. V. & Yungelson, L. R. 1993, MNRAS, 260, 675

Wen, L. 2003, ApJ, 598, 419

Willems, B., Henninger, M., Levin, T., et al. 2005, ApJ, 625, 324

Witzel, G., Ghez, A. M., Morris, M. R., et al. 2014, ApJL, 796, L8

Witzel, G., Sitarski, B. N., Ghez, A. M., et al. 2017, ApJ, 847, 80

Yu, Q. & Tremaine, S. 2003, ApJ, 599, 1129

Zubovas, K., Wynn, G. A., & Gualandris, A. 2013, ApJ, 771, 118